UPC **CTTC**

Computational modeling of adsorption packed bed reactors and solar-driven adsorption cooling systems

Centre Tecnològic de Transferència de Calor
Departament de Màquines i Motors Tèrmics
Universitat Politècnica de Catalunya

Giorgos Papakokkinos

Doctoral Thesis

Computational modeling of adsorption packed bed reactors and solar-driven adsorption cooling systems

Giorgos Papakokkinos

TESI DOCTORAL

presentada al

Departament de Màquines i Motors Tèrmics
ESEIAAT
Universitat Politècnica de Catalunya

per a l'obtenció del grau de

Doctor per la UPC

Terrassa, Gener 2021

Computational modeling of adsorption packed bed reactors and solar-driven adsorption cooling systems

Giorgos Papakokkinos

Directors de la Tesi

Dr. Jesús Castro Gonzalez

Dr. Assensi Oliva Llena

Tribunal Qualificador

Dr. First Committee Member

University of Commitee Member

Dr. Second Committee Member

University of Commitee Member

Dr. Third Committee Member

University of Commitee Member

Στην μητέρα μου Ελισάβετ, στον πατέρα μου Μάριο

A mi madre Elisavet, a mi padre Mario

Acknowledgements

La culminación de esta tesis conlleva inevitablemente una retrospección de los últimos años. La idea de hacer un doctorado y de involucrarme con el lado sostenible de la energía se debe a mis Profesores en la Politécnica de Atenas – especialmente a los Profesores Zervos y Voutsinas. Quiero agradecerles porque tantos años después, sigue pareciendo una buena idea.

Había flirteado con la posibilidad de hacer un doctorado varias veces antes de mi encuentro con Profesor Carlos David Pérez Segarra, primero como docente en métodos numéricos y transferencia de calor, y posteriormente como director de mi tesis del máster. Dicho encuentro fue catalítico para mi decisión de realizar el doctorado en el CTTC. Quiero agradecerle por todo lo que me ha aportado y por apoyar mi candidatura como estudiante de doctorado en el CTTC.

Una vez dentro del laboratorio, el Profesor Assensi Oliva me acogió y me cuidó como a todos los compañeros y compañeras del CTTC, siempre transmitiendo entusiasmo y dando coraje. Estoy agradecido a Assensi por darme la oportunidad de realizar la tesis sobre un tema que considero interesante y significativo, y además, por la confianza y la libertad que me ha dado en crear las condiciones óptimas de trabajo.

La persona con la que más he interactuado en el contexto del doctorado ha sido el director de mi tesis, Profesor Jesús Castro. Estoy profundamente agradecido a Jesús por aconsejarme y guiarme durante el doctorado, estando siempre disponible a escuchar y a dialogar. Jesús es una persona muy generosa y me considero afortunado porque entre nosotros se desarrolló una honesta relación.

Desde los primeros días en el laboratorio, la interacción con los compañeros y las compañeras fue determinante en el desarrollo de la tesis y en mi progreso como investigador. Quiero agradecer: a Oriol L., por las ideas que me aportó en métodos numéricos y por su previo trabajo en el laboratorio – a Lluís J., por introducirme en el código de TermoFluids – a Joan L., por enseñarme las entrañas de NEST, la filosofía de la programación object-oriented y por insistir en utilizar vim y tmux – a Jordi C., por sacarme de incontables pozos de código y por enseñarme como conseguir salir solo – a Guillem por su valioso apoyo en LaTeX y por su inestimable ayuda en cualquier asunto compartía con él – a Eduard, por los estimulantes meses que pasamos desarrollando los solvers implícitos – a Roser por su colaboración en las simulaciones de edificios – a Octavi, por su inestimable ayuda en cuestiones informáticas – a Jordi M., Jordi V., Xavi T., Deniz, Arnau, Nacho y Joan C., por resolver mis dudas en

varias ocasiones. En el contexto de esta tesis se ha ideado la realización de un futuro experimento. En las tareas relevantes, agradezco la ayuda que tuve por parte de Jian y por parte de Manolo, el técnico del laboratorio, que nos dejó precipitadamente y le echamos de menos. Consciente que la tesis se benefició de la experiencia colectiva del laboratorio, quiero dar las gracias a cada persona que pasó por el CTTC.

Quiero agradecer a Dr. Füldner de Fraunhofer Institute, por el suministro de los datos experimentales que se utilizaron para la validación del modelo del sistema y por aclarar mis dudas en varias ocasiones. Agradezco la ayuda de mi amigo Anish M. que estuvo siempre disponible a dialogar, a leer mis textos y a darme sus consejos.

Fuera del laboratorio, mi implicación con dos microcosmos sirvió como válvula de escape y ayudó a mantener los equilibrios, sobre todo durante los primeros años del doctorado. Se trata de la Associació Discapacitat Visual de Catalunya y el mundillo de volley de Montgat Nord. Especialmente, quiero agradecer a Manel, presidente de la asociación, por los numerosos buenos momentos y las cosas que aprendí de él – y también mi compañera de volley, Pavlina, por la motivación y los ánimos.

El doctorado fue entrelazado con varias visitas a mi país. Querría expresar mis agradecimientos a mis amigos y familiares en Chipre por su cariño, por crear un ambiente acogedor cuando visitaba la isla y por reaccionar con el mismo entusiasmo cada vez que anunciaba que el doctorado estaba en la recta final. Quiero agradecer a mis amigos Alexandros y Maria por cuidarme tanto cada vez que pasaba por Atenas.

Dos personas me han acompañado de cerca en toda la trayectoria del doctorado; han vivido todas las peripecias de la tesis, celebrando conmigo las pequeñas victorias y arropándome en las pequeñas derrotas. Muchas gracias Spiros por todo – me atrevo a decir que a través de nuestra amistad, entiendo el mundo un poco mejor. Moltes gràcies Alba per estar al meu costat tots aquests anys, pel teu suport i amor, pels riures i pels dibuixets.

Quiero dar las gracias a mi hermana Eleni y a su pareja, Michalis, por su inestimable e incondicional apoyo en toda mi vida. Eleni, es un autentico regalo tenerte como hermana. Dedico esta tesis a mi madre, Elisavet, y a mi padre, Mario, por su insuperable amor y dedicación - y por su ejemplo de fuerza y coraje.

Contents

Abstract

Environmental concerns regarding climate change and ozone depletion urge for a paradigm shift in the cooling production. The cooling demand exhibits an alarmingly increasing trend, thus its satisfaction in a sustainable manner is imperative. Adsorption cooling systems (ACSs) are a potential candidate for a sustainable future of cooling production. ACSs do not contribute to the aforementioned environmental problems, since they can utilize solar energy or waste heat, as well as they can employ substances with zero ozone depletion potential and global warming potential. The objective of this doctoral thesis is to contribute to the investigation and improvement of ACSs. The contribution is attempted through the development of two computational models – which approach ACSs from different perspectives – and their respective utilization for the conduction of related numerical studies.

The first research direction focuses on the design of the adsorption reactor, the most vital component of ACSs. The geometrical configuration of the reactor is determinant for the system performance. The reactor design is a crucial task since it creates a dichotomy between the two important performance indicators – the Specific Cooling Power (SCP) and the Coefficient of Performance (COP). Individual optimizations based on the SCP and the COP would result in completely opposite geometrical configurations. A computational model for the simulation of adsorption packed bed reactors was developed. The model is capable of simulating any potential reactor geometry, as it is implemented using three-dimensional unstructured meshes. The packed bed domain and the solid heat exchanger domain are simulated in a conjugate manner. A multi-timestep approach is adopted, resulting in a drastic reduction of the computational cost of the simulations. Verification and validation assessments were performed in order to evaluate the reliability of the model. Two major studies were conducted within this research direction. The first aspires to provide a comparison between five different reactor geometries, motivated by the lack of comparability across different studies in the literature. Thirteen cases of each geometry are simulated, by varying the fin thickness, the fin length and the solid volume fraction. In this study, the SCP of the adsorption phase is quantified. The second study pertains to a thorough investigation of a geometry that remained underexplored hitherto – the hexagonal honeycomb adsorption reactor. Both the COP and the SCP are quantified. A parametric study is conducted with respect to the three dimensions that define the geometry, as well as for various operating conditions.

The second research direction is dedicated to the investigation of adsorption cooling

systems, and in particular, to their integration within a wider thermal system, a solar-cooled building. Such integration is not straight-forward due to thermal inertia effects and the inherent cyclic operation of ACSs, as well as due to the dependence on an intermittent source and an auxiliary unit, with a clear objective to prioritize solar energy. A numerical model was developed using one-dimensional models for the adsorption reactors and lumped-capacitance models for the evaporator and condenser. The model is validated against experimental results found in the literature. Furthermore, it is coupled to the generic optimization program GenOpt, thus allowing the conduction of optimization studies. The ACS model is then coupled to solar collectors and thermal storage models, as well as to a building model. The latter is simulated with NEST-buildings, a buildings simulation tool, previously developed in the CTTC laboratory. This coupling results in a comprehensive simulation tool for adsorption-based solar-cooled buildings. A case study regarding a solar-cooled office is considered, with the objective to investigate the potential of satisfying its cooling demand using solar energy, and thus, take advantage of the associated environmental benefits. A control strategy is proposed based on variable cycle duration, using optimized values for the instantaneous operating conditions. The variable cycle duration approach allows to satisfy the cooling demand using significantly less solar collectors or less auxiliary energy input. The potential CO_2 emissions avoidance is calculated between 28.1-90.7% with respect to four scenarios of electricity-driven systems of different performance and CO_2 emission intensity.

1

Introduction

1.1 Motivation

The motivation of this work has its roots in three aspects of the cooling production: (i) its significant contribution on the quality of human life, (ii) its highly increasing demand and (iii) the environmentally unsustainable current solution, along with the technological drawbacks entailed.

Cooling is the process of heat removal and the consequent temperature reduction and/or phase change. Cooling technologies have progressively become a fundamental contributor to the improvement of the quality of human life. In the forefront, the most recognizable applications of cold production are comfort cooling, food preservation, as well as the supply chain and conservation of vaccines and medicines. Consequently, cooling contributes to people well-being and health through thermal comfort, it shapes human nutritional habits, it plays a significant role in the eradication of diseases and it allows the distribution and conservation of medicines such as insulin and chemotherapy drugs. Apart from these basic applications, cooling forms part of several other processes, such as the fertilizer production for agriculture, medical engineering equipment, cryopreservation, industrial and metallurgical processes, and heat dissipation of electronics. The extension of the influence of cooling in human societies is multifaceted. A recent study identified links between cooling and all 17 Sustainable Development Goals set by the United Nations [1, 2].

With respect to comfort cooling, the worldwide demand has increased significantly in the past decades and it is expected to follow this trend in the future. According to the International Energy Agency [3], the worldwide cooling demand in the building sector overtripled from 1990 to 2016, from 608 TWh to 2021 TWh. Based on their baseline scenario, it is predicted that by 2050 it will overtriple again, reaching 6200 TWh. Cooling is identified as the most significant contributor to the anticipated growth of the electricity demand in buildings, being responsible for 40% of the total growth.

The increase of the global cooling demand may be attributed to various factors: (i) the socioeconomic development of previously underdeveloped regions [4], (ii) global

warming creates the necessity of cooling even in colder climates during summer [5], (iii) the heat island effect increases the cooling demand in cities [6], (iv) the urbanization of earth results in an even greater portion of the population being affected by the heat island effect [7], (v) the human population growth [3] and (vi) the contemporary lifestyle is associated with higher internal heat gains in buildings [3].

Currently, the cooling demand is mostly satisfied by electricity-driven cooling systems, utilizing electricity produced mainly by the combustion of fossil fuels, which entails greenhouse gases emissions. Moreover, although the ozone-depleting refrigerants are successfully being phased out according to the Montreal Protocol, their successors – the current refrigerant generation – have significantly high global warming potential and they must be phased down according to the Kigali Amendment [8]. Furthermore, the economic cost for operating these systems is subjected to the market instabilities caused by the fossil fuel depletion. Apart from the environmental and economical issues, the current solution entails some technological drawbacks. Electricity-driven cooling systems create disproportionally significant peaks on the electrical load of national grids during warm months, as a result of high temperatures, and in some cases, considerable tourist fluxes. Consequently, stability problems are provoked in the national electrical grids, as well as the necessity to overdimension them in order to be able to satisfy these demand peaks. Furthermore, the cooling demand is mostly consumed in cities, away from the power plants, and thus, it is associated to transmission losses.

In view of the aforementioned increase of the cooling demand and the problematic current situation, it becomes evident that the cooling technologies must move towards more sustainable solutions. Thermally-driven cooling technologies could form part of this sustainable solution, since they can be driven by solar energy or waste heat, as well as they can employ refrigerants that do not deplete the ozone layer and they do not contribute to global warming. Furthermore, they allow to satisfy the cooling demand in a decentralized and local manner, and consequently, alleviate national electrical grids from the disproportionally high peaks and avoid transmission losses.

Among the thermally-driven cooling technologies, the most mature is absorption cooling. Although the performance of adsorption cooling is lower, it exhibits certain advantages and attracts research interest. In comparison to absorption cooling, adsorption cooling (i) does not have crystallization and corrosion problems [9], (ii) has lower auxiliary electricity consumption since there is no solution pump [10], (iii) may be driven by lower operating temperatures [11], and in general, the wide range of

adsorption pairs allow the operation in a wider range of driving and evaporation temperatures, (iv) has fewer moving parts, and thus, less maintenance requirements [12], and (v) has lower vibration and noise levels [13].

The investigation of the physical phenomena involved – as well as the environmental importance of these technologies – are well aligned with the idiosyncrasy of the CTTC laboratory. In fact, absorption cooling pertains to the research interests of the laboratory for over two decades. Hitherto, three doctoral theses have been conducted and one more is under development, within the frame of absorption cooling in CTTC. This doctoral thesis is the first venture of the laboratory in the field of adsorption cooling.

1.2 Adsorption cooling technology

This section aims to present the adsorption cooling technology. Section 1.2.1 is concerned with the explanation of the basic physical phenomena involved in adsorption cooling, namely, adsorption and cooling production. Subsequently, Section 1.2.2 proceeds to describe the synthesis of the two phenomena into the adsorption cooling concept and thermodynamic cycle. Finally, the section closes with the presentation of the major challenges in the design and operation of this technology.

1.2.1 Introductory concepts

1.2.1.1 Adsorption phenomenon

Adsorption is a surface phenomenon which describes the adhesion of a certain component – atoms, molecules, ions – of a liquid or gas onto the common interface with a solid or liquid phase.

Adsorption is further classified into physisorption and chemisorption, based on the nature of the particle adhesion. In physisorption, the adhesion of the components is a result of weak van der Waals forces [1], whereas in chemisorption a chemical bond is formed at the interface [15].

[1] According to IUPAC the term van der Waals forces is used for all nonspecific attractive or repulsive intermolecular forces [14]

The manifestation of the adsorption phenomenon which is relevant in the context of adsorption cooling is physisorption of gas molecules onto solid surfaces (Figure 1.1a). In this context, adsorbent is the solid onto which adsorption occurs, adsorbate is the adsorbed state, while the gas state is referred to as adsorptive [15] (although the term adsorbate is often used for the substance in general, either in adsorbed or gaseous state).

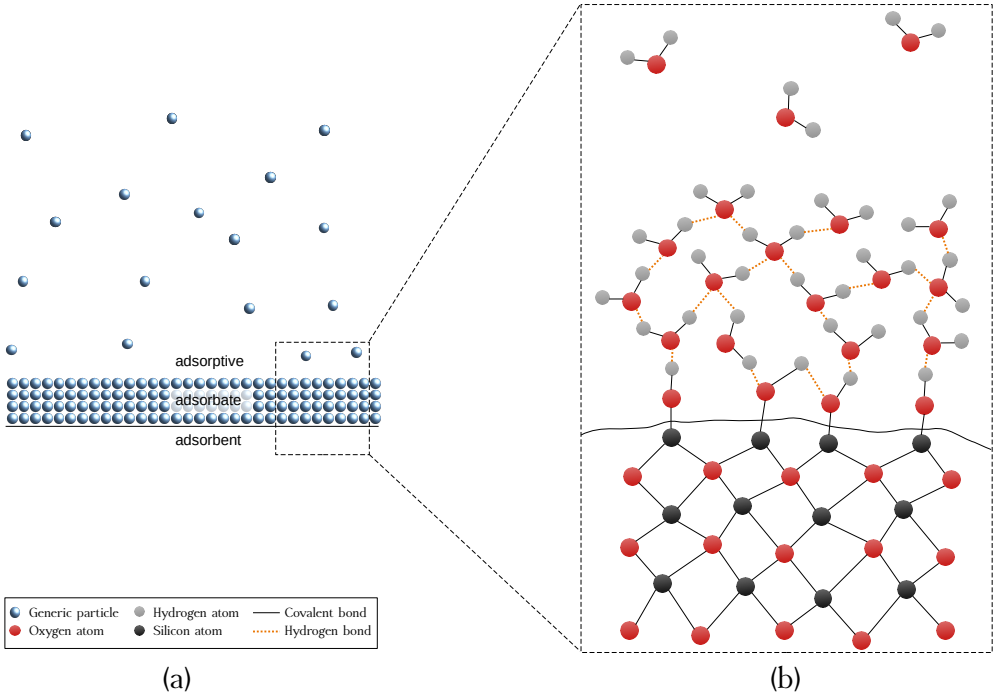

Figure 1.1: Conceptual illustration of (a) Generic physisorption and (b) Adsorption of water on silica gel

The adsorption of a gas molecule – its attachment onto the solid surface – is an exothermic process. The inverse process – the detachment of an adsorbed molecule and its return to the gas state – is called desorption and it is an endothermic process. The adsorption equilibrium capacity is determined by the temperature and the pressure. The mathematical relation employed for the calculation of the adsorption equilibrium capacity is called adsorption isotherm [15]. When an adsorbent is exposed to a gas and the adsorbed mass is less than its equilibrium capacity, the gas is adsorbed spon-

taneously and the adsorption enthalpy is released. Inversely, if the adsorbed mass is higher than the equilibrium capacity, adsorbate will spontaneously desorb and the adsorption enthalpy will be consumed.

The adsorption pair that is considered at the most part of this thesis is silica gel and water. Silica gel is an amorphous silicon dioxide (SiO_2), with silanol groups on its surface (Si-O-H). The presence of silanols increases the polarity and the hydrophilicity of the surface [16, 17]. The silanol groups on the surface of silica gel form hydrogen bonds with the gaseous water molecules [18]. As illustrated in Figure 1.1b, the first layer of the adsorbed water molecules forms further hydrogen bonds with other gaseous water molecules, resulting in the formation of multiple layers.

1.2.1.2 Cooling production

The principle of cooling production is based on the endothermic nature of the liquid-gas phase transition. The transition of liquid to gas involves an energy input, the latent heat of vaporization. The latter is the energy required in order to overcome the intermolecular attraction forces between the liquid molecules. The most familiar manifestation of vaporization is by providing the required energy to the medium, namely, by heating it. However, vaporization occurs as well through a pressure reduction, without providing the latent heat to the medium. Figure 1.2 illustrates the two processes of liquid-gas phase change on the phase diagram of water. When vaporization occurs through a pressure reduction, the latent heat is absorbed from the surrounding medium and thus, its temperature decreases.

Consider an adiabatic closed vessel containing a single substance, water, in liquid and gas state. Although macroscopically the two phases are separated, at the interface between gas and liquid there is a constant migration of water molecules, from one phase to the other. At dynamic equilibrium, the evaporation rate and the condensation rate are equal, hence, the mass of each phase remains constant. The gas pressure at dynamic equilibrium is known as the equilibrium vapor pressure, which is a function of the temperature. As the temperature increases, the equilibrium vapor pressure increases as well.

While in equilibrium, consider that the gas pressure becomes lower than the equilibrium vapor pressure, by removing a certain amount of gas molecules. Suddenly, the equilibrium is disrupted. The liquid molecules passing to the gas phase will be

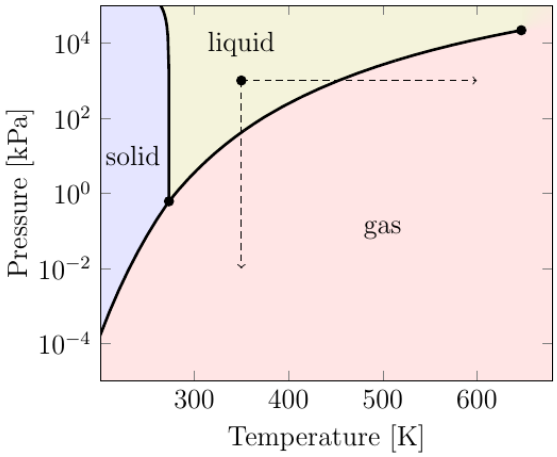

Figure 1.2: Pressure-Temperature phase diagram of water

more than the gas molecules passing to the liquid phase. Therefore, a net positive evaporation rate is established. This will continue until equilibrium is achieved anew; namely, until the gas pressure reaches again the equilibrium vapor pressure. Note that in this case, no heat input was provided to the system. Thus, the latent heat of vaporization associated to the evaporation that took place was absorbed from the medium itself, and consequently, its temperature decreases.

Building on the simplified example above, a continuous cooling production can be achieved if a gas outflow is established in the vessel, as well as an equal liquid mass inflow. In order to take advantage of the cooling produced – and avoid freezing – a secondary system should circulate a heat transfer fluid (HTF) through the vessel. The HTF enters at a temperature higher than the vessel temperature, exchanges heat and its temperature decreases.

1.2.2 Adsorption cooling

1.2.2.1 Basic concept

As it arises, a synergy can be implemented between an evaporator and an adsorbent, in order to achieve cooling production. Conceptually, this synergy is based on using

a not saturated adsorbent in order to suction out the vapor from the evaporator, and consequently, provoke evaporation and the desired cooling production. An intrinsic characteristic of this concept is that once the adsorbent is saturated, the adsorbate must be removed in order to restore anew its capacity to adsorb. Thus, a desorption – or regeneration – process is performed, during which, no cooling production takes place.

1.2.2.2 Adsorption cooling thermodynamic cycle

Having introduced the fundamental physical phenomena involved and the basic concept, this section proceeds with the presentation of the adsorption cooling thermodynamic cycle.

An adsorption cooling system (ACS) is composed by three basic components: the adsorption reactor, the evaporator and the condenser. The adsorption cooling thermodynamic cycle is divided into four phases: (a) pre-cooling, (b) adsorption, (c) pre-heating and (d) desorption. The desired cooling effect is produced only in the adsorption phase. During the rest phases there is no cooling production. Thus, in order to avoid intermittent cooling production, it is a common strategy to employ two reactors that operate alternately. Namely, while one reactor undergoes the phases in the order a-b-c-d, the other undergoes the phases in the order c-d-a-b.

The thermodynamic cycle is defined by the temperature of three secondary circuits T_{high}, T_{med} and T_{low}, which deliver heat transfer fluid to the components in order to regulate their temperatures. When the reactor operates as a desorber, its HTF has temperature T_{high}, whereas at its adsorber operation the HTF has temperature T_{med}. The latter is also considered as the HTF temperature of the condenser, and hence, the saturation pressure of the refrigerant at T_{med} defines the condenser pressure P_{con}. Similarly, T_{low} corresponds to the HTF temperature of the evaporator, thus the saturation pressure of the refrigerant at T_{low} defines the evaporator pressure P_{eva}. Within these operating conditions, the adsorbed mass in each reactor is cycling between the minimum adsorption capacity w_{low} and the maximum adsorption capacity w_{high}, which correspond to the adsorption equilibrium capacity at (P_{con}, T_{high}) and (P_{eva}, T_{med}), respectively.

Figure 1.3 illustrates the ACS operation during the four phases (valve openings, flow direction, reactor operation mode), alongside with the Clapeyron diagram of the ideal

cycle. The following discussion refers to Adsorption Reactor A, while Adsorption Reactor B undergoes the same phases but in a different order, as commented earlier.

Pre-cooling phase: At the beginning of the cycle, the recently desorbed reactor has high temperature and pressure (P_{con}, T_{high}), and its adsorption capacity is at its lowest level w_{low}. During the pre-cooling phase (Figure 1.3a) the reactor begins to be cooled down at T_{med}, while the valves connecting it with the evaporator and the condenser are both closed. Cooling down the reactor provokes a pressure reduction, as a result of the temperature and density reduction – the latter as a consequence of vapor adsorption. The objective is to reduce the reactor pressure at the pressure of the evaporator, in order to assure that once the reactor is connected to the evaporator, the mass flux will be from the evaporator towards the reactor.

Adsorption phase: Once the reactor pressure is as low as the evaporator pressure P_{eva}, the two components are connected and the adsorption phase begins (Figure 1.3b). During this phase, the vapor in the reactor is adsorbed onto the adsorbent surface, leading to a reduction of the vapor density, and thus, the reactor pressure decreases. Therefore a pressure difference is established between the two components. Consequently, the vapor starts to flow from the evaporator to the reactor and it is adsorbed by the adsorbent. As a result, the vapor pressure in the evaporator decreases and evaporation is provoked. The latent heat of vaporization produces the desired cooling effect. Adsorption is an exothermic process and thus, the released heat increases the reactor temperature. This is disadvantageous, since the adsorption capacity decreases at higher temperature. Therefore, the cooling of the reactor at T_{med} continues throughout the adsorption phase, in order to maintain the reactor temperature low and thus, its adsorption capacity high. In the ideal cycle, the adsorption phase would continue until the adsorbent is saturated, namely, until it reaches w_{high} and cannot adsorb more. However, the adsorption rate drops dramatically while approaching equilibrium and it is of no practical interest, thus, the adsorption phase is terminated earlier.

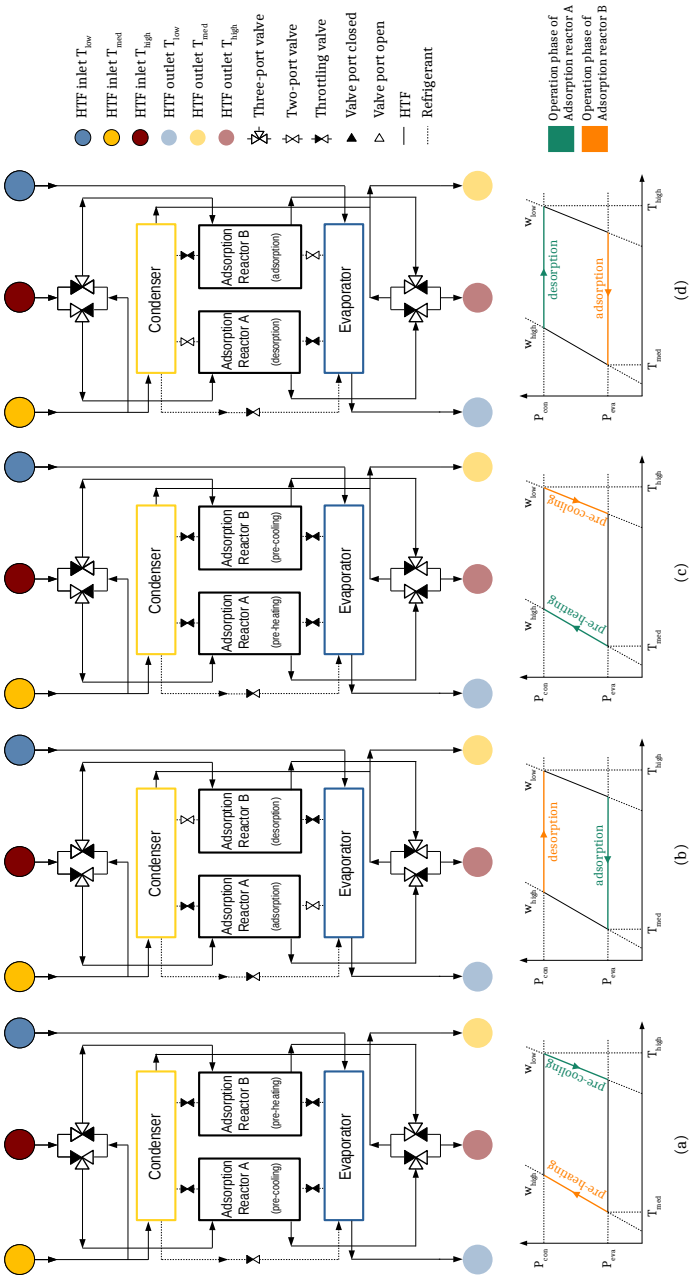

Figure 1.3: Schematic diagram and Clapeyron diagram for each phase of the adsorption cycle

Pre-heating phase: In order to remove the adsorbate from the adsorbent, and thus, reestablish its capacity to adsorb, the pre-heating and desorption phases are performed. Similarly to the pre-cooling phase, in the pre-heating phase (Figure 1.3c) the reactor is disconnected from the evaporator and remains isolated. Inversely to the pre-cooling phase, the reactor is heated at T_{high} with the objective to increase its pressure up to the condenser pressure. The reactor pressure increases, as a result of the temperature increase and density increase – the latter as a consequence of vapor desorption. The objective is to increase the reactor pressure at the pressure of the condenser, in order to assure that once the reactor is connected to the condenser, the mass flux will be from the reactor towards the condenser.

Desorption phase: Once the reactor pressure is as high as the condenser pressure P_{con}, the valve between the two components opens and the desorption phase begins (Figure 1.3d). Since desorption is an endothermic process, the reactor continues to be heated at T_{high}, until it releases the previously adsorbed mass and achieve anew w_{low}. The desorbed vapor increases the reactor pressure, and thus, vapor flows to the condenser, where it condenses to liquid, and returns to the evaporator through a throttling valve.

1.2.3 Major challenges in the design and operation of ACSs

This section presents the major challenges in the design and operation of adsorption cooling systems.

The design stage of an engineering application involves the a priori estimation of its performance. In the case of adsorption cooling systems, the system performance is quantified primarily through two performance indicators – the Specific Cooling Power (SCP) and the Coefficient of Performance (COP). The SCP represents the cooling capacity per unit mass of adsorbent. The COP represents the ratio of the cooling produced to the thermal energy input.

The quantification of these two performance indicators is remarkably essential, since two basic characteristics of the ACSs create a dichotomy over the SCP and COP. Any variation on the reactor geometry or the cycle durations will improve one of these performance indicators while it will deteriorate the other. An optimization of the reactor geometry with respect to the SCP would lead to a completely different

solution in comparison to an optimization of the geometry with respect to the COP. The same stands for the cycle durations. Sections 1.2.3.1 and 1.2.3.2 elaborate these two dichotomies of SCP and COP, whereas Section 1.2.3.3 discusses the complexities encountered in the integration of an ACS within a wider thermal system, a solar-cooled building.

1.2.3.1 Dichotomy of SCP and COP based on the reactor geometry

As it arises from the discussions above, the cooling production is proportional to the adsorption capacity, which in turn depends on the surface area that is available for adsorption. The necessity to increase the adsorption surface area leads to the utilization of porous materials. Indicatively, the silica gel under consideration at the most part of this thesis has a surface area of $720\,\mathrm{m}^2/\mathrm{g}$ [19]. Furthermore, the adsorbent porous materials are manufactured in small particles (often referred to as grains, granules or pellets) which are assembled in a packed bed configuration. Working with a packed bed of porous materials entails low intraparticle and interparticle mass transfer, as well as low heat transfer. The mass transfer resistances hinder the passage of the evaporated molecules towards the adsorption surfaces, which is translated as slow adsorption and thus, low cooling production. The heat transfer resistance can be interpreted as the difficulty to regulate the temperature of the adsorbent.

During the adsorption phase, the temperature of the reactor tends to increase due to the exothermic nature of adsorption. Since at higher temperatures the adsorption capacity decreases, it is beneficial to maintain the reactor temperature low, and thus its adsorption capacity – and consequently the cooling production – high. This task is hindered by the low heat transfer of the packed bed. In order to enhance the heat transfer rate, additional extended surfaces are incorporated on the heat exchanger solid – the metal mass which intervenes between the HTF and the adsorbent.

During the pre-heating and desorption phases, the reactor is heated at T_{high}. The heat provided during these intervals is the energy input of the ACS. The useful part of the provided energy is associated to the temperature increase of the adsorbent to T_{high} – where the adsorption capacity is low, thus desorption takes place – and the sorption enthalpy required for the endothermic desorption. However, part of the provided thermal energy is used for the temperature increase of the heat exchanger solid. This amount of thermal energy is lost in every cycle. Therefore in this case, it is desired to minimize the mass of the heat exchanger solid.

As it arises from the above, the geometrical configuration of the reactor is a determining factor for its performance. On the one hand, in order to increase the SCP, various additional extended surfaces should be incorporated to the heat exchanger solid, with the objective to enhance the heat transfer rate between the HTF and the packed bed. In this manner, its temperature is maintained low, and consequently, the adsorption rate and the cooling capacity high. On the other hand, in order to increase the COP, the heat exchanger solid should be kept minimum, with the objective to minimize the thermal energy lost in every cycle. Consequently, a conflict arises with respect to the solid mass of the heat exchanger. The design strategy should ensure enhanced heat transfer inside the packed bed, while using the minimum amount of additional mass in the heat exchanger.

It should be noted that different applications might prioritize the SCP over the COP or the inverse, or an optimum compromise might be desired. Therefore, quantification of these performance indicators under various geometrical configurations and operational parameters is considered highly useful.

1.2.3.2 Dichotomy of SCP and COP based on the cycle duration

The duration of the phases of the thermodynamic cycle also affect the SCP and COP. A short cycle duration benefits the SCP and deteriorates the COP, whereas a long cycle duration benefits the COP and deteriorates the SCP.

With respect to the SCP, the beginning of the cycle is the most productive in terms of cooling production. The newly desorbed adsorbent results in the highest adsorption rate once the reactor is connected to the evaporator. The adsorption rate – and consequently, the cooling production – gradually decreases over the course of the adsorption phase and approaches zero while equilibrium is approached. Therefore, the longer the cycle duration, the less is the average cooling capacity of the cycle.

Regarding the COP, the beginning of the cycle is the most detrimental, since the majority of the thermal input is dedicated to the temperature increase of the heat exchanger solid and the packed bed. A short cycle duration results in low COP since the majority of the invested thermal input did not result to desorption, thus it will not be reflected as adsorption and cooling in the subsequent adsorption phase. The more the cycle duration is prolonged, the more the invested thermal input results in adsorption and cooling in the subsequent adsorption phase.

Consequently, another dichotomy with respect to COP and SCP is provoked by the cycle duration. Moreover – unlike the case of the reactor geometry – the cycle duration is not predetermined for the ACS and it may vary. In fact, the cycle duration may result very useful in the adjustment of the SCP and COP, according to the instantaneous necessities and operating conditions. Therefore, the quantification of the SCP and COP under various cycle schemes is considered beneficial.

1.2.3.3 Integration of an ACS within a solar-cooled building

Apart from the intrinsic challenges for the performance of an ACS, its integration within a wider thermal system is also a challenging issue. A wider thermal system in this case is an adsorption-based solar-cooled building, therefore the ACS is coupled to the solar collectors and the thermal storage tank on the energy source side, as well as with the building on the energy demand side. This integration is not straightforward as a result of the characteristics commented below.

The inherent cyclic operation of the ACS results in a fluctuating return temperature of the secondary HTF circuits. The building, the thermal storage tank and the heat rejection device do not experience a constant or smooth HTF temperature. Furthermore, as a thermally-driven system, it is subjected to thermal inertia effects. In other words, the responsiveness of the system on variations of the operating conditions is not immediate, rather it is characterized by a certain delay.

A complexity is also encountered on the energy source side of the system. The system is equipped with solar thermal collectors, which depend on an intermittent energy source. Therefore, a thermal storage unit and an auxiliary heater are incorporated. However, there is a clear objective to prioritize solar energy. In this context, the control strategy has a crucial role in the harmonization of the ACS operation with the energy availability and the energy demand. Consequently, the study of the entire system as a whole is greatly beneficial. An improved control strategy can reduce the auxiliary thermal input, as well as the overall energy consumption of the system. It may also allow to achieve the same results using a smaller solar field, thus avoiding costs and space limitations. Lastly, the a priori study of these systems is essential in order to achieve an adequate dimensioning.

1.3 Objectives of the thesis

Computational models can contribute substantially to address the challenges presented in Section 1.2.3. Consistent computational models allow to simulate the physical phenomena involved with sufficient accuracy. They allow to study the behavior of these systems and quantify their performance under several scenarios involving geometrical and operational parameters, as well as material properties. They also allow to deepen our understanding with respect to the physics of the problem, since they provide temporal (or temporospatial where applicable) information for all the physical quantities involved, even those that cannot be measured. In comparison to actual experiments, computational simulations facilitate considerably the investigation process, since multiple scenarios can be studied in a shorted period, with less effort, lower cost, as well as with less material and energy waste.

In this context, the objective of the thesis was the development of computational models that can be used for a meaningful contribution in the collective research effort for the improvement of this technology. Two computational models were developed, approaching the adsorption cooling technology from two different perspectives.

Adsorption packed bed reactor model
As elaborated in Section 1.2.3, the design of the adsorption reactor is a crucial task, since its geometric configuration is determining for the performance of the system. The first objective of this thesis was the development of a computational model for the simulation of adsorption packed bed reactors. The model was implemented within the in-house C++/MPI CFD platform, TermoFluids. Both the packed bed and the heat exchanger solid are simulated in a conjugate manner, thus allowing to study the influence of the latter on the reactor performance. A desired capability of the model was to be able to simulate any potential reactor geometry, thus, it was implemented using three-dimensional unstructured meshes. Another important feature was the reliability of the model, hence it was imposed to verification and experimental validation assessments. Finally, an essential requirement of the model was to perform at a computational speed that is relevant for practical applications. Parallel-computing capabilities contribute to the reduction of the computational cost, along with an improved algorithm and the adoption of a multi-timestep approach.

The utilization of this model aims to contribute to the investigation of the geometrical

configuration of the reactor, through the conduction of a parametric study of five reactor geometries and their comparison. Furthermore, the model is employed for a thorough investigation of an underexplored reactor geometry, the hexagonal honeycomb adsorption reactor. The performance of the latter is quantified for various geometrical configurations and operational parameters.

Adsorption cooling system model
For the second perspective, the focus was shifted from the reactor to the entire system. The objective was to develop a reliable computational model from a component-level approach. This approach involves the modelization of the individual components with lumped-capacitance and one-dimensional models. This model was developed within NEST, an in-house, C++/MPI platform for the conjugate simulation of systems of arbitrary complexity. The capability of optimization studies was achieved by coupling the model to the generic optimization program GenOpt. Furthermore, a comprehensive simulation tool for adsorption-based solar-cooled buildings was developed, by coupling the model to NEST-buildings, a library previously developed in the CTTC laboratory.

The utilization of this model – in the context of a case study regarding a solar-cooled office – aims to study the integration of the ACS and investigate the behavior of the entire thermal system, facilitate its adequate dimensioning, as well as to explore and improve the control strategy, with the objective to maximize the environmental benefits.

1.4 Outline of the thesis

The rest of the thesis is structured as follows. Chapters 2 and 3 pertain to the study of the adsorption packed bed reactors, while Chapters 4 and 5 focus on the study of adsorption cooling systems.

Chapter 2 pertains to the presentation of the developed three-dimensional computational model for the simulation of adsorption packed bed reactors. The mathematical formulation and the numerical solution are presented, as well as the verification and validation assessments.

Chapter 3 is dedicated to the studies that have been conducted using the model

presented in Chapter 2. The first study pertains to the quantification of the SCP of the adsorption phase for five different geometries, while the second is a thorough investigation of the hexagonal honeycomb adsorption reactor.

Chapter 4 presents the development and validation of the ACS model based on lumped-capacitance and one-dimensional components. Moreover, the other models used in Chapter 5 are presented – namely, the solar collectors and thermal storage tanks, as well as the NEST-buildings library.

Chapter 5 presents the simulation of an adsorption-based solar-cooled building. Commencing from the validated ACS model, optimization studies are conducted for its cycle durations, as well as a scaling study for the determination of the ACS capacity that is sufficient to satisfy the cooling demand of the proposed building. A control strategy is implemented and progressively improved, while simulating the case study for various solar collectors areas and thermal storage capacities.

Finally, Chapter 6 summarizes the conclusions and presents the future studies of this research direction.

References

[1] United Nations. Transforming our world: the 2030 Agenda for Sustainable Development, 2015.

[2] R. Khosla, N.D. Miranda, P.A. Trotter, A. Mazzone, R. Renaldi, C. McElroy, F. Cohen, A. Jani, R. Perera-Salazar, and M. McCulloch. Cooling for sustainable development. *Nature Sustainability*, October 2020.

[3] International Energy Agency. The Future of Cooling. IEA, Paris, 2018.

[4] International Energy Agency. World Energy Outlook 2016. IEA, Paris, 2016.

[5] A. Kitous, J. Després, Assessment of the impact of climate change on residential energy demand for heating and cooling, EUR 29084 EN, Publications Office of the European Union, Luxembourg, 2018, ISBN 978-92-79-77861-2 .

[6] M. Santamouris. On the energy impact of urban heat island and global warming on buildings. *Energy and Buildings*, 82:100 – 113, 2014.

[7] United Nations, Department of Economic and Social Affairs, Population Division. World Urbanization Prospects: The 2014 Revision, Highlights, 2014.

[8] United Nations Environment Program, Ozone Secretariat. Handbook for the Montreal Protocol on Substances that Deplete the Ozone Layer, 14th edition. Nairobi, Kenya, 2020.

[9] K. Bataineh and Y. Taamneh. Review and recent improvements of solar sorption cooling systems. *Energy and Buildings*, 128:22 – 37, 2016.

[10] A.H.H. Ali. Performance assessment and gained operational experiences of a residential scale solar thermal driven adsorption cooling system installed in hot arid area. *Energy and Buildings*, 138:271 – 279, 2017.

[11] R. Sekret and M. Turski. Research on an adsorption cooling system supplied by solar energy. *Energy and Buildings*, 51:15 – 20, 2012.

[12] K. Habib, B. Choudhury, P.K. Chatterjee, and B.B. Saha. Study on a solar heat driven dual-mode adsorption chiller. *Energy*, 63:133 – 141, 2013.

[13] R.P. Sah, B. Choudhury, R.K. Das, and A. Sur. An overview of modelling techniques employed for performance simulation of low–grade heat operated adsorption cooling systems. *Renewable and Sustainable Energy Reviews*, 74:364 – 376, 2017.

[14] International Union of Pure and Applied Chemistry (IUPAC). Glossary of terms used in physical organic chemistry, 1994.

[15] F. Rouquerol, J. Rouquerol, K.S.W. Sing, P. Llewellyn, and G. Maurin. *Adsorption by Powders and Porous Solids*. Elsevier, 2nd edition, 2014.

[16] A. Freni, B. Dawoud, L. Bonaccorsi, S. Chmielewski, A. Frazzica, L. Calabrese, and G. Restuccia. *Characterization of Zeolite-Based Coatings for Adsorption Heat Pumps*. Springer, 2nd edition, 2015.

[17] M. Suzuki. *Adsorption Engineering*. Copublished by: Kodansha, Tokyo and Elsevier Science Publishers, Amsterdam, 1990.

[18] A. Christy. New insights into the surface functionalities and adsorption evolution of water molecules on silica gel surface: A study by second derivative near infrared spectroscopy. *Vibrational Spectroscopy*, 54(1):42 – 49, 2010.

[19] X. Wang, W. Zimmermann, K.C. Ng, A. Chakraboty, and J.U. Keller. Investigation on the isotherm of silica gel+water systems. *Journal of Thermal Analysis and Calorimetry*, 76(2):659 – 669, 2004.

2

Development of a computational model for adsorption packed bed reactors

Contents of this chapter have been included in :
- G. Papakokkinos, J. Castro, J. Lopez and A. Oliva, A generalized computational model for the simulation of adsorption packed bed reactors – Parametric study of five reactor geometries for cooling applications, *Applied Energy*, 235 (2), 409-427, 2018
- G. Papakokkinos, J. Castro, C. Oliet and A. Oliva, Computational investigation of the hexagonal honeycomb adsorption reactor for cooling applications, *Under review*

2.1 Introduction

This chapter presents the development of a computational model for the simulation of adsorption packed bed reactors. The latter is the most vital component of an adsorption cooling system (ACS). Its design is a crucial task since it has a determining impact on the performance of the system. As elaborated in Section 1.2.3, the reactor design influences the Coefficient of Performance (COP) and the Specific Cooling Power (SCP) in a distinct manner. Distributed-parameter models may assist the design process significantly. Thus, one of the thesis' scopes is the development of a computational model for adsorption packed bed reactors, that is capable to simulate any potential geometry with sufficient accuracy – as well as with a computational cost that allows its utilization for engineering applications. The developed model was employed for the numerical studies presented in Chapter 3.

Section 2.2 presents a literature review with respect to distributed-parameter models of adsorption packed bed reactors. Section 2.3 is dedicated to the mathematical formulation of the model, while Section 2.4 pertains to the presentation of its numerical solution. Section 2.5 presents the verification and validation assessments of the model.

2.2 Literature review

Several distributed-parameter models can be encountered in the literature, with respect to the simulation of adsorption packed bed reactors. The scope of the related studies is diverse. These research scopes include: (i) the study of the validity of modeling strategies, such as the comparison of the local thermal equilibrium approach to the nonequilibrium approach [1], the applicability of the isobaric assumption [2] and the effect of different intraparticle mass transfer kinetics modeling methods [3], (ii) the experimental validation of numerical models regarding the adsorption refrigeration tube [4, 5], the tubular reactor with axial and radial fins [6, 7] and the annular adsorption reactor [8, 9], (iii) to study the performance of the ACS for different adsorption pairs [10, 11], (iv) to investigate the thermodynamic cycle configurations adopting heat recovery and mass recovery strategies [12–14], (v) the investigation of the influence of the reactor design on its performance. The latter is the topic of the literature review of Chapter 3, whereas the literature review of this chapter focuses on the modeling process.

Table 2.1 presents an extensive, though not exhaustive, summary of the distributed-parameter models published in the peer-reviewed literature [1–29]. For conciseness, numerical models used by the same research group and appear multiple times in the literature are listed only once. Simulation models related to adsorption packed bed reactors which are embedded in the solar collector such as [30, 31] are not included in the summary, since they are specific to solar energy source, as well as to ice production applications. Since numerical models are easily adaptable to other adsorption pairs, the adsorption pair and isotherm are not included in the presented summary. It should be noted that the adsorption packed bed reactors are used throughout a wide spectrum of industrial and environmental applications. Examples include gas storage (hydrogen [32], methane [33], carbon dioxide [34]), gas separation [35], carbon capture [36] and water treatment and purification [37]. Although the presented model is extensible to these applications, Table 2.1 is limited to numerical studies related to adsorption cooling, desalination and heat storage.

Table 2.1 summarizes the most important features related to the reliability, extensibility and complexity of the models. The features summarized in Table 2.1 are discussed below with the intention to reveal some common tendencies, important distinctions and limitations of the current state-of-the-art regarding the numerical modeling of adsorption packed bed reactors.

The experimental validation is categorized between local and global. Global experimental validation is performed at component level, based on experimental information outside the packed bed, such as the temporal evolution of the outlet temperature of the HTF, the exterior wall temperature of the packed bed and the overall adsorption uptake. Local experimental validation is based on experimental information within the packed bed, in particular, the temporal evolution of the temperature on 3-4 different points inside the packed bed. The local experimental validation is considered more rigorous since it challenges the distributed-parameter character of the models and therefore it increases their reliability for design purposes. The majority of the experimentally validated models are based on the global approach, while only few models are validated based on the local approach. Approximately one third of the presented numerical models are not experimentally validated, hence they are less applicable to studies aiming quantitatively accurate results.

The models are also characterized by whether they solve numerically the solid heat exchanger. When the solid is not taken explicitly into account the influence of its shape, size as well as its thermal properties cannot be appreciated and the model may be used to study only the packed bed using fixed boundary conditions. When the solid is numerically solved, the conjugate heat transfer is solved and the influence of the heat exchanger can be evaluated, studied and improved.

The spatial discretization of the domain is also a significant factor regarding the applicability of the model. From Table 2.1, it can be observed that the majority of the models are based on cylindrical coordinates, hence they are restricted to reactor geometries of cylindrical shape. Structured meshes are subjected to geometric limitations with respect to the simulated geometry, whereas unstructured meshes can be used in order to simulate any potential geometry. Furthermore, unstructured meshes allow higher flexibility over the mesh density distribution, which can be adapted spatially to the physical phenomena involved. None of the studies based on either in-house or commercial software models explicitly reports the use of unstructured meshes, although it can be assumed that commercial software models have this capability.

The dimensionality of a model represents its capacity to be applied independently to the presence of geometric symmetry or symmetry of the boundary conditions. The applicability of one-dimensional and two-dimensional models depends on the presence of such symmetries, while three-dimensional models can be applied in any case. Only few of the presented models are three-dimensional, whereas the majority

are either one-dimensional or two-dimensional.

Table 2.1 also summarizes the geometry of the packed bed reactor that was simulated by the referenced models. Annular reactor is noted when the HTF passes through the exterior of the cylinder and the vapor enters through its center. The presence of fins and their type is also reported.

The vast majority of the reported distributed-parameter models use the Linear Driving Force (LDF) model to describe the intraparticle mass transfer resistance. A few models use the equilibrium approach, which neglects the adsorption kinetics, assuming adsorption equilibrium. The solid diffusion model (SD, or Fickian diffusion model) is generally considered to be the most accurate [24], however its computational cost is much higher. While the LDF model assumes lumped temperature and adsorption capacity over the entire adsorbent particle, the SD model requires spatial discretization of the particle and numerical solution of the heat transfer and adsorbate diffusion within the adsorbent. This applies for each control volume of the mesh, increasing significantly the computational cost of the simulations, especially in three-dimensional cases. Moreover, the spatial discretization at the particle level decreases the acceptable timestep. Chabani et al. [3] compared the three approaches and concluded that outside their validity range, the LDF model underestimates the system performance and the equilibrium approach overestimates it, with respect to the diffusion model.

Regarding the interparticle mass transfer resistance, some studies assume uniform pressure throughout the packed bed [3, 16]. This isobaric assumption is not valid in the case of large packed beds or small adsorbent particle sizes [2], where pressure gradients are considerable. The most common approach is to use momentum equations for porous media such as the Darcy equation, the Ergun equation and the Darcy-Brinkmann equation. In [7, 29], where commercial CFD software were employed, the use of the Navier-Stokes equations with a sink term in the momentum equation was reported.

With respect to the heat transfer within the packed bed, two approaches are encountered in the literature; the most commonly used is the Local Thermal Equilibrium (LTE), while few works use the Local Thermal Nonequilibrium (LTNE) [1, 5, 18, 25, 26]. The LTE approach assumes that the gas and solid phases have the same temperature, therefore one energy equation is solved. This approach requires the use of effective thermal conductivity and effective specific heat capacity, assuming that the heat transfer resistance between the two phases is negligible. The LTNE approach

distinguishes the temperature of the two phases, and therefore, two energy equations are solved. Each energy equation has a source term for the heat transfer between the two phases. Mhimid [1] compared the two approaches for the desorption phase. Although no significant difference was found on the total desorbed mass between the two approaches, he concluded that the LTE is not valid throughout the entire domain. Using the LTNE approach, he observed temperature differences up to 10 °C between gas and solid. Furthermore, the conclusion of the small discrepancy between the desorbed mass calculated by the two approaches is specific to the particularities of the studied case (geometry, dimensions, adsorption pair, desorption phase, operating conditions etc.) and cannot be generalized.

Based on the above discussion and with an overview of the Table 2.1, it becomes clear that there is a great interest for the numerical modeling of adsorption reactors. However, the previously reported models have significant limitations with respect to the simulated reactor geometry. The majority is limited only to cylindrical geometries. Moreover, only few reported models are three-dimensional, whereas the rest depend on the presence of symmetries. Furthermore, most of the reported models are either not experimentally validated, or their experimental validation is performed at component level, and thus, the distributed-parameter character of the model is not questioned. In addition, many reported models simulate only the packed bed and they do not explicitly solve the heat exchanger, thus, they cannot be used for the study and the improvement of the reactor performance.

In the context of this thesis, a generalized three-dimensional computational model was developed, capable to simulate any potential reactor geometry. The model exhibits reasonably good agreement against experimental results, with respect to the temporal evolution of the temperature at four points inside the packed bed reactor [7]. Both the packed bed and the solid heat exchanger domains are simulated in a dynamic conjugate manner, thus allowing to study the influence of the latter on the reactor performance. The intraparticle and interparticle mass transfer resistance were modeled using the LDF model and the Ergun equation, respectively. The heat transfer within the packed bed was modeled by the LTNE approach, thus two energy equations were solved. The spatial discretization of the governing equations was implemented using three-dimensional unstructured meshes. Versatility is provided regarding the adsorption pair and the material of the heat exchanger. The computations can be distributed in various CPUs, allowing the simulation of relatively large domains in reasonable computational time. The numerical model is implemented within the

in-house C++/MPI CFD platform, TermoFluids [38]. Coding the model rather than using commercial software provides the freedom to fully define the problem mathematically, as well as to implement numerical algorithms that assure stability and accuracy at the lowest possible computational cost.

Table 2.1: Summary of distributed-parameter models of adsorption packed bed reactors

Reference	Year	Exp. validation	Solid Simul.	Spatial discretization	Dim.	Reactor geometry	Intraparticle mass transfer	Interparticle mass transfer	Heat transfer
L.M.Sun et al. [11]	1995	None	Yes	Cylindrical	1d	Tubular	Equilibrium	Ergun	LTE
A.Mhimid [1]	1998	Global	No	Cylindrical	2d	Annular	LDF	Darcy	Both
L.Z.Zhang [6]	1999	Local	Yes	Cylindrical	3d	Tubular (axial fins)	LDF	Darcy	LTE
L.Luo [8]	2000	Local	No	Cylindrical	1d	Annular	Equilibrium	Diffusion	LTE
M.H.Chabani [3]	2002	None	Yes	Cylindrical	1d	Annular	Equil/LDF/SD	Isobaric	LTE
L. Marletta [15]	2002	None	Yes	Cylindrical	2d	Tubular (coated)	Equilibrium	Ergun	LTE
H.T.Chua [12]	2004	Global	Yes	Cylindrical	2d	Tubular (radial fins)	LDF	N/A	LTE
K.C.Leong [14]	2004	None	Yes	Cylindrical	2d	Tubular	LDF	Darcy	LTE
E.Voyiatzis [16]	2008	None	Yes	Cylindrical	1d	Tubular	LDF	Isobaric	LTE
W.D.Wu [17]	2009	Global	Yes	Cylindrical	2d	Annular ads. tube	LDF	Darcy	LTE
B.B.Saha [10]	2009	Global	Yes	Cylindrical	2d	Tubular (radial fins)	LDF	N/A	LTE
F.B.Cortés [18]	2009	Global	No	Cylindrical	1d	Annular	LDF	Darcy	LTNE
H.Niazmand [19]	2012	Global	Yes	Cylindrical	2d	Tubular (radial fins)	LDF	Ergun	LTE
Y.L.Zhao [4]	2012	Local	No	Cylindrical	1d	Annular ads. tube	Equilibrium	Diffusion	LTE
Y.L.Zhao [5]	2012	Local	No	Cylindrical	1d	Annular ads. tube	LDF	Darcy	LTNE
G.G.Ilis [2]	2013	None	No	Cylindrical	1d	Annular	LDF	Isobaric/Darcy	LTE
M.Mahdavikhah [20]	2013	Global	Yes	Structured Non-orthog.	3d	Tubular (square radial fins)	LDF	Darcy	LTE
H.Demir [21]	2013	None	No	Cylindrical	1d	Annular	LDF	Darcy	LTE
M.Duquesne [22]	2014	Global	No	Cylindrical	2d	Tubular	Equilibrium	Darcy	LTE
J.W.Wu [9]	2014	Local	No	Cylindrical	1d	Annular	LDF	Darcy	LTE
H.R.Ramji [23]*	2014	Global	No	N/A	N/A	Tubular (axial fins)	LDF	N/A	LTE
S.W.Hong [24]*	2015	Global	Yes	Cylindrical	2d	Tubular (radial fins)	SD	Diffusion	LTE
İ.Solmuş [25]	2015	None	No	Cylindrical	2d	Annular	LDF	Darcy	LTNE
Q.W.Pan [13]*	2015	None	Yes	Cylindrical	2d	Tubular (radial fins)	N/A	Isobaric	LTE
S.Jribi [7]*	2017	Local	Yes	N/A	2d	Tubular (radial fins)	LDF	Navier-Stokes	LTE
R.Mohammed [26]	2017	Global	No	Cartesian	3d	Other	LDF	Darcy-Brink.	LTNE
M.M.Kowsari [27]	2018	Global	Yes	Structured Non-orthog.	3d	Finned flat tube	LDF	Darcy	LTE
B.Golparvar [28]	2018	Global	Yes	Cylindrical	3d	Tubular (radial/axial)	LDF	Darcy	LTE
M.B.Elsheniti [29]*	2019	Global	Yes	Cylindrical	2d	Tubular (radial fins)	LDF	Navier-Stokes	LTE

**commercial CFD software was used*

2.3 Mathematical formulation

The mathematical formulation consists in the task of describing the physical phenomena involved through mathematical equations. In the presented model, two computational domains are involved, the adsorption packed bed (PB) and the solid heat exchanger (HX). Figure 2.1 pertains to a conceptual illustration of the computational domains. Illustrations of the five studied reactor geometries can be found in Chapter 3. [1] The following subsections present the mathematical formulation of the two domains and their boundary conditions.

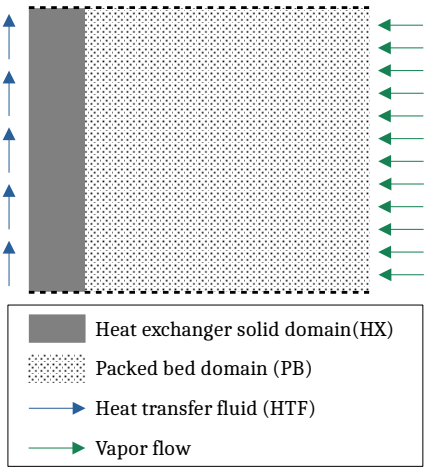

Figure 2.1: Conceptual illustration of the two computational domains

For the construction of the model, a series of assumptions has been considered. These assumptions are: (i) the shape and size of the adsorbent particles, as well as the void fraction, are uniform throughout the packed bed, (ii) the adsorbent is assumed to be an isotropic porous medium, hence its surface porosity is equivalent to its volume porosity [39], (iii) the specific heat capacity of the adsorbed phase corresponds to the liquid phase, (iv) the HTF temperature is constant, (v) there are no heat losses to the environment, (vi) the adsorptive gas behaves as an ideal gas and (vii) when the reactor is connected to the evaporator or condenser, their respective temperature and

[1] Figure 3.1 illustrates the studied reactor geometries, Figure 3.2 the computational domains after applying symmetries and periodicities and Figure 3.3 shows their boundary conditions.

pressure are considered constant. Regarding the latter assumption, the developed models provide the capability to couple the reactor with simple models of evaporator and condenser. However, such approach is avoided in order not to condition the reactor performance results by aspects which are not related to the reactor, such as the dimensioning of the evaporator and the condenser.

2.3.1 Adsorption packed bed model

The adsorption packed bed domain is comprised by two phases, the solid adsorbent and the adsorptive gas.

2.3.1.1 Adsorption equilibrium

The adsorption equilibrium capacity is the amount of adsorbate mass per unit mass of adsorbent, that is adsorbed onto the adsorbent when the pressure and temperature are maintained constant for a relatively long period. The adsorption equilibrium capacity w^* is calculated through the adsorption isotherm. Unless stated otherwise, the Tóth adsorption isotherm is employed in this study, as derived experimentally by Wang et al. [40], for the adsorption pair of water and silica gel type RD.

$$w^*(P,T) = \frac{K_0 \exp(\Delta H_{\text{ads}}/(R_g T))P}{\left[1 + \left(\frac{K_0}{q_m} \exp(\Delta H_{\text{ads}}/(R_g T))P\right)^{\tau}\right]^{1/\tau}} \tag{2.1}$$

The input parameters of the Tóth isotherm are listed in Table 3.2. The model allows the implementation of additional adsorption isotherms. For further information on adsorption isotherms, the reader is referred to [41].

2.3.1.2 Adsorption kinetics

The information provided by the adsorption isotherm pertains to the equilibrium capacity. When the conditions are altered, the adsorbed mass w does not change instantaneously to the equilibrium capacity w^* that corresponds to the new conditions. The adsorbed mass moves from its instantaneous value towards the equilibrium capacity which corresponds to the instantaneous conditions. The velocity of this

process is described by the adsorption kinetics. In this study, the adopted approach for the mathematical description of the adsorption kinetics is the LDF model [42]. For spherical particles, the LDF model is expressed as:

$$\frac{dw}{dt} = \frac{60 D_e}{d_{\mathrm{p}}^2}(w^* - w) \tag{2.2}$$

where D_e is the effective diffusivity, calculated by the Arrhenius equation, based on the temperature, the reference diffusivity D_0 and the activation energy E_a.

$$D_e = D_0 \exp(-E_a/(RT)) \tag{2.3}$$

2.3.1.3 Vapor mass conservation equation

The vapor mass inside a control volume varies as a result of vapor fluxes on its boundaries and sorption phenomena. The vapor mass conservation is expressed by the continuity equation of the specific mass, namely, the vapor density.

$$\underbrace{\varepsilon_{\mathrm{b}} \frac{\partial \rho_{\mathrm{g}}}{\partial t}}_{\mathrm{i}} + \underbrace{\nabla \cdot (\rho_{\mathrm{g}} \vec{u})}_{\mathrm{ii}} + \underbrace{\rho_{\mathrm{s}}(1-\varepsilon_{\mathrm{t}}) \frac{\partial w}{\partial t}}_{\mathrm{iii}} = 0 \tag{2.4}$$

The term (2.4-i) is the accumulation term and represents the rate of mass change within the control volume. The term (2.4-ii) is the convective term and represents the net mass flux at the boundaries of the control volume. The superficial velocity $\vec{u}$ is calculated through equation 2.18. The term (2.4-iii) is the sink/source term and represents the amount of vapor which leaves or enters the vapor phase of the control volume, depending on whether adsorption or desorption takes place. The total void fraction ε_{t} is a function of the bed void fraction ε_{b} and the particle porosity ε_{p}. It is calculated as:

$$\varepsilon_{\mathrm{t}} = \varepsilon_{\mathrm{b}} + (1 - \varepsilon_{\mathrm{b}})\varepsilon_{\mathrm{p}} \tag{2.5}$$

The vapor mass inside the control volume dV is calculated as $\varepsilon_{\mathrm{b}} \rho_{\mathrm{g}} \mathrm{dV}$, while the solid mass inside the control volume is calculated as $\rho_{\mathrm{s}}(1 - \varepsilon_{\mathrm{t}})\,\mathrm{dV}$.

2.3.1.4 Energy conservation equations

For the mathematical description of the heat transfer inside the packed bed, the local thermal nonequilibrium approach is adopted. This approach considers that the gas and solid phases have distinct temperatures and thus, a separate energy conservation equation is solved for each phase.

Gas phase The energy conservation equation for the gas phase is expressed as:

$$\underbrace{\varepsilon_b \frac{\partial(\rho_g h_g)}{\partial t}}_{\text{i}} + \underbrace{\nabla \cdot (\rho_g \vec{u} h_g)}_{\text{ii}} = \underbrace{\varepsilon_b \lambda_g \nabla^2 T_g}_{\text{iii}} + \underbrace{a U_{pi}(T_s - T_g)}_{\text{iv}} - \underbrace{\rho_s (1-\varepsilon_t) \frac{\partial w}{\partial t} h_g}_{\text{v}} \tag{2.6}$$

The term (2.6-i) is the accumulation term, representing the temporal variation of energy inside the gas phase of the control volume. The term (2.6-ii) is the convective term, which represents the transportation of energy across the boundary of the control volume, as a result of mass fluxes. The term (2.6-iii) is the diffusive term, representing the energy transfer across the boundaries of the control volume, as a result of the temperature difference. The term (2.6-iv) represents the convective heat transfer which takes place between the solid and the gas phase of the control volume. The exchange surface area per unit volume a and the heat transfer coefficient U_{pi} are calculated using the equations 2.14 and 2.15, respectively. Finally, the term (2.6-v) is the thermal energy of the mass leaving or entering the gas phase of the control volume, as a result of adsorption or desorption.

The partial derivative of the accumulation term is further developed as illustrated below, in equation 2.7. The product rule is applied and the accumulation term is expressed by the two components responsible for the total enthalpy change. On the one hand, the sensible heat, manifested as temperature change, and on the other hand, the thermal mass change due to the mass variation inside the gas phase of the control volume.

$$\frac{\partial(\rho_g h_g)}{\partial t} = \rho_g \frac{\partial h_g}{\partial t} + h_g \frac{\partial \rho_g}{\partial t} = \rho_g c_{p_g} \frac{\partial T_g}{\partial t} + h_g \frac{\partial \rho_g}{\partial t} \tag{2.7}$$

Substituting equation 2.7 in equation 2.6, the final form of the energy conservation equation for the gas phase of the control volume is obtained.

$$\varepsilon_b \rho_g c_{p_g} \frac{\partial T_g}{\partial t} + \varepsilon_b h_g \frac{\partial \rho_g}{\partial t} + \nabla \cdot (\rho_g \vec{u} h_g) = \varepsilon_b \lambda_g \nabla^2 T_g + a U_{pi} (T_s - T_g) - \rho_s (1 - \varepsilon_t) \frac{\partial w}{\partial t} h_g \tag{2.8}$$

Although the differential equation 2.8 can be expressed in a simpler form by introducing the mass conservation equation (equation 2.4), equation 2.8 is adopted due to the convenience of its numerical integration.

Solid phase With respect to the energy conservation equation of the solid phase, two widely adopted assumptions are considered. The first assumption is that the total enthalpy of the "mixture" of adsorbent and adsorbate H_{wa} is assumed to be the sum of the enthalpies of the individual components - the dry adsorbent H_{da} and the adsorbed phase H_{ap}. Based on this assumption and by expressing the adsorbed phase mass m_{ap} as the product of the solid adsorbent dry mass m_{da} and the adsorption concentration w, the following expression for the total enthalpy inside the control volume is obtained:

$$H_{wa} = H_{da} + H_{ap} = m_{da} h_{da} + m_{ap} h_{ap} = m_{da} h_{da} + m_{da} w h_{ap} \tag{2.9}$$

The second assumption is that the specific heat of the adsorbed phase is equal to the specific heat of the liquid phase. Based on this assumption and equation 2.9, the accumulation term is developed below. Firstly, the product rule is applied on the derivative regarding the adsorbed phase, since both the specific enthalpy h_{ap} and the adsorbed mass quantity w vary. Then, the assumption of the specific heat of the liquid phase is applied. Finally, a specific heat capacity for both the dry adsorbent and the adsorbed phase is employed, defined as $c_{p_s} = (c_{p_{da}} + w c_{p_l})$, and the dry adsorbent density ρ_{da} is expressed by the more common ρ_s.

$$\begin{aligned} \frac{\partial (\rho_{da} h_{da})}{\partial t} + \frac{\partial (\rho_{da} w h_{ap})}{\partial t} =& \rho_{da} \frac{\partial h_{da}}{\partial t} + \rho_{da} w \frac{\partial h_{ap}}{\partial t} + \rho_{da} h_{ap} \frac{\partial w}{\partial t} \\ =& \rho_{da} c_{p_{da}} \frac{\partial T_s}{\partial t} + \rho_{da} w c_{p_l} \frac{\partial T_s}{\partial t} + \rho_{da} h_{ap} \frac{\partial w}{\partial t} \\ =& \rho_s c_{p_s} \frac{\partial T_s}{\partial t} + \rho_s h_{ap} \frac{\partial w}{\partial t} \end{aligned} \tag{2.10}$$

A first form of the solid energy conservation equation is presented below:

$$\underbrace{\rho_s(1-\varepsilon_t)c_{p_s}\frac{\partial T_s}{\partial t}}_{\text{i}}+\underbrace{\rho_s(1-\varepsilon_t)h_{ap}\frac{\partial w}{\partial t}}_{\text{ii}}=\underbrace{(1-\varepsilon_b)\lambda_s\nabla^2 T_g}_{\text{iii}}+\underbrace{aU_{pi}(T_g-T_s)}_{\text{iv}}+\underbrace{\rho_s(1-\varepsilon_t)\frac{\partial w}{\partial t}h_g}_{\text{v}} \tag{2.11}$$

The terms (2.11-i) and (2.11-ii) represent the accumulation term, as developed in equation 2.10. The term (2.11-i) represents the enthalpy change inside the control volume as a result of temperature change, while the term (2.11-ii) represents the enthalpy change as a result of the variation of the adsorbed mass. The term (2.11-iii) represents the conductive heat transfer at the boundaries of the control volume, as a consequence of temperature difference. The term (2.11-iv) is the sensible heat exchanged with the gas phase of the control volume. The term (2.11-v) is the enthalpy of the vapor crossing the boundary gas-solid during sorption.

As it can be observed, the gas and solid energy equations are linked through the terms (2.6-iv) and (2.11-iv), which represent the convective heat transfer between the solid and gas phase – as well as through the terms (2.6-v) and (2.11-v) which represent the thermal energy exchanged through the mass transfer, which takes place as a result of sorption.

The difference between the terms (2.11-ii) and (2.11-v) represents the enthalpy change that the adsorbate undergoes, from its gaseous state to the adsorbed state. This enthalpy difference can be expressed by equation 2.12, as the sum of its two components. The term (2.12-i) represents the sensible heat energy which is exchanged as its temperature changes from T_g to T_s. The term (2.12-ii) pertains to the enthalpy of adsorption which is released due to the exothermic nature of adsorption.

$$h_g-h_{ap}=\underbrace{c_{p_g}(T_g-T_s)}_{\text{i}}+\underbrace{\Delta H_{ads}}_{\text{ii}} \tag{2.12}$$

Substituting equation 2.12 in equation 2.11, the following form of the energy conservation equation for the solid phase is obtained:

$$\rho_s(1-\varepsilon_t)c_{p_s}\frac{\partial T_s}{\partial t}=(1-\varepsilon_b)\lambda_s\nabla^2 T_g+aU_{pi}(T_g-T_s)+\rho_s(1-\varepsilon_t)\frac{\partial w}{\partial t}\left[\Delta H_{ads}+c_{p_g}(T_g-T_s)\right] \tag{2.13}$$

Convective heat transfer between the solid and gas phase As mentioned earlier, the two energy conservation equations include a term $aU_{\mathrm{pi}}\Delta T$, describing the convective heat transfer per unit volume between them, as a result of their temperature difference. The parameter a is the specific exchange surface area per unit volume [$\mathrm{m}^2/\mathrm{m}^3$]. For a bed of spherical particles, it is calculated by equation 2.14 [39].

$$a = 6\,(1-\varepsilon_{\mathrm{b}})/d_{\mathrm{p}} \tag{2.14}$$

The heat transfer coefficient between the two phases is determined through the Nusselt number, as in equation 2.15 [43].

$$\mathrm{Nu} = 2 + 1.1\mathrm{Pr}^{0.33}\mathrm{Re}^{0.6} = \frac{U_{\mathrm{pi}}d_{\mathrm{p}}}{\lambda_{\mathrm{g}}} \tag{2.15}$$

The Reynolds and the Prandtl number are calculated as:

$$\mathrm{Re} = \frac{d_{\mathrm{p}}\rho_{\mathrm{g}}\,|\vec{u}|}{\mu_{\mathrm{g}}} \text{ and } \mathrm{Pr} = \frac{c_{p_{\mathrm{g}}}\mu_{\mathrm{g}}}{\lambda_{\mathrm{g}}} \tag{2.16}$$

2.3.1.5 Pressure equation

The pressure of the adsorptive gas is evaluated based on the ideal gas law, as a function of the gas temperature and gas density.

$$P = \rho_{\mathrm{g}}R_{\mathrm{g}}T_{\mathrm{g}} \tag{2.17}$$

A comparative study was undertaken between the results of the ideal gas law and the methodology of the International Association for the Properties of Water and Steam [44]. The pressure was calculated in the pressure range of 1-4.8 kPa and temperature range of 30-80 °C. The results revealed a relative discrepancy in the range of 0.00018-0.002. This discrepancy is considered acceptable, taking into consideration the drastically lower computational cost of the ideal gas law.

2.3.1.6 Momentum equation

The interparticle mass transfer is calculated through the momentum equation for porous media. In this work, the Ergun equation - an extension of the Darcy equation - is employed [11, 39]. The Ergun equation allows to evaluate the velocity field based on the pressure gradient.

$$\vec{u} + \frac{\rho_g}{\mu_g} K_E \vec{u}|\vec{u}| = -\frac{K_D}{\mu_g} \nabla P \tag{2.18}$$

where permeability K_D and Ergun inertia-related parameter K_E are calculated as:

$$K_D = \frac{d_p^2 \varepsilon_b^3}{150(1-\varepsilon_b)^2} \text{ and } K_E = \frac{1.75 d_p}{150(1-\varepsilon_b)} \tag{2.19}$$

2.3.2 Heat exchanger solid model

For the heat exchanger solid domain the heat equation is applied.

$$\rho_{hx} c_{p_{hx}} \frac{\partial T_{hx}}{\partial t} = \lambda_{hx} \nabla^2 T_{hx} \tag{2.20}$$

2.3.3 Boundary conditions

The mathematical formulation requires the definition of the boundary conditions of the two domains. Figure 3.3 illustrates these boundary conditions for all the geometries studied in the context of this thesis. For the computational domain under consideration, the following boundaries are encountered.

Reactor - Vapor chamber The interface between the packed bed domain and the vapor chamber is the open boundary, where the gas mass fluxes take place during the adsorption and desorption phases. During the pre-cooling and pre-heating phases, this boundary is considered closed and Neumann boundary condition is imposed for the pressure, as well as for the gas and solid temperatures. It should be noted that no-slip boundary condition applies for velocity when the pressure gradient is zero.

$$\frac{\partial P}{\partial \hat{n}} = \frac{\partial T_g}{\partial \hat{n}} = \frac{\partial T_s}{\partial \hat{n}} = 0 \tag{2.21}$$

During the adsorption and desorption phases, a Dirichlet boundary condition is imposed for pressure, according to the pressure of the evaporator and condenser, respectively (equation 2.22a). The gas temperature on this boundary depends on the direction of the flow. If the mass flow is inwards, then the gas temperature takes the value of the inlet gas, namely, the evaporator temperature during adsorption or the condenser temperature during desorption (backflow case for the latter). If the mass flow is outwards, a Neumann boundary condition is applied (equation 2.22b). For the solid temperature, Neumann boundary condition is imposed (equation 2.22c). The gas density is calculated via the ideal gas law, according to the local pressure and temperature.

$$P \ : \ \begin{cases} P = P_{\text{eva}} \text{ for adsorption} \\ P = P_{\text{con}} \text{ for desorption} \end{cases} \tag{2.22a}$$

$$T_{\text{g}} \ : \ \begin{cases} T_{\text{g}} = T_{\text{eva/con}} & \text{when } \dot{m} \text{ is inwards} \\ \dfrac{\partial T_{\text{g}}}{\partial \hat{n}} = 0 & \text{when } \dot{m} \text{ is outwards} \end{cases} \tag{2.22b}$$

$$T_{\text{s}} \ : \ \frac{\partial T_{\text{s}}}{\partial \hat{n}} = 0 \tag{2.22c}$$

With respect to the interface of the heat exchanger solid and the vapor chamber, this only pertains to a small surface (tip of the fin) and it would exchange thermal energy via natural convection. In this context, the thermal energy exchanged between the vapor chamber and the heat exchanger solid is neglected and Neumann boundary condition is applied.

$$\frac{\partial T_{\text{hx}}}{\partial \hat{n}} = 0 \tag{2.23}$$

Reactor - HTF channel This applies only for the heat exchanger solid. The heat flux between the latter and the heat transfer fluid is calculated with a Newton boundary condition (equation 2.24). The convective heat transfer coefficient U_{HTF} can be calculated based on the flow regime, the fluid properties and the channel geometry, as reported in [45].

$$\lambda_{\text{hx}} \frac{\partial T_{\text{hx}}}{\partial \hat{n}} = U_{\text{HTF}} (T_{\text{HTF}} - T_{\text{hx}}) \tag{2.24}$$

Reactor symmetries On the boundaries where geometrical symmetry applies, Neumann boundary condition is imposed for all variables:

$$\frac{\partial P}{\partial \hat{n}} = \frac{\partial T_g}{\partial \hat{n}} = \frac{\partial T_s}{\partial \hat{n}} = \frac{\partial T_{hx}}{\partial \hat{n}} = 0 \tag{2.25}$$

Interface between packed bed and heat exchanger The heat flux between the packed bed and the heat exchanger domain at their interface is calculated based on equation 2.26, using the contact heat transfer coefficient U_{if} and the local temperature difference.

$$\dot{q}_{if} = \frac{\dot{Q}_{if}}{A_{if}} = U_{if}\,(T_{hx} - T_s) \tag{2.26}$$

On the packed bed side, there is some ambiguity with respect to how the exchanged heat flux is distributed between the solid and the gas phase [39]. In studies related to the experimental derivation of the contact heat transfer coefficient for silica gel [46,47], the reported values pertain to the U_{if} between the heat exchanger solid and the solid phase of the packed bed (adsorbent grains). In [47], it was hypothesized that the heat flux between the heat exchanger solid and the adsorbent grains occurs partially through the stagnant vapor and that the reported values for U_{if} correspond to an apparent heat transfer coefficient. Consequently, since these reported values include the heat flux through the stagnant vapor, in the context of this study it is assumed that the heat flux between the two domains is exchanged exclusively between the heat exchanger and the solid phase of the packed bed. For the remaining variables of the packed bed, Neumann boundary condition is applied.

$$\frac{\partial P}{\partial \hat{n}} = \frac{\partial T_g}{\partial \hat{n}} = 0 \tag{2.27}$$

2.4 Numerical solution

For the numerical solution, the governing equations are discretized in space and time. The developed numerical model is implemented within the in-house C++/MPI CFD platform, TermoFluids [38].

Spatial discretization Using the finite volume method, the domains are discretized using collocated, unstructured, three-dimensional meshes. The diffusive terms are discretized based on a second-order central difference scheme. The convective terms are discretized using the upwind scheme. For the calculation of gradients, the least-squares method is employed. The interface between the two domains is discretized with coinciding meshes.

Temporal discretization The transient terms are discretized based on an Euler implicit scheme. A multi-timestep approach is adopted, reducing significantly the computational cost, without compromising the accuracy of the solution. Preliminary studies were performed in order to assess whether to employ an explicit scheme (lower timestep, one iteration per timestep) or an implicit scheme (higher timestep more iterations per timestep). The computational cost of the latter was proven lower, thus implicit temporal discretization was employed.

Numerical methods The energy conservation equations are solved using the Generalized Minimal Residual (GMRES) method, while the mass conservation equation is solved using a Gauss-Seidel (G-S) method. The rest of the equations do not require an iterative method.

Algorithm The implicit algorithm for the conjugate problem requires the solution of the two domains individually until convergence is achieved. After each domain iteration, the two domains exchange information with respect to the temperature distribution on their common interface. Subsequently, the heat flux between them is calculated for every control face. This heat flux distribution is imposed as the boundary condition in the next iteration of each domain. This procedure is repeated until the solution of the two domains converge.

With respect to the solution of each domain, the heat exchanger domain involves the numerical solution of just one variable, whereas for the packed bed, various variables are computed. Therefore, inner sub-iterations are conducted for the numerical solution of the packed bed. The initial inner iterative algorithm had a significant computational cost, that would be problematic for simulations of practical applications. Three major modifications were applied in the initial iterative algorithm in order to improve the computational speed of the model. This improvement is

achieved by reducing the required iterations or by increasing the admissible timestep or by reducing the computational cost of the iteration. Algorithm 1 illustrates the initial iterative process for the packed bed domain, while Algorithm 2 illustrates its improved version, which employs the three modifications discussed subsequently.

Step 1. Coupling the mass transfer related equations
The first step involves the distinction between the heat transfer equations and the mass transfer equations. In Algorithms 1 and 2, heat transfer related equations are marked with red, while mass transfer related equations are marked with blue. It was identified that the mass transfer equations are strongly coupled and in the initial algorithm they required a low timestep in order to not diverge. Even in low timestep, the sub-iterations between them would be part of the entire iteration of the packed bed, thus, involving the computation of the energy equations as well.

For this reason, the mass transfer equations were incorporated inside the Gauss-Seidel iterative method for the mass transfer equations, marked as blue in Algorithm 2. This is hereinafter referred to as the Mass block. This modification improved significantly the computational speed through (i) increasing the admissible timestep by one order (ii) reducing the required iterations and (iii) skipping the energy equations in iterations concerning the convergence of the Mass block.

Step 2. Conjoint solution of energy conservation equations of gas and solid
For the numerical solution of the energy conservation equations, the built-in GMRES solver of TermoFluids is used. After the discretization of these equations in all the control volumes, they become a system of n algebraic equations, where n is the nodes number. The system is expressed in its matrix form, with an $n \times n$ square matrix $\mathbf{A}$ containing the coefficients of the variables T, and a $n \times 1$ column matrix $\mathbf{b}$, containing the remaining terms of each equation. GMRES receives the matrix and the column vector and solves the system for all T. In the initial algorithm, this procedure was being performed twice in each sub-iteration, once for T_g and T_s, respectively (Figure 2.2a). The terms involving the other's phase temperature were considered constant and they were included in $\mathbf{b}$. Thus, after the solution of T_g, its updated value would be used for the calculation of T_s, and vice versa, until convergence. Similarly to the Mass block, the sub-iterations related to the convergence between the two energy equations were part of the entire packed bed iteration, thus the Mass block would also be computed.

For these reasons, it was decided to merge the two energy equations in one larger set of equations, hereinafter referred to as the Thermal block (Figure 2.2b). As illustrated, this larger matrix is composed by four quartiles. The $\mathbf{A}_g$ is placed on the upper left quartile, while $\mathbf{A}_s$ is placed on the bottom right. The terms of the gas energy equation that involve T_s are placed in the upper right quartile, while the terms of the solid equation that involve T_g are placed in the bottom left quartile. In this way, the terms that link the two equations are solved conjointly and thus the required iterations decrease.

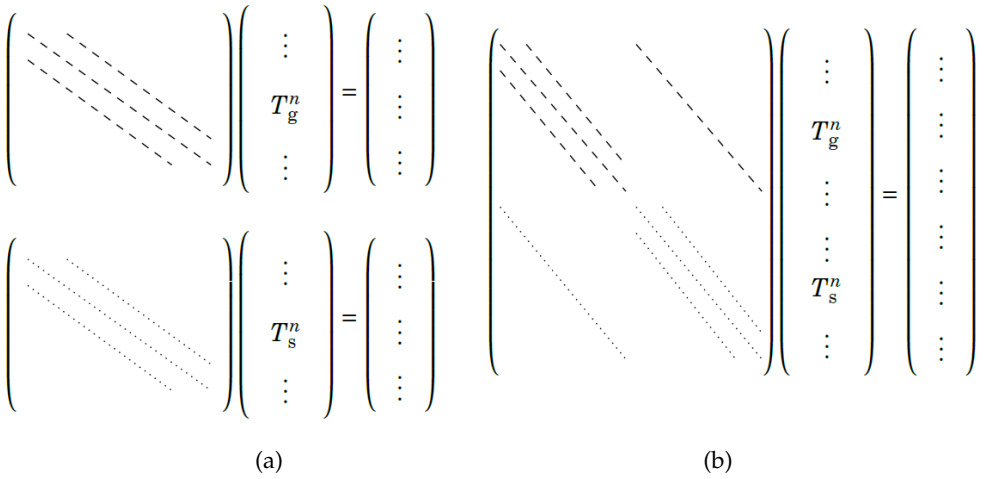

Figure 2.2: Schematic illustration of Step 2, with respect to the treatment of the energy conservation equation in (a) the initial algorithm and (b) the improved algorithm

This action improved the computational speed of the model since (i) the computational cost of each iteration decreased, as constructing and solving one set of matrices instead of two is computationally faster, (ii) the convergence between T_g and T_s requires considerably less iterations.

Step 3. Multi-timestep approach

The third modification arises from the fact that the mass transfer phenomena have lower time scale than the heat transfer phenomena. Consequently, the Mass block requires a significantly lower timestep than the Energy block. In a conventional approach, the smallest timestep is imposed to all the equations. Therefore, such ap-

proach would entail to numerically solve the Energy block – the most computationally intensive part of the model – more often than it is actually required, leading to a significantly higher computational cost.

In order to improve the computational speed of the model, a multi-timestep approach is adopted. With this approach, the Energy block is solved using a certain timestep Δt, while the Mass block is solved at a lower sub-timestep $\Delta t_{\text{sub}} = \Delta t / N_{\Delta t_{\text{sub}}}$.

On the one hand, the Mass block requires the temperatures for (i) the adsorption equilibrium capacity, (ii) the temperature-dependence of the diffusivity and (iii) the pressure calculation. Using the same values of T_{g} and T_{s} for all $N_{\Delta t_{\text{sub}}}$ sub-timesteps within one timestep does not affect the results. Solving the energy equations at the lower timestep results in imperceptible variations in the temperatures. On the other hand, the Energy block requires from the Mass block calculations, the mass fluxes within the domain for the convection term of the gas equation and the adsorption rate for the exothermic source term of the solid equation. These values are integrated for all the $N_{\Delta t_{\text{sub}}}$ and equivalent values are calculated for Δt. As elaborated in Section 2.5.1, this approach does not compromise the accuracy of the solution, while it drastically reduces the computational cost.

After the improvement of the packed bed domain algorithm through the three steps elaborated above, the entire timestep algorithm is shaped as illustrated in Figure 2.3.

Algorithm 1: Initial algorithm

while $\epsilon_{iter} > \theta_{iter,PB}$ **do**
- **for** *all nodes* **do**
  - calculate w^* ;
  - calculate $\frac{\partial w}{\partial t}$;
  - calculate w ;
- **end**
- **while** $\epsilon_{\rho,G\text{-}S} > \theta_{\rho,G\text{-}S}$ **do**
  - **for** *all nodes* **do**
    - calculate ρ_g ;
  - **end**
- **end**
- **for** *all nodes* **do**
  - setup GMRES matrices for T_g ;
- **end**
- GMRES solution for T_g ;
- **for** *all nodes* **do**
  - setup GMRES matrices for T_s ;
- **end**
- GMRES solution for T_s ;
- **for** *all nodes* **do**
  - calculate P ;
- **end**
- Pressure gradient ∇P calculation ;
- **for** *all faces* **do**
  - calculate $\vec{u}$;
  - calculate $\dot{m}_g$;
- **end**

end

Algorithm 2: Improved algorithm

while $\epsilon_{iter} > \theta_{it,PB}$ **do**
- **for** # Δt_{sub} **do**
  - **while** $\epsilon_{\rho,G\text{-}S} > \theta_{\rho,G\text{-}S}$ **do**
    - **for** *all nodes* **do**
      - calculate w^* ;
      - calculate $\left.\frac{\partial w}{\partial t}\right|_{\Delta t_{\text{sub}}}$;
      - calculate w ;
      - calculate ρ_g ;
      - calculate P ;
    - **end**
    - ∇P calculation ;
    - **for** *all faces* **do**
      - calculate $\vec{u}$;
    - **end**
  - **end**
- **end**
- **for** *all faces* **do**
  - calculate $\dot{m}_g|_{\Delta t}$
- **end**
- **for** *all nodes* **do**
  - calculate $\left.\frac{\partial w}{\partial t}\right|_{\Delta t}$;
- **end**
- **for** *all nodes* **do**
  - setup conjoint GMRES matrices for T_g and T_s ;
- **end**
- GMRES solution for T_g and T_s ;

end

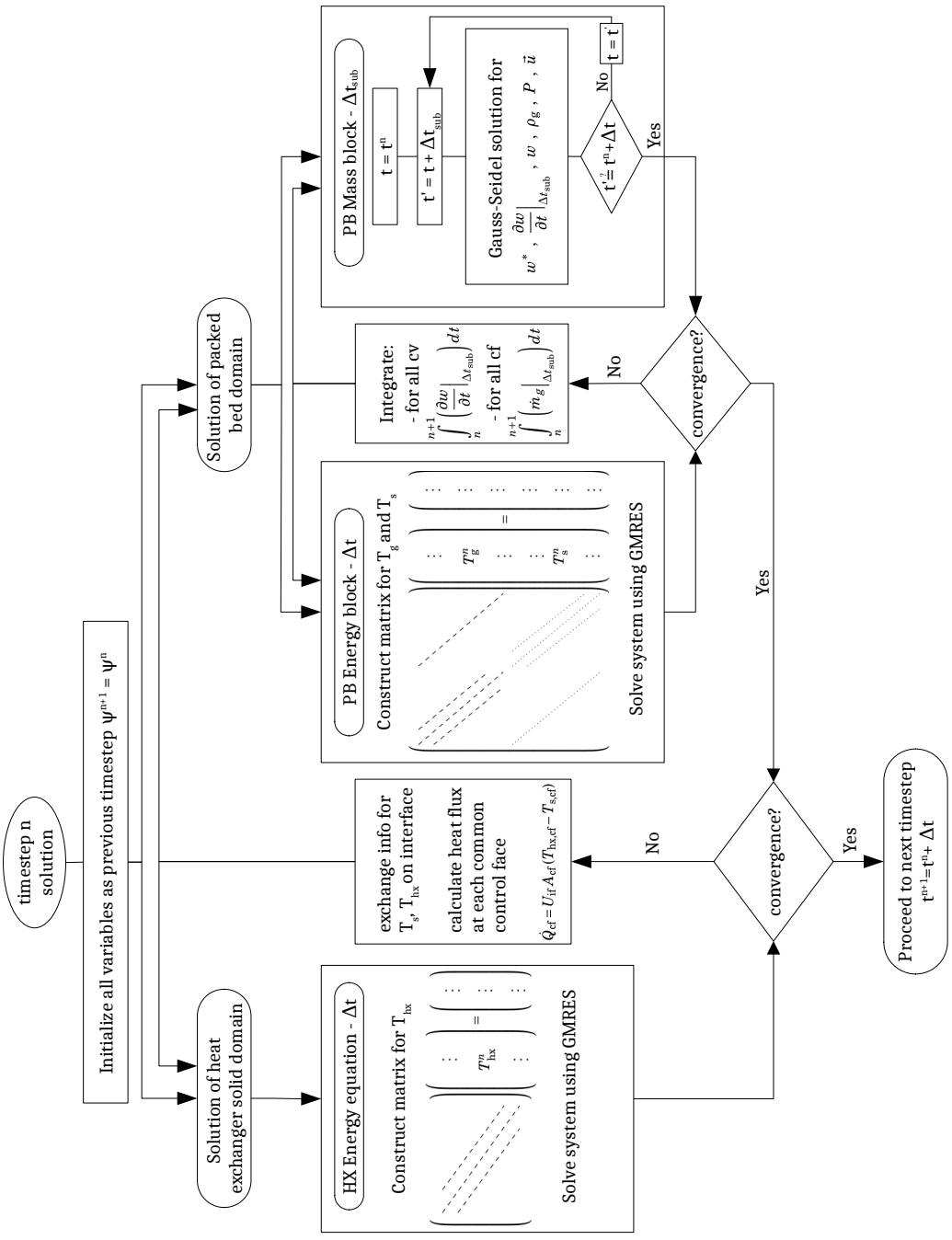

Figure 2.3: Algorithm diagram for the numerical procedure for the solution of one timestep

Parallel computing
The computational model allows the parallelization of the computations on various CPUs. The heat exchanger domain is computationally less intensive than the packed bed domain, therefore the allocation of CPUs was one for the solid and three or seven for the packed bed. The CPU of the heat exchanger domain is also responsible for the calculation of the heat flux between the two domains. It gathers the temperature distribution at the interface from the CPUs of the packed bed, performs the relevant calculations and then returns them the exchanged heat flux.

2.5 Verification and Validation

Upon the construction of the computational model, its credibility was assessed through verification and validation procedures. According to the American Institute of Aeronautics and Astronautics [48] verification and validation are defined as:

"Verification: The process of determining that a model implementation accurately represents the developer's conceptual description of the model and the solution to the model."

"Validation: The process of determining the degree to which a model is an accurate representation of the real world from the perspective of the intended uses of the model."

Subsequently, section 2.5.1 presents the verification assessment, while section 2.5.2 presents the experimental validation.

2.5.1 Verification assessment

2.5.1.1 Introduction and objective

This section presents the verification assessment of the simulation tool. This assessment aims to evaluate the consistency of the model with respect to:

- the global energy conservation
- the global mass conservation
- the mesh independence of the solution
- the timestep independence of the solution

- the sufficiency of the convergence criteria involved
- the correct programming implementation regarding parallelization of computing in various CPUs (Central Processing Unit) and memory leakage

Given the strong interconnection of the spatial and temporal discretization, it has been chosen to present these aspects conjointly. The selected combinations of timestep, mesh and convergence criteria are summarized in Table 2.2.

2.5.1.2 Parameters under consideration

The test cases are monitored and compared from three perspectives. The three perspectives represent different levels of expectations from the model. In computational simulations, a compromise is always sought between the computational cost and the sufficient accuracy of the solution.

Global perspective
Global mass conservation and global energy conservation are evaluated in order to ensure that no mass nor energy is created or destroyed, within the domain and throughout the simulation. Through these metrics, the consistency of the mathematical formulation and its numerical implementation is assessed.

Local perspective
The temporal evolution of the variables values is monitored at a specific point inside the packed bed domain. This aims to question the ability of the model to capture adequately local phenomena. This is mainly used to evaluate the density of the mesh. A coarse mesh may satisfy the aforementioned global balances, although it might fail to capture the local phenomena. It is examined whether the computational cost reduction achieved by using a coarse mesh jeopardize the reliability of the results. This test challenges the distributed-parameter character of the model.

Utilitarian perspective
The monitored parameters are the temporal evolution of the total inflow of vapor mass in the packed bed and the total heat flux between the heat transfer fluid and the heat exchanger solid. These two parameters are sufficient for the calculation of the SCP and

the COP, and thus, the characterization of the reactor performance. This perspective is similar to the global perspective in the sense that it approaches macroscopically the reactor. However, the utilitarian perspective intents to detect whether a case with poor performance in terms of global balances and local perspective – which are considered more strict – can still predict the reactor performance, with sufficient accuracy for the utilization of the model.

2.5.1.3 Computation of the verification assessment metrics

This section details the computation of the verification assessment metrics.

Global perspective - Mass conservation
The mass balance is performed for the adsorbate, since it is the only fluid inside the simulated domain. It simply states that, the contained mass within the domain at any given time should be equal to the sum of the initially contained mass, plus the mass fluxes that crossed the domain boundaries during the period under consideration. The equality that should be evaluated is represented in equation 2.28.

$$M_{\mathrm{a}}(t) \stackrel{?}{=} M_{\mathrm{a,init}} + \int_{t} \dot{M}_{\mathrm{a,inlet}}\, dt \tag{2.28}$$

With respect to the contained mass, the two components of the packed bed are involved, the vapor phase and the adsorbed mass in the solid phase. For its calculation, all the control volumes of the packed bed volume V_{PB} are considered. For the mass fluxes at the boundaries of the domain, all the control faces at the boundary under consideration are summed for every timestep.

$$\left[\sum_{\mathrm{cv}}^{V_{\mathrm{PB}}} \rho_{\mathrm{g,cv}}\, \varepsilon_{\mathrm{b}} V_{\mathrm{cv}} + \sum_{\mathrm{cv}}^{V_{\mathrm{PB}}} \rho_{\mathrm{s}}\, (1-\varepsilon_{\mathrm{t}})\, w_{\mathrm{cv}} V_{\mathrm{cv}}\right]_{t=n} \stackrel{?}{=} \left[\sum_{\mathrm{cv}}^{V_{\mathrm{PB}}} \rho_{\mathrm{g,cv}}\, \varepsilon_{\mathrm{b}} V_{\mathrm{cv}} + \sum_{\mathrm{cv}}^{V_{\mathrm{PB}}} \rho_{\mathrm{s}}\, (1-\varepsilon_{\mathrm{t}})\, w_{\mathrm{cv}} V_{\mathrm{cv}}\right]_{t=0} + \sum_{\Delta t}^{t=n} \left(- \sum_{\mathrm{cf}}^{A_{\mathrm{in}}} \rho_{\mathrm{g,cf}}\, (\vec{u}_{\mathrm{cf}} \cdot \hat{n}_{\mathrm{cf}}) A_{\mathrm{cf}} \right) \Delta t \tag{2.29}$$

where:
$\sum_{cv}^{V_{PB}} \rho_{g,cv}\, \varepsilon_b V_{cv}$ is the vapor mass in the gas phase over the entire packed bed volume,
$\sum_{cv}^{V_{PB}} \rho_s\, (1-\varepsilon_t)\, w_{cv} V_{cv}$ is the adsorbed mass onto the solid phase over the entire V_{PB},
$\sum_{cf}^{A_{in}} \rho_{g,cf}\, (\vec{u}_{cf} \cdot \hat{n}_{cf}) A_{cf}$ is the vapor mass flow rate on the inlet boundary, which is positive for outflow and negative for inflow, since the surface unit vector $\hat{n}_{cf}$ is outward by convention,
$\sum_{\Delta t}^{t=n} \left(-\sum_{cf}^{A_{in}} \rho_{g,cf}\, (\vec{u}_{cf} \cdot \hat{n}_{cf}) A_{cf} \right) \Delta t$ is the total vapor mass that entered the packed bed domain through the inlet boundary, throughout the simulation period under consideration.

Expectedly, the equality of the equations 2.28 and 2.29 will not be valid, due to the errors introduced by the numerical procedure. In order to assess the error, the LHS of these equations is denoted as the calculated mass M_{calc} and the RHS is denoted as the expected mass M_{expe}. The error related to the mass conservation ϵ_{mass} is calculated in equation 2.30, as a relative error.

$$\epsilon_{mass} = \frac{|M_{expe} - M_{calc}|}{M_{expe}} \tag{2.30}$$

Global perspective - Energy conservation
The energy balance is performed for the entire domain, both the packed bed and the heat exchanger solid. The components containing thermal energy are the adsorbate in both gas and adsorbed phase, the solid adsorbent and the solid of the heat exchanger.

In order to be able to perform an energy balance, a slightly different case than the actual adsorption case is considered. An energy balance of the adsorption case would require to know the enthalpy of the adsorbed state, in order to take into account the variation of the contained thermal energy in the solid phase, as a result of the variation of the adsorbed mass (term 2.33-iii). As illustrated in section 2.3.1.4, it is possible to solve the energy equations without knowledge of the enthalpy of the adsorbed state. However, the energy balance would require knowledge of the latter, which is difficult to compute. Moreover, even if the adsorbed state enthalpy was possible

to compute, a good agreement between the expected and the calculated thermal energy would not be achieved. This inconsistency would be related to the value of the adsorption enthalpy. In reality, the adsorption enthalpy depends on the temperature, the pressure and the adsorbed mass. However, the experimentally derived value for adsorption enthalpy that is adopted in this study is constant throughout the temperature, pressure and adsorbed mass range under consideration [40].

Within this context, it was decided to perform the energy balance on a fictitious case, very similar to the adsorption case. The differentiation is that the vapor that is adsorbed onto the solid phase is considered to be condensed instead of adsorbed. The knowledge of the enthalpy of the saturated liquid, as well as the pressure dependence of the condensation enthalpy, allow to perform the energy balance. More particularly, the adsorption of vapor is not associated to the exothermic release of (2.693 ± 0.1)MJ/kg [40], but to the sum of the condensation enthalpy (approximately 2.430-2.477 MJ/kg in the pressure range under consideration) plus the sensible heat according to the temperature of the superheated vapor. In this sense, the fictitious case used for the energy balance approximates very well the actual adsorption case, while it allows to perform the energy balance.

Similarly to the mass balance, the energy balance questions whether the thermal energy contained at a given instant is equal to the initially contained thermal energy, plus the energy fluxes that crossed the domain boundaries during the period under consideration.

$$E(t) \stackrel{?}{=} E_{\text{init}} + \int_t \dot{E}_{\text{inlet}}\, dt \tag{2.31}$$

As it will be explained later (terms 2.33-ii and 2.33-iv), the energy balance is feasible only if equation 2.31 is reordered as in 2.32. Therefore, it is questioned whether the change in the thermal energy contained inside the domain is equal to the energy fluxes.

$$\Delta E = E(t) - E_{\text{init}} \stackrel{?}{=} \int_t \dot{E}_{\text{fluxes}}\, dt \tag{2.32}$$

The variation of the thermal energy contained in the domain is the sum of the four components: (i) the gas phase, (ii) the dry solid adsorbent, (iii) the adsorbed adsorbate and (iv) the solid of the heat exchanger. The thermal energy fluxes at the boundaries

of the domain pertain to the thermal energy associated to the inlet vapor mass and to the heat exchanged between the heat exchanger solid and the heat transfer fluid.

$$\underbrace{\Delta E_{\text{gas}}}_{\text{i}} + \underbrace{\Delta E_{\text{dry adsorbent}}}_{\text{ii}} + \underbrace{\Delta E_{\text{adsorbed}}}_{\text{iii}} + \underbrace{\Delta E_{\text{solid,hx}}}_{\text{iv}} \stackrel{?}{=} \underbrace{\int_t \dot{E}_{\text{g,inlet}}\, dt}_{\text{v}} + \underbrace{\int_t \dot{E}_{\text{conv,HTF}}\, dt}_{\text{vi}} \tag{2.33}$$

where:

(i) $\Delta E_{\text{gas}} = \sum_{\text{cv}}^{V_{\text{PB}}} \left(\rho_{\text{g}}^{\text{t}} h_{\text{g}}^{\text{t}} - \rho_{\text{g}}^{0} h_{\text{g}}^{0}\right)_{\text{cv}} \varepsilon_{\text{b}} V_{\text{cv}}$ is the enthalpy change of the gas phase as a result of the density variation and the specific enthalpy variation. The latter is a consequence of the pressure and temperature change. The sum involves all the control volumes of the packed bed domain.

(ii) $\Delta E_{\text{dry adsorbent}} = \sum_{\text{cv}}^{V_{\text{PB}}} \rho_{\text{s}} \left(h_{\text{s}}^{\text{t}} - h_{\text{s}}^{0}\right)_{\text{cv}} (1-\varepsilon_{\text{t}}) V_{\text{cv}} = \sum_{\text{cv}}^{V_{\text{PB}}} \rho_{\text{s}} c_{p_{\text{da}}} \left(T_{\text{s}}^{\text{t}} - T_{\text{s}}^{0}\right)_{\text{cv}} (1-\varepsilon_{\text{t}}) V_{\text{cv}}$
This term amounts for the variation of the thermal energy inside the dry solid adsorbent. This is one of the term that obliges the energy balance to be based on equation 2.32 rather on equation 2.31. Although the enthalpy of the solid adsorbent is unknown, the enthalpy change can be calculated as $c_{\text{p}}\Delta T$. The sum involves all the control volumes of the packed bed domain.

(iii) $\Delta E_{\text{adsorbed}} = \sum_{\text{cv}}^{V_{\text{PB}}} \rho_{\text{s}} \left(w^{\text{t}} h_{\text{ap}}^{\text{t}} - w^{0} h_{\text{ap}}^{0}\right)_{\text{cv}} (1-\varepsilon_{\text{t}}) V_{\text{cv}}$ is the term that takes into account the enthalpy variation of the adsorbed phase, as a result of both the temperature change of the solid phase Δh_{ap} and the variation of the adsorbed mass amount Δw. This is the term that obliged the energy balance to be based on condensation instead of adsorption as explained earlier. The sum involves all the control volumes of the packed bed domain.

(iv) $\Delta E_{\text{solid,hx}} = \sum_{\text{cv}}^{V_{\text{HX}}} \rho_{\text{hx}} \left(h_{\text{hx}}^{\text{t}} - h_{\text{hx}}^{0}\right)_{\text{cv}} V_{\text{cv}} = \sum_{\text{cv}}^{V_{\text{HX}}} \rho_{\text{hx}} c_{p_{\text{hx}}} \left(T_{\text{hx}}^{\text{t}} - T_{\text{hx}}^{0}\right)_{\text{cv}} V_{\text{cv}}$
This term corresponds to the thermal energy variation within the heat exchanger solid V_{HX}, during the period under consideration. The same applies as for the term (2.33-ii), regarding the necessity to perform the energy balance as in equation 2.32. The sum involves all the control volumes of the heat exchanger domain.

$$\text{(v)} \int_t \dot{E}_{\text{g,inlet}}\, dt = \sum_{\Delta t}^{t=n} \left[-\sum_{\text{cf}}^{A_{\text{in}}} \underbrace{\left(\rho_{\text{g,cf}} \left(\vec{u}_{\text{cf}} \cdot \hat{n}_{\text{cf}}\right) A_{\text{cf}}\right)}_{\dot{m}_{\text{g}}} h_{\text{g}} \right] \Delta t$$

This term takes into account the thermal energy flux at the boundaries of the reactor domain, which is associated to the thermal energy contained by the total inlet vapor mass. The sum involves all the control faces at the boundary of the packed bed where vapor flux takes place, for all timesteps. It is reminded that $\dot{m}_{\text{g}}$ is positive for outflow and negative for inflow, since the surface unit vector is outward.

$$\text{(vi)} \int_t \dot{E}_{\text{conv,HTF}}\, dt = \sum_{\Delta t}^{t=n} \left[\sum_{\text{cf}}^{A_{\text{HTF}}} U_{\text{HTF}} A_{\text{cf}} \left(T_{\text{HTF}} - T_{\text{hx,cf}}\right) \right] \Delta t$$

This term corresponds to the total thermal energy exchanged between the heat exchanger solid and the heat transfer fluid. The sum involves all the control faces at the common boundary of the heat exchanger with the HTF, for all timesteps.

Expectedly, the equality of the equations 2.32 and 2.33 will not be valid, due to the errors introduced by the numerical procedure. In order to assess the error, the LHS of these equations is denoted as the calculated thermal energy variation ΔE_{calc} and the RHS is denoted as the expected thermal energy variation ΔE_{expe}. The error related to the energy conservation ϵ_{energy} is calculated in equation 2.34, as a relative error.

$$\epsilon_{\text{energy}} = \frac{|\Delta E_{\text{expe}} - \Delta E_{\text{calc}}|}{\Delta E_{\text{expe}}} \tag{2.34}$$

Local perspective - Variable evaluation on a specific point

Since the variable values are calculated at the centroids of the control volumes, the value of a variable on a specific point requires to be computed. This is achieved through a built-in function of the TermoFluids code, which employs the least-squares method for the calculation of the variable gradient at the neighboring nodes. Subsequently, the variable value at the point under consideration is calculated based on the variable value and gradient on the neighboring nodes, while applying a distance-weighting factor between those values [49,50].

Utilitarian perspective - Vapor inflow and heat exchanged with HTF
The verification metrics pertaining in the utilitarian perspective were presented earlier in the context of the global perspective.

The inlet vapor inside the packed bed is calculated as:

$$m_{\mathrm{g,total}} = \sum_{\Delta t}^{t=n} \left(- \sum_{\mathrm{cf}}^{A_{\mathrm{in}}} \dot{m}_{\mathrm{g,cf}} \right) \Delta t = \sum_{\Delta t}^{t=n} \left(- \sum_{\mathrm{cf}}^{A_{\mathrm{in}}} \rho_{\mathrm{g,cf}} \left(\vec{u}_{\mathrm{cf}} \cdot \hat{n}_{\mathrm{cf}} \right) A_{\mathrm{cf}} \right) \Delta t$$

The heat exchanged between the heat exchanger solid and the heat transfer fluid is calculated as:

$$Q_{\mathrm{HTF,total}} = \sum_{\Delta t}^{t=n} \left(\sum_{\mathrm{cf}}^{A_{\mathrm{in}}} \dot{q}_{\mathrm{cf}} A_{\mathrm{cf}} \right) \Delta t = \sum_{\Delta t}^{t=n} \left[\sum_{\mathrm{cf}}^{A_{\mathrm{HTF}}} U_{\mathrm{HTF}} A_{\mathrm{cf}} \left(T_{\mathrm{HTF}} - T_{\mathrm{hx,cf}} \right) \right] \Delta t$$

2.5.1.4 Test case details

The geometry of the test case pertains to the simulation of the hexagonal honeycomb packed bed reactor. The exact dimensions correspond to the base scenario, as presented in Section 3.4. The test case is similar to an adsorption phase, although some differentiations are considered in order to add complexity to the test. The initial conditions are 30 °C for temperature and 1228 Pa for pressure. The adsorbed mass is the equilibrium capacity for the aforementioned conditions. Once the simulation begins, the inlet conditions for the reactor are $P_{\mathrm{inlet}} = 4243\,\mathrm{Pa}$ and $T_{\mathrm{g,inlet}} = 80\,^{\circ}\mathrm{C}$. The temperature of the heat transfer fluid is considered 30 °C and the convection heat transfer coefficient is $U_{\mathrm{HTF}} = 1000\,\mathrm{W/(m^2\,K)}$. The period of the simulation case is 100 s.

2.5.1.5 Results

Eleven cases were chosen for the presentation of the results of the verification assessment. These cases are summarized in Table 2.2, along with their respective errors regarding mass and energy balances.

With respect to the contents of Table 2.2, the first block *Temporal discretization* presents the timestep and the number of sub-timesteps adopted in each test case. The second block *Spatial discretization* presents the number of control volumes in the packed bed domain mesh and the heat exchanger domain mesh. The third block *Convergence*

criteria presents the convergence criteria adopted in the iterative numerical procedures, where G-S refers to the Gauss-Seidel method used for the Mass block of the packed bed and the GMRES refers to the solver used for the Energy block of the packed bed (T_g,T_s) and for T_{hx} in the heat exchanger. The last column *Global perspective results* summarizes the errors of the global balances for mass and energy, as calculated in equations 2.30 and 2.34, respectively.

Increasing test number implies (i) on the one hand, a "less strict solution" - by having either coarser mesh, or higher timestep or higher convergence criteria, and (ii) on the other hand, a lower computational cost. The following comparisons can be performed:

- Test 0 and Test 1 compare two cases without the multi-timestep approach, with two different mesh densities. This provides a mesh independence test prior to the application of the multi-timestep approach.
- Test 1-4 compare 4 different temporal discretization combination that use the same mesh. This aims to question the validity of the multi-timestep approach. The timestep is progressively increased and in parallel, the number of sub-timesteps.
- Test 4-7 compare various mesh densities with the same temporal discretization scheme, based on the multi-timestep approach.
- Test 7-10 compare cases with the same mesh and the same temporal discretization, but with different convergence criteria for the iterative numerical procedures. In comparison to Test 7, Test 8 has lower Gauss-Seidel convergence criterion, Test 9 has lower GMRES convergence criterion, whereas Test 10 has lower values for both convergence criteria.

With respect to the local perspective, the variables are evaluated at a specific point inside the packed bed domain. As seen in Figure 3.14, after applying symmetries and periodicities, the packed bed domain is a triangular prism. The point at which the variable values are evaluated is the centroid of this triangular prism. Figure 2.4 illustrates the temporal evolution at the centroid for the gas temperature, the gas density, the pressure and the adsorbed mass.

With respect to the utilitarian perspective, the temporal evolution of the total inlet gas and the total heat exchanged with the HTF are presented in Figure 2.5, normalized by the adsorbent mass.

Table 2.2: Test cases details and global perspective results

	Temporal discretization		Spatial discretization		Convergence criteria		Global perspective results	
	Δt	$N_{\Delta t_{\text{sub}}}$	PB	HX	G-S	GMRES	ϵ_{mass}	ϵ_{energy}
Test 0	10^{-6}	-	1977	988	10^{-12}	10^{-15}	2.28×10^{-10}	1.24×10^{-08}
Test 1	10^{-6}	-	1275	685	10^{-12}	10^{-15}	3.19×10^{-10}	1.97×10^{-08}
Test 2	10^{-5}	10	1275	685	10^{-12}	10^{-15}	3.57×10^{-10}	1.88×10^{-09}
Test 3	10^{-4}	100	1275	685	10^{-12}	10^{-15}	1.93×10^{-10}	8.75×10^{-11}
Test 4	10^{-3}	1000	1275	685	10^{-12}	10^{-15}	1.02×10^{-09}	7.96×10^{-11}
Test 5	10^{-3}	1000	631	448	10^{-12}	10^{-15}	1.01×10^{-09}	1.73×10^{-12}
Test 6	10^{-3}	1000	357	300	10^{-12}	10^{-15}	1.04×10^{-09}	7.54×10^{-11}
Test 7	10^{-3}	1000	199	187	10^{-12}	10^{-15}	9.69×10^{-10}	6.62×10^{-11}
Test 8	10^{-3}	1000	199	187	10^{-12}	10^{-10}	9.69×10^{-10}	6.65×10^{-06}
Test 9	10^{-3}	1000	199	187	10^{-10}	10^{-15}	4.36×10^{-09}	6.07×10^{-11}
Test 10	10^{-3}	1000	199	187	10^{-10}	10^{-10}	4.36×10^{-09}	6.65×10^{-06}

Results discussion

For the global perspective results, it can be observed that all presented cases exhibit acceptable errors for the global balances for mass and energy. The highest ϵ_{energy} is 6.65×10^{-6} and it is exhibited in Tests 8 and 10 where the convergence criterion of the GMRES solver is increased. In order to put this error into context, the corresponding absolute error in Joules would provoke a temperature difference of less than 10^{-4}°C if it is uniformly distributed across the domain. A counter-intuitive phenomenon is observed between Tests 1-4, where at increasing timestep the ϵ_{energy} decreases. This is explained since the basic difference of the Tests 1-4 is the frequency that the energy equations are solved. Namely, within a given period of 10^{-3}s, the energy equations are solved 1000 times for Test 1, while for Test 4 they are solved only 1 time. Therefore, the error that is introduced by the iterative solver is lower for Test 4. Regarding ϵ_{mass} the highest value is 4.36×10^{-9} and it is encountered in Tests 9 and 10, where the Gauss-Seidel convergence criterion is increased. In order to put this error into context, its corresponding absolute error would provoke a difference in the adsorbed mass in the order of $10^{-9}\text{kg}_\text{w}/\text{kg}_\text{s}$, if it is uniformly distributed.

With respect to the local perspective, the temporal evolution of the variables at the centroid are almost identical. In the case of the adsorbed mass in Figure 2.4d, the "less strict solutions" appear to diverge slightly. It should be noted that the results

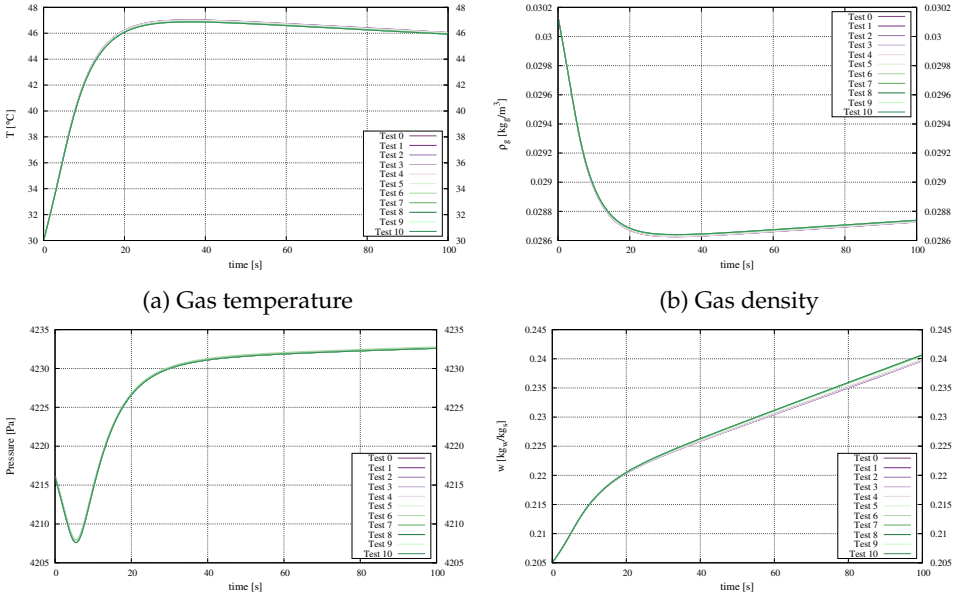

(a) Gas temperature

(b) Gas density

(c) Pressure

(d) Adsorbed mass

Figure 2.4: Temporal profiles at the centroid of the packed bed domain for (a) gas temperature (b) gas density (c) pressure and (d) adsorbed mass

of these graphs – apart from the solution quality – include also the error from the interpolation of the variable to the specific point under consideration.

Finally, the metrics regarding the utilitarian perspective (Figure 2.5) show that all test cases have good agreement with respect to the total inlet mass and total heat exchanged. Thus, all test cases would provide the same results with respect to the reactor performance.

Programming implementation assessment

Additionally to the above, the programming implementation was assessed with respect to:

- **Parallelization in various CPUs**: This test aims to assure that the parallelization of the computations to various CPUs does not affect the solution. In other words, it questions whether the required data are communicated correctly between

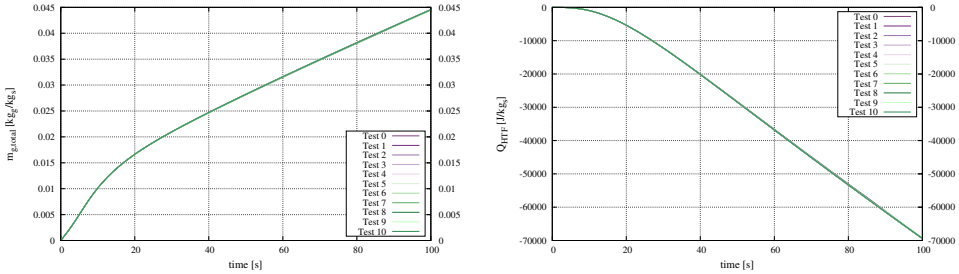

(a) Total inlet gas (b) Total heat exchanged with the HTF

Figure 2.5: Temporal profiles of (a) the total inlet gas to the packed bed domain and (b) the total heat exchanged with the HTF

the CPUs. In this context, the same case was simulated by partitioning the packed bed domain to 1, 3 and 7 CPUs, obtaining the same results and therefore, assuring that the parallelization is error-free.

- **Memory leak**: This test aims to detect memory leakage problems. These problems are encountered when unnecessary information is not deleted by the program and therefore the allocated memory is not released. Consequently, these data accumulate and they increasingly occupy the memory of the system and decelerate the computational speed of the code. In this context, the computational time spent on each iteration was monitored and it was verified that its remain constant throughout the simulation.

2.5.2 Experimental validation

2.5.2.1 Introduction and scope

In addition to the verification procedure presented in the previous section, a priority of this study was to experimentally validate the numerical model using experimental results published in the literature. This section aims to present the experimental validation task.

The experimental validation involves the numerical simulation of a conducted experiment. An experiment is conducted, monitored and documented with the objective to

reproduce it numerically. During the experiment, one or more physical quantities are measured and then they are compared with their numerical counterparts, which arise from the simulation. This comparison reveals the ability of the model to simulate the physical phenomena involved accurately.

With respect to which quantities are compared between the experiment and the simulation, researchers employed different approaches. For the experimental validation of distributed-parameter models of adsorption packed bed reactors, the following approaches are encountered in the literature.

A. temporal profile of the outlet temperature of the heat transfer fluid [10,19,29,51]

B. temporal profile of the temperature at the exterior wall of the packed bed [23,52]

C. temporal profile of the average temperature of the packed bed (averaged spatially) [20,53,54]

D. temporal profile of the total adsorbed mass inside the packed bed [27]

E. temporal profile of the temperature in different points inside the packed bed (usually 3-4 points) [4,6,9,51]

From the approaches listed above, the only one that challenges the distributed-parameter of the model is the approach E, where the temperature is measured inside the packed bed in various positions. The other approaches treat the adsorption reactor macroscopically. They might be sufficient for validating the behavior of the reactor at a component level, however, the numerical solution inside the packed bed is not questioned. Consequently, it was considered that an experimental validation based on information inside the packed (instead of information outside the packed bed) would provide a more rigorous experimental validation. Therefore, one criterion for the selection of the experiment was to be based on approach E.

During this thesis, the initiative emerged with respect to the conduction of an experiment in the CTTC laboratory, that will combine approaches A, D and E. This is further elaborated in section 2.5.2.3. In the frame of this thesis, the necessity of this experiment was identified, the experiment was conceptually conceived and some preparatory tasks were performed. However, its complete preparation and implementation form part of the future studies in CTTC.

2.5.2.2 Numerical and experimental results comparison

The experiment selected for the validation of the numerical model was conducted by Jribi et al. [7]. This study was chosen since it is the most well documented experiment among the studies that belong to approach E. The experiment pertains to a tubular reactor with radial fins. The employed adsorption pair is ethanol and activated carbon (Maxsorb III). Throughout the adsorption process, the temperature is monitored at four points inside the packed bed, using thermocouples with an accuracy of ± 0.1 K. The four thermocouples are positioned at a distance of 0, 1, 5 and 10 mm from the tube of the reactor, and they are abbreviated accordingly, as T0, T1, T5 and T10. Figure 2.6 illustrates the reactor geometry, the position of the thermocouples and the computational domain.

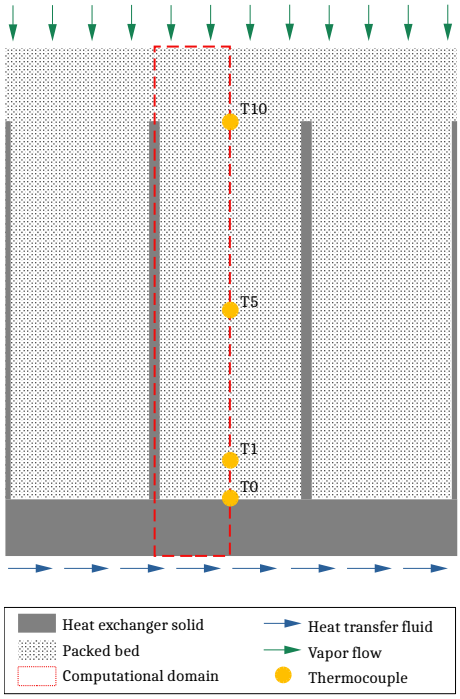

Figure 2.6: Schematic diagram of the geometry, calculation domain and position of thermocouples of the experiment used for validation (Reproduced image from [7])

The simulation details can be found in [7]. Along with the temporal temperature profiles measured by the four thermocouples, the boundary conditions throughout the experiment are also provided [7]. These are the temporal profiles of the heat transfer fluid temperature, the inlet vapor refrigerant temperature and the vapor pressure at the inlet of the reactor. The intention is to predict the temperature profile at the four points inside the packed bed by simulating the reactor during the adsorption process. The experimental and the simulated results are shown in Figure 2.7.

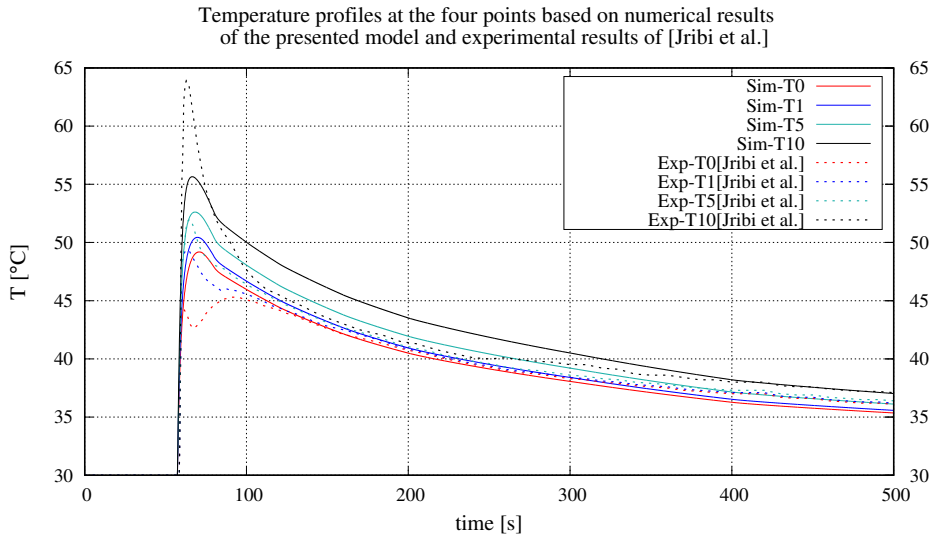

Figure 2.7: Comparison of the numerical results of the presented model and experimental results from Jribi et al. [7]

The numerical model predicts qualitatively well the temperature evolution at T1 and T5. At T10, a significant temperature peak is not captured by the model. Further analysis was conducted in order to identify the model input parameters that might be responsible for this discrepancy. It was revealed that this peak is highly sensitive to the reactor inlet pressure profile. At the beginning of the experiment, the reactor and the evaporator are disconnected and their respective pressures are 950 Pa and 8700 Pa. When the two vessels are connected, a sudden pressure peak is exhibited at the reactor inlet pressure profile [7]. This pressure peak is associated to the temperature peak observed for T10 in Figure 2.7. There are two uncertainties with respect to the

appropriateness of the inlet pressure profile that is used as input to the computational model:

- The relative position of the reactor pressure sensor is unknown, with respect to the incorporated thermocouples. It is possible that the pressure measured by this instrument does not correspond to the actual pressure of the inlet vapor at the position of the thermocouples. Therefore, it is unclear whether this profile represents adequately the inlet pressure profile of the simulated domain.
- The sampling of the sensor is unknown, therefore it is possible that the inlet pressure peak is not captured well quantitatively. In that case, the inlet pressure profile imposed as boundary condition during the simulation does not reproduce the real experimental conditions, leading to a discrepancy between the numerical and experimental results.

Taking into consideration the important influence of the inlet pressure profile, as well as the two aforementioned uncertainties, it is conjectured that this discrepancy might be attributed partially to an inconsistency between the experimental and the numerical boundary conditions.

With respect to the numerical results of T0, the overall behavior is well captured throughout the simulation, except in the period between 60 s to 110 s. In [7], it is stated that the thermocouple T0 is positioned at a distance of 0 mm from the tube. It is unclear whether the solid tube and the thermocouple are in contact. The presented numerical results correspond to the vapor temperature.

In addition to these case-specific reasons that might be responsible for the discrepancies between the numerical and experimental results, there are various other reasons that apply to any experimental validation. These include errors related to the conduction and documentation of the experiment, as well as inadequacies of the modeling approaches involved. Despite the inconsistencies discussed above, the agreement between the numerical and experimental results is considered reasonable for further utilization of the model.

Discussion regarding the contact heat transfer coefficient

It should be noted that for the simulation of the experiment, the value of the contact heat transfer coefficient at the interface between the packed bed and the heat exchanger solid, U_{if}, is unknown. It must be emphasized that for the silica gel case –

the adsorbent used in the simulations in this thesis – this value was experimentally derived by Glaznev and Aristov [47]. However, since this parameter is unavailable for the experimental case, a sensitivity analysis was conducted. For the silica gel, the contact heat transfer coefficient was taken as $U_{\text{if}} = 100\,\text{W}/(\text{m}^2\,\text{K})$ for particle diameter $d_{\text{p}} = 0.5\,\text{mm}$. The contact heat transfer coefficient increases when the particle diameter decreases [47]. The particle diameter of the activated carbon in this experiment is $d_{\text{p}} = 0.07\,\text{mm}$ [7], therefore a U_{if} higher than $100\,\text{W}/(\text{m}^2\,\text{K})$ is expected. The simulation was conducted for U_{if} values of 140, 160, 180, 200 and $220\,\text{W}/(\text{m}^2\,\text{K})$.

In order to quantify the discrepancy, the root mean square deviation (RMSD) between the experimental and the numerical results is calculated as in equation 2.35. The sampling is taken every 0.1 s and two time periods are considered: (a) the total duration t_{total} excluding the first 56 s when the reactor is still disconnected from the evaporator and it is at equilibrium with the boundary conditions, and (b) the most transient period of the experiment, t_{trans}, between 56 s and 100 s.

$$\text{RMSD} = \sqrt{\frac{\sum_{t=1}^{N} (T_{\text{t,exp}} - T_{\text{t,sim}})^2}{N}} \tag{2.35}$$

The RMSD results are presented in Table 2.3 for t_{trans} and t_{total}. The maximum and average RMSD of the four thermocouples are reported for each case.

Furthermore, Figure 2.8 illustrates the span of the temperature profile in each thermocouple position, as it is influenced by the contact heat transfer coefficient. For the sake of clarity of the graphs, only the cases of 140 and $220\,\text{W}/(\text{m}^2\,\text{K})$ are plotted. The results corresponding to the other cases lie within the in-between shaded region.

Table 2.3: Root mean square deviation (RMSD) during t_{trans} and t_{total}, for U_{if} values in the range of 140-220 $W/(m^2K)$

	140 $W/(m^2 K)$		160 $W/(m^2 K)$		180 $W/(m^2 K)$		200 $W/(m^2 K)$		220 $W/(m^2 K)$	
	t_{trans}	t_{total}	t_{trans}	t_{total}	t_{trans}	t_{total}	t_{trans}	t_{total}	t_{trans}	t_{total}
T0	4.29	1.40	3.93	1.29	3.65	1.24	3.42	1.23	3.24	1.23
T1	2.78	1.03	2.53	0.90	2.36	0.85	2.24	0.85	2.16	0.88
T5	2.81	1.42	2.55	1.19	2.34	1.03	2.19	0.92	2.08	0.85
T10	3.67	2.25	3.76	2.05	3.85	1.91	3.95	1.81	4.05	1.75
Max.	4.29	2.25	3.93	2.05	3.85	1.91	3.95	1.81	4.05	1.75
Aver.	3.39	1.53	3.19	1.36	3.05	1.26	2.95	1.20	2.88	1.18

As observed in Table 2.3, the average RMSD of the four thermocouples for the entire duration t_{total} decreases at the higher value of the U_{if} range under consideration. However, the maximum RMSD for the transient region of the experiment t_{trans} also corresponds to the higher U_{if}.

As illustrated in Figure 2.8, the effect of U_{if} is the vertical displacement of the temperature profiles. At higher U_{if}, the thermal energy released as a result of the exothermic adsorption is removed more effectively and the temperature is generally lower. The maximum temperature difference between $U_{if} = 140\,W/(m^2\,K)$ and $U_{if} = 220\,W/(m^2\,K)$ is 2.25 °C and it is encountered in T0. This maximum temperature difference decreases while the position of the thermocouple from the tube increases. In particular, the maximum temperature difference between $U_{if} = 140\,W/(m^2\,K)$ and $U_{if} = 220\,W/(m^2\,K)$ is 2.04, 1.81 and 1.32 °C for T1, T5 and T10, respectively.

The results presented in Figure 2.7 pertain to the case of $U_{if} = 180\,W/(m^2\,K)$, as an intermediate case, compensating the average RMSD for t_{total} and maximum RMSD for t_{trans}.

2.5.2.3 Future experimental validation

As already commented, during the experimental validation process, the necessity of performing an experimental test in the CTTC laboratory was identified. This section elaborates the motivation for conducting this experiment.

In order to convey the academic benefit of this experiment, it is useful to recall the five approaches encountered hitherto in the literature. With the exception of approach D,

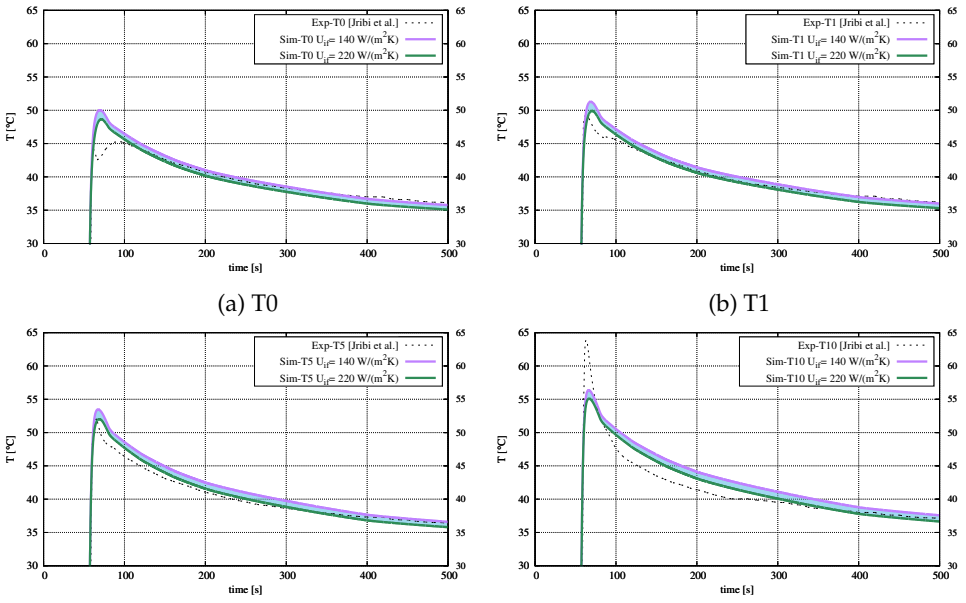

(a) T0 (b) T1

(c) T5 (d) T10

Figure 2.8: Influence of the contact heat transfer coefficient on the temporal profile of temperature at the four positions under consideration

all the rest approaches use the temperature as the basis of the experimental validation, since it is the physical quantity which can be measured more readily. Approach D exhibits an interesting feature, since the measured quantity is the total adsorbed mass. The latter is directly related to the useful outcome of this system, the cooling production. Even though this approach does not challenge the distributed-parameter character of the model and it does not provide information inside the packed bed, it can be utilized for the validation of the numerical prediction regarding an important indicator for the performance of the reactor. Approach A – monitoring the HTF outlet temperature – provides experimental information on the thermal energy exchanged between the HTF (assuming knowledge of the HTF inlet temperature). Therefore, approach A allows to validate the thermal energy required for the desorption of the reactor, which is the energy input of the system.

According to the above, it is evident that an experiment combining the approaches A, D and E would be highly beneficial for the community. Approach D questions the

ability of the model to predict the overall adsorbed mass in the reactor and thus, the cooling produced. Approach A allows the validation of the thermal energy exchanged with the HTF. Finally, approach E questions the ability of the model to predict the local physical phenomena inside the reactor. The three approaches complement each other and their combination would enhance the rigorosity of the experimental validation.

Additionally to the fact that this experiment would be a state-of-the-art experiment with respect to the validation of the adsorption packed bed reactors, there are other practical aspects that led to the decision for conducting such experiment in CTTC. In summary, the reasons that led to this decision are:

- Conducting the experiment in our group will provide a more complete picture of the weaknesses of the experimental process and the uncertainties introduced. Therefore, it will facilitate the task of attributing the discrepancies to specific aspects of the procedure. Furthermore, it allows to avoid loss of information during documentation.
- Monitoring several parameters will be useful in cases when parameter identification process is required. For example, recall the five values of U_{if}, simulated in the previous section. The case of $U_{\mathrm{if}} = 220\,\mathrm{W/(m^2\,K)}$ yields 5.7% more adsorbed mass than the case of $U_{\mathrm{if}} = 140\,\mathrm{W/(m^2\,K)}$. Evidently, knowledge of the experimental value of the adsorbed mass would allow to compare it to the simulated value for the various U_{if}, and thus allow to choose the best fitted value of the latter.
- Ability to perform multiple experiments for various operating conditions.
- Use the adsorption pair based on the prioritized interests of CTTC laboratory, namely the silica gel - water adsorption pair. The latter is commonly used in space cooling applications while the adsorption pair used in the experiment is mostly used in lower temperature applications.

As already mentioned, in the context of this thesis, the necessity of this experiment was identified, the experiment was conceptually conceived and some preparatory tasks were performed. Its complete preparation and implementation form part of the future research in CTTC.

References

[1] A. Mhimid. Theoretical study of heat and mass transfer in a zeolite bed during water desorption: validity of local thermal equilibrium assumption. *International Journal of Heat and Mass Transfer*, 41(19):2967 – 2977, 1998.

[2] G.G. Ilis, M. Mobedi, and S. Ülkü. Comparison of uniform and non-uniform pressure approaches used to analyze an adsorption process in a closed type adsorbent bed. *Transport in Porous Media*, 98:81 – 101, 2013.

[3] M.H. Chahbani, J. Labidi, and J. Paris. Effect of mass transfer kinetics on the performance of adsorptive heat pump systems. *Applied Thermal Engineering*, 22(1):23 – 40, 2002.

[4] Y.L. Zhao, E. Hu, and A. Blazewicz. A non-uniform pressure and transient boundary condition based dynamic modeling of the adsorption process of an adsorption refrigeration tube. *Applied Energy*, 90(1):280 – 287, 2012.

[5] Y. Zhao, E. Hu, and A. Blazewicz. Dynamic modelling of an activated carbon–methanol adsorption refrigeration tube with considerations of interfacial convection and transient pressure process. *Applied Energy*, 95:276 – 284, 2012.

[6] L.Z. Zhang and L. Wang. Momentum and heat transfer in the adsorbent of a waste-heat adsorption cooling system. *Energy*, 24(7):605 – 624, 1999.

[7] S. Jribi, T. Miyazaki, B.B. Saha, S. Koyama, S. Maeda, and T. Maruyama. CFD simulation and experimental validation of ethanol adsorption onto activated carbon packed heat exchanger. *International Journal of Refrigeration*, 74:345 – 353, 2017.

[8] L. Luo and D. Tondeur. Transient thermal study of an adsorption refrigerating machine. *Adsorption*, 6(1):93 – 104, 2000.

[9] J.W. Wu, M.J. Biggs, and E.J. Hu. Dynamic model for the optimisation of adsorption-based desalination processes. *Applied Thermal Engineering*, 66(1):464 – 473, 2014.

[10] B.B. Saha, A. Chakraborty, S. Koyama, and Y.I. Aristov. A new generation cooling device employing $CaCl_2$-in-silica gel–water system. *International Journal of Heat and Mass Transfer*, 52(1):516 – 524, 2009.

[11] L.M. Sun, N. Ben Amar, and F. Meunier. Numerical study on coupled heat and mass transfers in an absorber with external fluid heating. *Heat Recovery Systems and CHP*, 15(1):19 – 29, 1995.

[12] H.T. Chua, K.C. Ng, W. Wang, C. Yap, and X.L. Wang. Transient modeling of a two-bed silica gel–water adsorption chiller. *International Journal of Heat and Mass Transfer*, 47(4):659 – 669, 2004.

[13] Q.W. Pan, R.Z. Wang, and L.W. Wang. Comparison of different kinds of heat recoveries applied in adsorption refrigeration system. *International Journal of Refrigeration*, 55:37 – 48, 2015.

[14] K.C. Leong and Y. Liu. Numerical study of a combined heat and mass recovery adsorption cooling cycle. *International Journal of Heat and Mass Transfer*, 47(22):4761 – 4770, 2004.

[15] L. Marletta, G. Maggio, A. Freni, M. Ingrasciotta, and G. Restuccia. A non-uniform temperature non-uniform pressure dynamic model of heat and mass transfer in compact adsorbent beds. *International Journal of Heat and Mass Transfer*, 45(16):3321 – 3330, 2002.

[16] E. Voyiatzis, J.A. Palyvos, and N.C. Markatos. Heat-exchanger design and switching-frequency effects on the performance of a continuous type solar adsorption chiller. *Applied Energy*, 85(12):1237 – 1250, 2008.

[17] W.D. Wu, H. Zhang, and D.W. Sun. Mathematical simulation and experimental study of a modified zeolite 13X–water adsorption refrigeration module. *Applied Thermal Engineering*, 29(4):645 – 651, 2009.

[18] F.B. Cortés, F. Chejne, J.M. Mejía, and C.A. Londoño. Mathematical model of the sorption phenomenon of methanol in activated coal. *Energy Conversion and Management*, 50(5):1295 – 1303, 2009.

[19] H. Niazmand and I. Dabzadeh. Numerical simulation of heat and mass transfer in adsorbent beds with annular fins. *International Journal of Refrigeration*, 35(3):581 – 593, 2012.

[20] M. Mahdavikhah and H. Niazmand. Effects of plate finned heat exchanger parameters on the adsorption chiller performance. *Applied Thermal Engineering*, 50(1):939 – 949, 2013.

[21] H. Demir. The effect of microwave regenerated adsorbent bed on the performance of an adsorption heat pump. *Applied Thermal Engineering*, 50(1):134 – 142, 2013.

[22] M. Duquesne, J. Toutain, A. Sempey, S. Ginestet, and E. Palomo del Barrio. Modeling of a nonlinear thermochemical energy storage by adsorption on zeolites. *Applied Thermal Engineering*, 71(1):469 – 480, 2014.

[23] H.R. Ramji, S.L. Leo, and M.O. Abdullah. Parametric study and simulation of a heat-driven adsorber for air conditioning system employing activated carbon–methanol working pair. *Applied Energy*, 113:324 – 333, 2014.

[24] S.W. Hong, S.H. Ahn, O.K. Kwon, and J.D. Chung. Optimization of a fin-tube type adsorption chiller by design of experiment. *International Journal of Refrigeration*, 49:49 – 56, 2015.

[25] İ. Solmuş, C. Yamali, C. Yildirim, and K. Bilen. Transient behavior of a cylindrical adsorbent bed during the adsorption process. *Applied Energy*, 142:115 – 124, 2015.

[26] R.H. Mohammed, O. Mesalhy, M.L. Elsayed, and L.C. Chow. Novel compact bed design for adsorption cooling systems: Parametric numerical study. *International Journal of Refrigeration*, 80:238 – 251, 2017.

[27] M.M. Kowsari, H. Niazmand, and M.M. Tokarev. Bed configuration effects on the finned flat-tube adsorption heat exchanger performance: Numerical modeling and experimental validation. *Applied Energy*, 213:540 – 554, 2018.

[28] B. Golparvar, H. Niazmand, A. Sharafian, and A.A. Hosseini. Optimum fin spacing of finned tube adsorber bed heat exchangers in an exhaust gas-driven adsorption cooling system. *Applied Energy*, 232:504 – 516, 2018.

[29] M.B. Elsheniti, M.A. Hassab, and A.E. Attia. Examination of effects of operating and geometric parameters on the performance of a two-bed adsorption chiller. *Applied Thermal Engineering*, 146:674 – 687, 2019.

[30] M. Louajari, A. Mimet, and A. Ouammi. Study of the effect of finned tube adsorber on the performance of solar driven adsorption cooling machine using activated carbon–ammonia pair. *Applied Energy*, 88(3):690 – 698, 2011.

[31] G.J.V.N. Brites, J.J. Costa, and V.A.F. Costa. Influence of the design parameters on the overall performance of a solar adsorption refrigerator. *Renewable Energy*, 86:238 – 250, 2016.

[32] C. Corgnale, B. Hardy, R. Chahine, and D. Cossement. Hydrogen desorption using honeycomb finned heat exchangers integrated in adsorbent storage systems. *Applied Energy*, 213:426 – 434, 2018.

[33] M. Beckner and A. Dailly. A pilot study of activated carbon and metal–organic frameworks for methane storage. *Applied Energy*, 162:506 – 514, 2016.

[34] N.A.A. Qasem, R. Ben-Mansour, and M.A. Habib. An efficient CO_2 adsorptive storage using MOF-5 and MOF-177. *Applied Energy*, 210:317 – 326, 2018.

[35] R.T Yang. *Gas separation by adsorption processes*. Butterworth Publishers, Boston, 1987.

[36] R. Ben-Mansour, M.A. Habib, O.E. Bamidele, M. Basha, N.A.A. Qasem, A. Peedikakkal, T. Laoui, and M. Ali. Carbon capture by physical adsorption: Materials, experimental investigations and numerical modeling and simulations – a review. *Applied Energy*, 161:225 – 255, 2016.

[37] A. Bonilla-Petriciolet, D.I. Mendoza-Castillo, and H.E Reynel-Ávila. *Adsorption processes for water treatment and purification*. Springer International Publishing, 2017.

[38] O. Lehmkuhl, C.D. Perez-Segarra, R. Borrell, M. Soria, and A. Oliva. TermoFluids: A new parallel unstructured CFD code for the simulation of turbulent industrial problems on low cost PC Cluster. In *Parallel Computational Fluid Dynamics 2007*, pages 275–282. Springer Berlin Heidelberg, 2009.

[39] A.D. Nield and A. Bejan. *Convection in Porous Media*. Springer-Verlag New York, 4th edition, 2013.

[40] X. Wang, W. Zimmermann, K.C. Ng, A. Chakraboty, and J.U. Keller. Investigation on the isotherm of silica gel+water systems. *Journal of Thermal Analysis and Calorimetry*, 76(2):659 – 669, 2004.

[41] F. Rouquerol, J. Rouquerol, K.S.W. Sing, P. Llewellyn, and G. Maurin. *Adsorption by Powders and Porous Solids*. Elsevier, 2nd edition, 2014.

[42] M. Suzuki. *Adsorption Engineering*. Copublished by: Kodansha, Tokyo and Elsevier Science Publishers, Amsterdam, 1990.

[43] N. Wakao and S. Kaguei. *Heat and Mass Transfer in Packed Beds*. Gordon and Breach Science Publishers, 1982.

[44] W. Wagner and H.J. Kretzschmar. *International Steam Tables - Properties of Water and Steam based on the Industrial Formulation IAPWS-IF97*. Springer-Verlag Berlin Heidelberg, 2nd edition, 2008.

[45] T.L. Bergman, A.S. Lavine, F.P. Incropera, and D.P. DeWitt. *Fundamentals of Heat and Mass Transfer*. John Wiley and Sons, 7th edition, 2011.

[46] S. Santamaria, A. Sapienza, A. Frazzica, A. Freni, I.S. Girnik, and Y.I. Aristov. Water adsorption dynamics on representative pieces of real adsorbers for adsorptive chillers. *Applied Energy*, 134:11 – 19, 2014.

[47] I.S. Glaznev and Y.I. Aristov. The effect of cycle boundary conditions and adsorbent grain size on the water sorption dynamics in adsorption chillers. *International Journal of Heat and Mass Transfer*, 53(9):1893 – 1898, 2010.

[48] American Institute for Aeronautics and Astronautics. Guide for the Verification and Validation of Computational Fluid Dynamics Simulations. AIAA-G-077-1998, Reston, VA, 1998.

[49] C. D. Perez-Segarra, C. Farre, J. Cadafalch, and A. Oliva. Analysis of Different Numerical Schemes for the Resolution of Convection-Diffusion Equations using Finite-Volume Methods on Three-Dimensional Unstructured Grids. Part I: Discretization Schemes. *Numerical Heat Transfer, Part B: Fundamentals*, 49(4):333–350, 2006.

[50] Oriol Lehmkuhl Barba. *Numerical resolution of turbulent flows on complex geometries*. PhD thesis, Universitat Politècnica de Catalunya, 2012.

[51] L.Z. Zhang. A three-dimensional non-equilibrium model for an intermittent adsorption cooling system. *Solar Energy*, 69(1):27 – 35, 2000.

[52] H.Z. Hassan, A.A. Mohamad, and R. Bennacer. Simulation of an adsorption solar cooling system. *Energy*, 36(1):530 – 537, 2011.

[53] G. Restuccia, A. Freni, S. Vasta, and Y. Aristov. Selective water sorbent for solid sorption chiller: experimental results and modelling. *International Journal of Refrigeration*, 27(3):284 – 293, 2004.

[54] H. Niazmand, H. Talebian, and M. Mahdavikhah. Effects of particle diameter on performance improvement of adsorption systems. *Applied Thermal Engineering*, 59(1):243 – 252, 2013.

3

Numerical studies of adsorption packed bed reactors

Contents of this chapter have been included in :
- G. Papakokkinos, J. Castro, J. Lopez and A. Oliva, A generalized computational model for the simulation of adsorption packed bed reactors – Parametric study of five reactor geometries for cooling applications, *Applied Energy*, 235 (2), 409-427, 2018
- G. Papakokkinos, J. Castro, C. Oliet and A. Oliva, Computational investigation of the hexagonal honeycomb adsorption reactor for cooling applications, *Under review*

3.1 Introduction

This chapter pertains to the presentation of the numerical studies that have been conducted using the developed model for the simulation of adsorption packed bed reactors, which is presented in Chapter 2.

Two major numerical studies have been conducted. One of the distinctive features of the developed computational model is its capability of simulating any potential reactor geometry. Thus, the scope of the two numerical studies is aligned with this feature.

The objective of the first study is to investigate five reactor geometries and provide a comparative study among them. Although various investigations can be found in the literature with respect to different geometries, a reliable comparison between them is not possible. The latter is a consequence of several reasons. The comparability across these studies is low since (i) the studies use different adsorption pairs, (ii) the simulation models are based on different assumptions or methods, (iii) the reported results are not sufficient for comparison and (iv) some models are not validated or the validation approaches are not the same. For these reasons, a comparison between studies might lead to unsafe conclusions. Conducting simulations of different reactor

geometries with the same computational model and within the same framework increases the comparability of the geometries and allows to extract more reliable conclusions. As it will be explained later, the study involves the quantification of the Specific Cooling Power during the adsorption phase. This study is presented in Section 3.3.

In the second study, the developed model is employed for the numerical investigation of a reactor geometry that has not been studied thoroughly hitherto. This geometry is the hexagonal honeycomb adsorption reactor. This is a bioinspired geometry that mimics the way bees build their hives [1]. According to the honeycomb conjecture – proven mathematically in 1999 – this hexagonal tiling is the partition of the plane in regions of equal area with the minimum perimeter [2]. From an adsorption reactor perspective, this can be interpreted as the partition of a planar reactor that requires the minimum amount of heat exchanger fins for a given adsorbent cell size. The study involves the characterization of the Coefficient of Performance and the Specific Cooling Power. A parametric study is conducted with respect to the three dimensions that define the geometry, as well as for various operating conditions. This study is presented in Section 3.4.

Subsequently, Section 3.5 approaches the results from an engineering perspective, focusing the discussion on practical aspects of different applications.

3.2 Literature review

The literature review of this chapter is dedicated to the studies that employed computational models for the investigation of the reactor performance under different geometrical configurations and operational parameters.

With respect to the finless tubular reactor, Solmuş et al. [3] used a two-dimensional axisymmetric model to simulate a cylindrical reactor with a vapor passage in its center, employing the adsorption pair water-silica gel. They studied the influence of the packed bed thickness and the impact of operational parameters, such as the driving heat source and cooling temperatures, as well as the condenser and evaporator pressures. Liu and Leong [4] studied numerically the finless cylindrical reactor with annular vapor passage, employing water and zeolite 13X as the adsorption pair. They investigated how the COP and the SCP are influenced by the condenser, evaporator,

desorption and adsorption temperatures, as well as by the velocity of the heat transfer fluid.

Regarding the tubular reactor with circular radial fins, Niazmand and Dabzadeh [5] studied the influence of fin pitch and fin length, using a two-dimensional axisymmetric model. They concluded that the incorporation of fins reduces significantly the reactor bed size, at the cost of a slightly lower COP. Saha et al. [6] investigated numerically the same reactor geometry. They studied the impact of the cycle time and driving temperature on the performance of the system in terms of cooling capacity and COP, employing two different adsorbents. In the same direction, Hong et al. [7] studied the effect of several parameters, concluding that the driving heat source temperature has the strongest influence on the SCP. Khanam et al. [8] presented a study of the cycle time influence on the performance of the system, using a computational model based on ANSYS Fluent software. They reported that the SCP exhibits a maximum at cycle time of 800 s, whereas COP increases as a function of the cycle time. Elsheniti et al. [9] presented a two-dimensional axisymmetric model based on COMSOL software. The model was used to simulate a finned tube adsorption reactor. According to their findings, they proposed smaller fin height and larger fin number, shorter desorption time by a factor of 0.7-0.9 with respect to the adsorption time, and a turbulent regime for the heat transfer fluid. Mitra et al. [10] presented a two-dimensional model based on the ANSYS Fluent software. The model was used to investigate three aspect ratios of the rectangular packed bed domain, as well as two adsorbent particles size.

Apart from circular radial fins, tubular reactors were investigated with axial (longitudinal) and radial square fins. Golparvar et al. [11] presented a three-dimensional model based on cylindrical coordinates. The model was used for the simulation of tubular reactors with radial and axial fins, in a vehicular air-conditioning system driven by the exhaust gases of the engine. They studied the influence of the fin height and fin spacing on the SCP and COP. They concluded that the reactor with radial fins provides 10% higher cooling capacity with respect to the reactor with axial fins. Mahdavikhah and Niazmand [12] studied the impact of fin pitch and fin length on the performance of a tubular reactor with square radial fins, using a three-dimensional model. According to their results, they emphasized the importance of these geometrical parameters on the performance of the system. Ramji et al. [13] used the ANSYS software to investigate a tubular adsorber reactor with axial fins, driven by exhaust heat. The influence of the wall thickness on the performance of the system was studied.

With respect to non-tubular geometries, Mohammed et al. [14] studied a reactor geometry consisting of two rectangular layers of packed beads separated by a vapor passage. They numerically investigated the influence of the particle diameter, bed thickness and thermal conductivity on the SCP. In a subsequent work, Mohammed et al. [15] proposed a reactor design based on rectangular modular cells. They used a computational model based on COMSOL software, which they experimentally validated by comparing results regarding the average bed temperature and average water uptake. They investigated numerically the influence of the operating temperatures and the convective heat transfer coefficient on the SCP. Kowsari et al. [16] used a three-dimensional model for the investigation of the geometrical configuration of the trapezoidal finned flat tube heat exchanger.

As it arises from the literature review, the vast majority of the studies focused on tubular reactors. This tendency results from the models limitations, which based their spatial discretization on cylindrical coordinates. Consequently, the geometric configurations which cannot be simulated by cylindrical coordinates remain relatively underexplored. An example of such underexplored geometry is the hexagonal honeycomb. This is a bioinspired geometry that mimics the way bees build their hives [1]. This structure attracted interest since the antiquity and in 1999, the honeycomb conjecture was proven mathematically. The latter states that this hexagonal tiling is the partition of the plane in regions of equal area with the minimum perimeter [2]. From an adsorption reactor perspective, this can be interpreted as the partition of a planar reactor that requires the minimum amount of fins for a given adsorbent cell size. Although the hexagonal honeycomb structure is employed within various engineering contexts [17–19] – to the author's knowledge, a complete study and characterization for adsorption cooling reactors has not been reported in the literature, hitherto. Within the context of the adsorption cooling, two works studied partially two variants of the honeycomb adsorption reactor [20, 21]. It should be noted that, although the honeycomb structure is employed in these works, the overall geometric configuration of the adsorption reactor is not the same. In [20], the HTF channel is between the posteriors of two ensembles of honeycomb cells (Figure 3.13), while in [21] the HTF channels are at the laterals of an ensemble of honeycomb cells. This difference renders the geometries as two different reactors. Shi et al. [20] studied the honeycomb reactor using a COMSOL software model. Their analysis was limited to the adsorption process, evaluating the adsorption uptake for different cell geometries and cooling water Reynolds numbers. Sosnowski et al. [21] studied the proposed

geometry using ANSYS Fluent software, focusing only on the desorption process. From their simulations, they reported the temperature increase and the logarithmic mean temperature difference of the HTF.

Consequently, the literature review reveals the absence of (i) a comparative parametric study between various geometries of adsorption packed bed reactors and (ii) a thorough investigation of the hexagonal honeycomb adsorption reactor.

3.3 Specific Cooling Power for five adsorption reactor geometries

The objective of this study is to contribute to the ongoing research, dedicated to the design of the adsorption reactor. The intention is to study the five geometries under consideration and to provide a reliable comparison between them. As elaborated earlier, the comparison between different studies across the literature is not always reliable.

This study pertains to the quantification of the Specific Cooling Power during the adsorption phase. The computation of the COP – which is conducted for the honeycomb reactor in Section 3.4 – requires significantly longer simulations, since for its calculation the entire thermodynamic cycle must be simulated repetitively, until cyclic behavior is attained. The latter forms part of ongoing studies and the presented results involve only the SCP in the adsorption phase. However, as elaborated in Sections 3.3.2 and 3.3.6.4, a similar COP should be expected for geometries with the same Solid Volume Fraction.

3.3.1 Geometries under investigation

The studied geometries – illustrated in Figure 3.1 – are:

- GEOM-A: circular channel with radial fins
- GEOM-B: circular channel with square fins
- GEOM-C: circular channel with axial fins
- GEOM-D: rectangular channel with corrugated fins
- GEOM-E: rectangular channel with hexagonal honeycomb fins

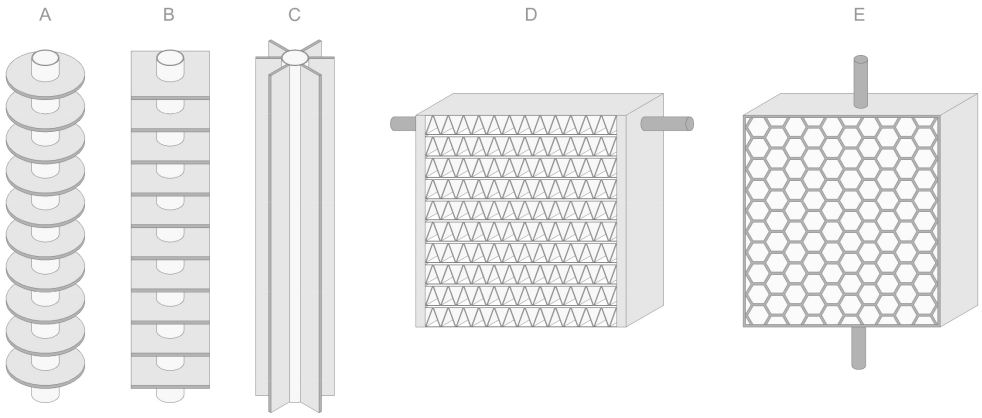

Figure 3.1: Adsorption reactor geometries under investigation

In GEOM-A,B,C, the HTF passes through the circular channel in the center of the geometry. In GEOM-D, the HTF enters from one side and it is distributed to various horizontal rectangular channels, which are incorporated between the metal plates with the corrugated fins. In GEOM-E, the HTF passes through a vertical rectangular channel, which is formed by two metal plates with incorporated hexagonal honeycomb fins.

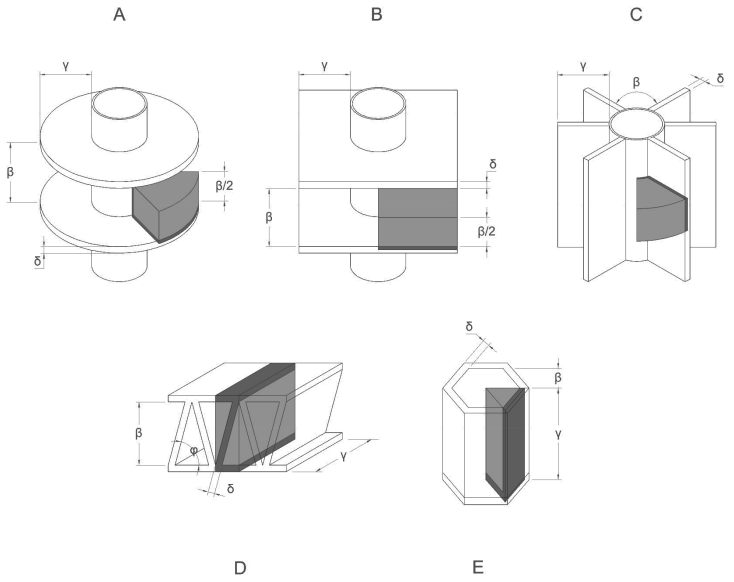

Figure 3.2: Simulated domains taking into account periodicities and symmetries

The simulated domain – and thus, the computational time – can be reduced significantly by taking into consideration the periodicities and the symmetries of the geometries. The reduction of the simulated domain is based on the assumptions (iv) and (v) from Section 3 in Chapter 2. These assumptions involve considering constant HTF temperature and ideally insulated reactor. The adoption of these assumptions allow to interpret the results of the reduced geometries as representative for the entire reactor. The reduced geometries are illustrated in Figure 3.2. Figure 3.3 illustrates the spatial discretization and the boundary conditions (as elaborated in Section 2.3.3) for each geometry. In GEOM-A and GEOM-C, symmetries allow to reduce the problem to two-dimensional, while GEOM-B, GEOM-D and GEOM-E are three-dimensional problems.

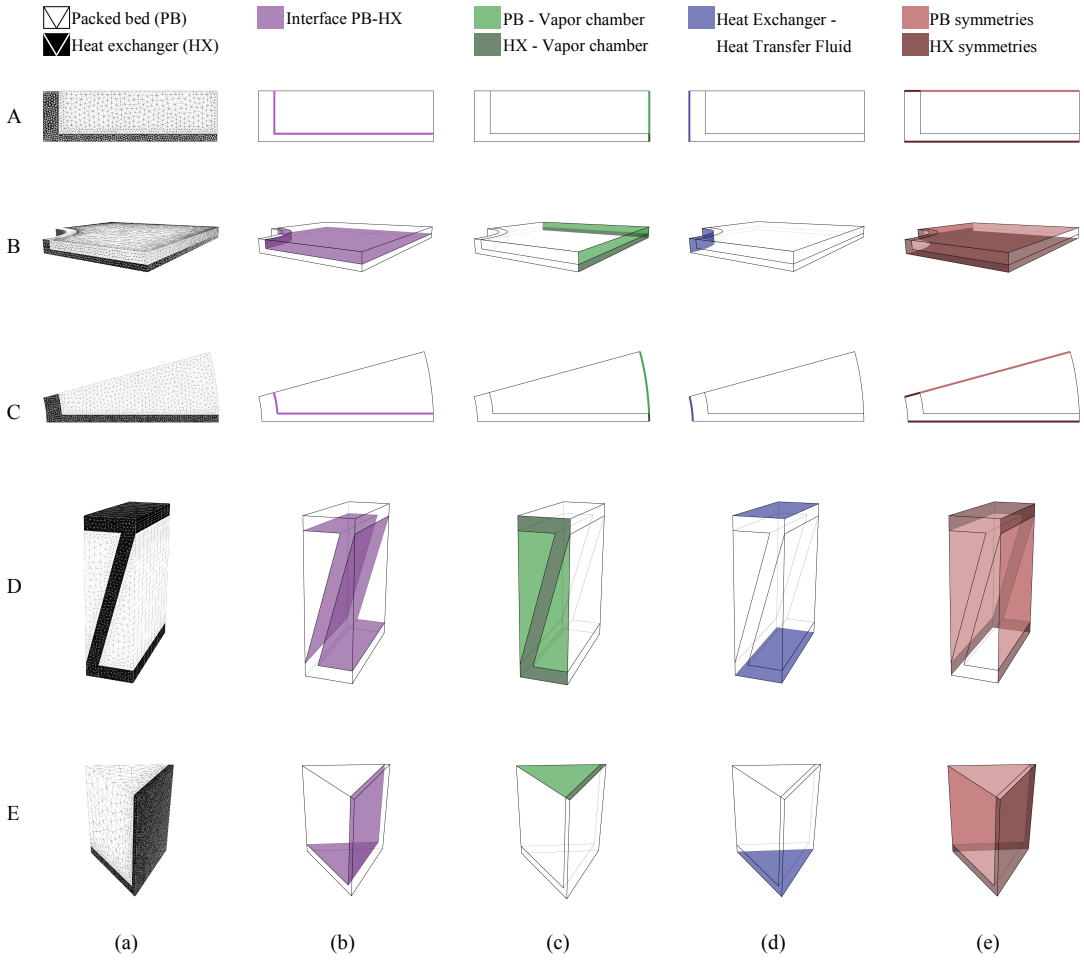

Figure 3.3: (a) Geometry discretization, (b) Interface between the two domains, (c) Face exposed to the vapor chamber for the two domains, (d) Interface between heat exchanger and heat transfer fluid and (e) Symmetry faces of the two domains

3.3.2 Comparability of the geometries

One scope of this study – apart from the individual study of each geometry – is to be able to compare the performance of the reactor geometries under consideration.

This section presents the foundations and conventions that render the geometries comparable.

As illustrated in Figure 3.2, the studied geometries can be defined by three dimensions (β, γ, δ). Only GEOM-D requires an additional parameter, the angle ϕ, which in the context of this study is set to 75°. As it can be observed, the two of the three geometrical parameters that define each geometry are readily comparable. These parameters concern the fin, namely, the mass of solid which is in contact with the HTF channel and extends inside the packed bed in order to enhance the heat transfer. The fin thickness δ and the fin length γ are comparable across the five geometries. The latter is representative of the maximum distance that the gas is required to traverse inside the packed bed (from gas inlet).

The third parameter – denoted as β – is not comparable across the five geometries. In the case of GEOM-A and GEOM-B, β is the fin pitch, defined as the distance between two fins, whereas for GEOM-C, β is the fin pitch, defined as the angle between two fins. For GEOM-D and GEOM-E, β cannot be defined with the same clarity as for GEOM-A,B,C. Consequently, the complete definition of the geometries requires the introduction of a parameter that would allow the comparison of the geometries. The introduced parameter is the Solid Volume Fraction (SVF), defined as the ratio percentage of the heat exchanger solid volume to the total volume of the reactor (equation 3.1). This parameter is meaningful, in the sense that it is related to the performance of the adsorption cooling system. As already explained, the mass of the heat exchanger solid corresponds to the additional input energy which is lost in the desorption phase of every cycle and thus, it affects the COP. For a given SVF, a similar COP is expected across different geometries, as elaborated in Section 3.3.6.4. Imposing the SVF allows to calculate the parameter β through the relevant geometric relations and equation 3.1.

$$\mathrm{SVF} = \frac{V_{\mathrm{solid}}}{V_{\mathrm{total}}} \times 100\% \tag{3.1}$$

3.3.3 Parameters under investigation

For the geometric study, a total of 65 simulations were performed, 13 for each geometry. The base case is for fin thickness δ=1 mm, fin length γ=10 mm and solid volume

fraction SVF=40 %. For each of these parameters, a parametric study was conducted. By keeping the other two parameters constant, the SVF was studied for 20, 30, 40, 50 and 60 %, the fin thickness δ for 0.5, 1, 2, 3 , 4 mm and the fin length γ for 5, 10, 20, 30 and 40 mm. Table 3.1 summarizes the reactor dimensions of all the simulated cases.

Table 3.1: Dimensions of the simulated geometries

SVF	δ	γ	β according to geometry				
[%]	[mm]	[mm]	A[mm]	B[mm]	C[°]	D[mm]	E[mm]
20	1	10	5.38	4.97	30.48	24.16	8.75
30	1	10	2.82	2.68	18.22	14.57	4.14
40	1	10	1.72	1.66	12.99	9.75	2.50
50	1	10	1.11	1.08	10.10	6.83	1.66
60	1	10	0.73	0.71	8.26	4.85	1.14
40	1	5	2.15	1.92	18.97	9.75	3.23
40	1	10	1.72	1.66	12.99	9.75	2.50
40	1	20	1.57	1.56	8.67	9.75	2.22
40	1	30	1.54	1.53	6.61	9.75	2.14
40	1	40	1.52	1.52	5.35	9.75	2.10
40	0.5	10	0.86	0.83	6.50	6.64	1.25
40	1	10	1.72	1.66	12.99	9.75	2.50
40	2	10	3.44	3.33	25.98	15.63	5.00
40	3	10	5.16	4.99	38.98	21.37	7.50
40	4	10	6.88	6.65	51.97	27.05	10.00

The meshes were created using Ansys ICEM CFD mesh generator. Evidently, the necessity of quick mesh generation arose, since for each of the 65 cases, multiple meshes were required for the mesh independence studies and the determination of the mesh used in the simulations. Scripting tools were developed for this task. For each geometry, a script was developed that executes the following: (i) receive input for the parameters that define the geometry, (ii) receive input for the meshing parameters, (iii) construct an ICEM script for the automatic generation of the geometry and the mesh, (iv) launch ICEM script and (v) post-process of the mesh (transformation to TermoFluids format, parallelization of CPUs and other preparatory tasks).

For the presented geometric study, the heat exchanger material is copper. The simulations were repeated with aluminium as heat exchanger material and the results are commented in Section 3.3.6.3.

3.3.4 Simulation details

For the simulation initial conditions, the reactor is considered desorbed and precooled. The initial adsorbed mass w_{init} corresponds to the equilibrium capacity for the condenser pressure and HTF desorption temperature of a typical cycle ($P = 4243\,\text{Pa}$ and $T = 80\,^{\circ}\text{C}$). At the beginning of the simulation, the reactor is connected to the evaporator and the adsorption process is initiated. As already explained, reaching equilibrium is not of practical interest due to the significant drop of adsorption, and consequently, of cooling production. Therefore, the adsorption process is terminated earlier. For the termination, the relative average adsorbed mass $\overline{w}_{\text{rel}}$ is evaluated as in equation 3.2. For its computation, the adsorbed mass w is spatially averaged throughout the packed bed domain. Then, it is converted to the percentage of the difference between the initial adsorbed mass w_{init} and the adsorption equilibrium capacity w^* that corresponds to the evaporator pressure and the HTF adsorption temperature ($P = 1228\,\text{Pa}$ and $T = 30\,^{\circ}\text{C}$). The latter is the adsorbed mass that would have been achieved if the process continued for a relatively long period. The simulation is terminated when $\overline{w}_{\text{rel}}$ becomes 70 % and the time required for this process is denoted as $t_{70\%}$.

$$\overline{w}_{\text{rel}} = \frac{\overline{w} - w_{\text{init}}}{w^*\big|_{(P_{\text{evap}}, T_{\text{HTF}})} - w_{\text{init}}} \times 100\% \tag{3.2}$$

Table 3.2 summarizes the input parameters of the computational model.

3.3.5 Evaluation parameters and results interpretation

The simulation results are evaluated based on the average Specific Cooling Power of the adsorption phase SCP_{ads} [$\text{W kg}_{\text{s}}^{-1}$] (equation 3.3) and the $t_{70\%}$, as defined above. These values are representative of the effectiveness of the reactor in terms of heat and mass transfer.

Table 3.2: Model input parameters

Input parameter	Value	Unit	Ref.
$c_{p_{\mathrm{Al}}}$	903	$\mathrm{J\,kg^{-1}\,K^{-1}}$	[22]
$c_{p_{\mathrm{Cu}}}$	385	$\mathrm{J\,kg^{-1}\,K^{-1}}$	[22]
$c_{p_{\mathrm{s,dry}}}$	924	$\mathrm{J\,kg^{-1}\,K^{-1}}$	[23]
d_{p}	0.0005	m	[24]*
D_0	2.54×10^{-4}	$\mathrm{m^2\,s^{-1}}$	[25]
E_a	4.2×10^{4}	$\mathrm{J\,mol^{-1}}$	[25]
U_{if}	100	$\mathrm{W\,m^{-2}\,K^{-1}}$	[26]
K_0	7.3×10^{-13}	$\mathrm{kg_w\,kg_s\,Pa^{-1}}$	[23]
q_m	0.45	$\mathrm{kg_w\,kg_s^{-1}}$	[23]
ΔH_{ads}	2.693×10^{6}	$\mathrm{J\,kg^{-1}}$	[23]
ε_{b}	0.3955	-	[23]**
ε_{p}	0.4287	-	[23]**
ε_{t}	0.6546	-	[23]**
ρ_{s}	2027	$\mathrm{kg\,m^{-3}}$	[23]
ρ_{Al}	2702	$\mathrm{kg\,m^{-3}}$	[22]
ρ_{Cu}	8933	$\mathrm{kg\,m^{-3}}$	[22]
λ_{Al}	237	$\mathrm{W\,m^{-1}\,K^{-1}}$	[22]
λ_{Cu}	401	$\mathrm{W\,m^{-1}\,K^{-1}}$	[22]
λ_{s}	0.198	$\mathrm{W\,m^{-1}\,K^{-1}}$	[23]
τ	12	-	[23]

**Average particle diameter of the range provided by the manufacturer [24]*
***Calculated based on the apparent, skeletal and particle bulk densities [23]*

$$\mathrm{SCP_{ads}} = \frac{\Delta m \times \Delta H_{\mathrm{evap}}}{M_s \times t_{70\%}} = \frac{\Delta w \times \Delta H_{\mathrm{evap}}}{t_{70\%}} \tag{3.3}$$

where Δm is the difference between final and initial adsorbed mass contained in the reactor, namely, the total mass that entered the reactor from the evaporator. M_s is the dry solid adsorbent mass and ΔH_{evap} is the latent heat of evaporation of water.

It should be emphasized that in this performance metric, the instantaneous SCP is averaged throughout the adsorption phase. It should not be confused with $\mathrm{SCP_{cycle}}$, which is reported in Section 3.4, where the instantaneous SCP is averaged throughout the entire thermodynamic cycle.

Furthermore, another aspect for the evaluation of the results is the temporal evolution of the instantaneous Specific Cooling Power SCP_{inst}. The latter is associated to the smooth operation of the evaporator and it should be taken into account during the design stage.

The SCP_{ads} and the $t_{70\%}$ are plotted together in one graph. The former on the left vertical axis and the latter on the right vertical axis. It should be noted that the $t_{70\%}$ axis is reversed and non-linear since $SCP_{ads} \propto \frac{1}{t_{70\%}}$. As $t_{70\%}$ is different for each case, the results of SCP_{inst} are plotted against the non-dimensional time $t^* = t \ / \ t_{70\%}$, for ease of comparison between different cases.

3.3.6 Results

3.3.6.1 Average Specific Cooling Power SCP_{ads} and $t_{70\%}$

Figure 3.4 illustrates the effect of the solid volume fraction on the performance of the reactor, based on simulations of the five geometries for SVF 20, 30, 40, 50 and 60% ($\delta = 1\,\text{mm}$, $\gamma = 10\,\text{mm}$). Anticipatedly, increasing the solid volume fraction of the reactor increases the SCP_{ads} and reduces the $t_{70\%}$. This applies to all geometries under consideration. While the fin thickness and length are kept identical, increasing the SVF means that the fins are more densely distributed. Therefore, the heat transfer is more effective. Consequently, the exothermic energy released as a result of adsorption is removed more effectively and the temperature is maintained lower. Lower temperature corresponds to a higher adsorption equilibrium capacity, thus a higher adsorption rate. As a result, the $\overline{w}_{rel}$ reaches 70% at a lower $t_{70\%}$ and, consequently the SCP_{ads} increases. In the opposite case of lower SVF, the fins are less densely distributed and thus, the cooling of the reactor is less effective. Therefore, higher temperatures are developed, corresponding to lower adsorption equilibrium capacity and thus, lower adsorption rate and SCP_{ads}. Indicatively, for SVF=20 %, the SCP_{ads} lies between 144.6 W/kg_s (GEOM-E) and 179.7 W/kg_s (GEOM-A), whereas for SVF=60 %, the SCP_{ads} lies between 413.4 W/kg_s (GEOM-B) and 535.8 W/kg_s (GEOM-D). The time required to achieve $\overline{w}_{rel}$ of 70 %, $t_{70\%}$, lies for SVF=20 % between 1529.9 s (GEOM-A) and 1901.9 s (GEOM-E), whereas for SVF=60 % it ranges between 513.2 s (GEOM-D) and 665.1 s (GEOM-B). It is interesting to observe that for SVF=20 % the geometries have similar performance since the minimum and maximum SCP_{ads} differ by only 35.1 W/kg_s, while this difference for SVF=60 % reaches 122.4 W/kg_s. This demon-

strates that the design of the reactor becomes more significant in higher SVFs. For the geometries based on circular channels (GEOM-A,B,C), the SCP_{ads} for SVF=60 % is on average 2.56 times its value for SVF=20 %. For the geometries based on rectangular channels (GEOM-D,E), the SCP_{ads} for SVF=60 % is on average 3.43 times its value for SVF=20 %. As it arises, the Solid Volume Fraction influences drastically the SCP_{ads} of the reactor.

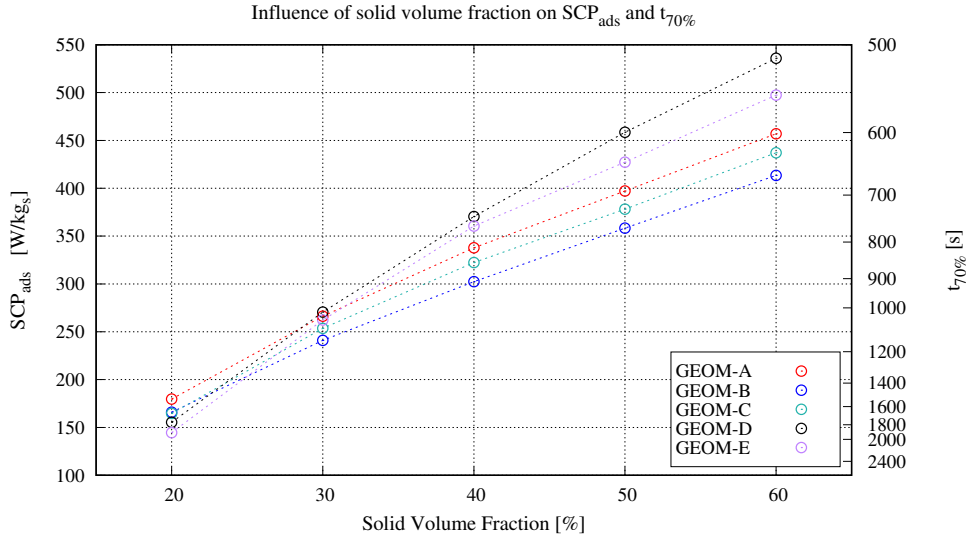

Figure 3.4: Results comparison for the influence of Solid Volume Fraction on SCP_{ads} (left y-axis) and $t_{70\%}$ (right y-axis, reversed)

Figure 3.5 shows the impact of the fin length on the SCP_{ads} of each geometry for γ values of 5, 10, 20, 30 and 40 mm ($\delta = 1$ mm, SVF $= 40$ %). For the smallest fin length $\gamma = 5$ mm, the geometries have very similar performance, since the minimum and maximum SCP_{ads} differ by only 30.6 W/kg_s. While for $\gamma = 5$ mm the performance is almost geometry-independent, for $\gamma = 40$ mm the SCP_{ads} ranges between 71.1 W/kg_s (GEOM-B) and 264.7 W/kg_s (GEOM-D), showing a strong dependence on the geometry. The performance of the reactor is expectedly lower when the fin length increases, since the packed bed volume becomes larger, and thus, the heat and mass transfer are hindered. However, it can be observed that the decrease of the reactor performance is more pronounced on the circular channel geometries (GEOM-A,B,C), with an average

decrease of SCP_{ads} of approximately 80.3 % between fin length of $\gamma = 5\,mm$ and $\gamma = 40\,mm$, whereas GEOM-D and GEOM-E exhibit a decrease of 29.4 % and 49.1 %, respectively.

Moreover, it is interesting to observe that the impact of the fin length variation is neither numerically constant across the studied range nor behaves in a similar manner in the five geometries. The expected performance variation as a result of γ variation is different depending on the region of the studied range, except GEOM-E, which exhibits an almost linear relation between γ and SCP_{ads}. For circular channel geometries, the gradient of the SCP_{ads} curve is much higher at the smaller fin lengths than at larger fin lengths, whereas for GEOM-D the effect is the opposite. In particular, circular channel geometries have in average a $\left(\frac{\Delta SCP_{ads}}{\Delta\gamma}\right)$ of $-12.7\,(W/kg_s)/mm$ for $5\,mm < \gamma < 10\,mm$, whereas for $30\,mm < \gamma < 40\,mm$ their average $\left(\frac{\Delta SCP_{ads}}{\Delta\gamma}\right)$ is $-3.8\,(W/kg_s)/mm$. Contrarily, GEOM-D has $\left(\frac{\Delta SCP_{ads}}{\Delta\gamma}\right)$ of $-0.9\,(W/kg_s)/mm$ for $5\,mm < \gamma < 10\,mm$ and $-4.2\,(W/kg_s)/mm$ for $30\,mm < \gamma < 40\,mm$. To conclude, the performance of circular channel geometries is less sensitive on variations of γ at higher values of γ, while the performance of GEOM-D becomes less sensitive at lower values of γ.

Figure 3.6 illustrates the effect of the fin thickness for δ values of 0.5, 1, 2, 3 and 4 mm ($\gamma = 10\,mm$, SVF = 40 %). As observed in Table 3.1, increasing the fin thickness while maintaining the solid volume fraction steady results to geometries with greater distance between fins. The results in Figure 3.6 quantify the empirical notion that thinner fins densely packed are preferable to thicker fins sparsely packed. Unlike the case of fin length, there are no differences between the performance behavior of the five geometries. At $\delta = 0.5\,mm$, the SCP_{ads} ranges between $344.7\,W/kg_s$ (GEOM-B) and $464.5\,W/kg_s$ (GEOM-E), while at $\delta = 4\,mm$ it becomes less geometry-dependent, ranging between $131.8\,W/kg_s$ and $155.3\,W/kg_s$. The impact of fin thickness on SCP_{ads} ($\frac{\Delta SCP_{ads}}{\Delta\delta}$) is stronger for lower δ. For $0.5\,mm < \delta < 1\,mm$, the ($\frac{\Delta SCP_{ads}}{\Delta\delta}$) ranges between $-84.6\,(W/kg_s)/mm$ (GEOM-B) and $-208.2\,(W/kg_s)/mm$ (GEOM-E), while for $3\,mm < \delta < 4\,mm$ it ranges between $-30.6\,(W/kg_s)/mm$ (GEOM-B) and $-42.5\,(W/kg_s)/mm$ for (GEOM-D). The SCP_{ads} becomes less sensitive to fin thickness variations at higher values of δ.

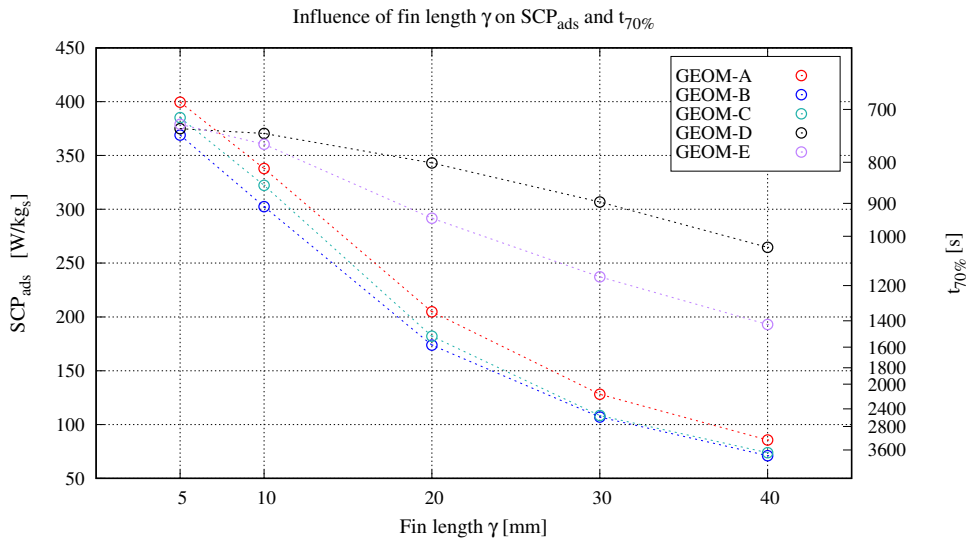

Figure 3.5: Results comparison for the influence of fin length on SCP_{ads} (left y-axis) and $t_{70\%}$ (right y-axis, reversed)

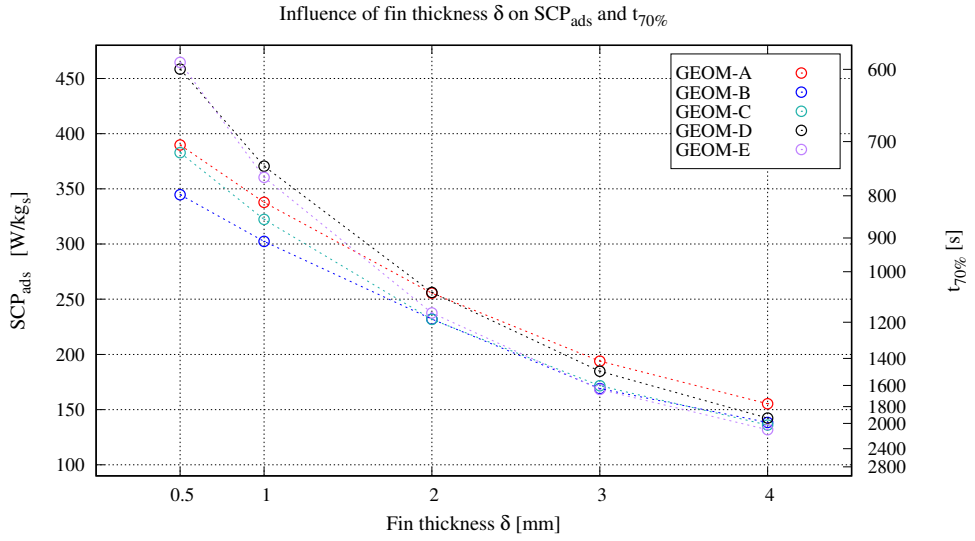

Figure 3.6: Results comparison for the influence of fin thickness on SCP_{ads} (left y-axis) and $t_{70\%}$ (right y-axis, reversed)

3.3.6.2 Instantaneous Specific Cooling Power SCP_{inst}

In the previous section, the parametric study presented the Specific Cooling Power as the average of the adsorption phase. In this section, the objective is to elaborate the influence of the parameters under consideration on the temporal evolution of the instantaneous SCP. It is reminded that the SCP_{inst} is plotted against the non-dimensional time $t^* = t \ / \ t_{70\%}$, for ease of comparison between different cases.

It should be noted that the SCP_{inst} value is expected to be high at the beginning of the adsorption phase and subsequently decreases as equilibrium is approached. It is desired that the temporal evolution of the SCP_{inst} is as smooth as possible. A smooth SCP_{inst} curve corresponds to smooth cooling production throughout the adsorption phase.

For each of the three parameters under consideration – SVF, fin length and fin thickness – four graphs are presented. Two of them pertain to the SCP_{inst} of two representative geometries (one based on circular channel and one based on rectangular channel) for all the values of the parameters under consideration. The other two graphs compare the SCP_{inst} of all the geometries for the lowest and the highest value of the range of the parameter under consideration.

In Figure 3.7, the temporal evolution of SCP_{inst} is shown for GEOM-A and GEOM-D, for SVF values of 20, 30, 40, 50 and 60 %. Figure 3.8 shows the SCP_{inst} temporal evolution for all geometries, for SVF=20 % and SVF=60 %. As it can be observed, all cases exhibit an SCP_{inst} of approximately 1240 W/kg_s at the beginning of the adsorption phase. Subsequently, the SCP_{inst} drops drastically for lower SVF values, while the decrease for higher SVF values is smoother. The adsorption rate is similar for all geometries at the beginning. The temperature inside the reactor increases as a result of the exothermic nature of adsorption. For low SVF, the ineffectiveness of the heat exchanger to remove the released adsorption heat results in a higher temperature inside the reactor. As a result, the adsorption capacity and the adsorption rate drop. On the contrary, for high SVF, the heat transfer is more effective and the reactor temperature is maintained low. Consequently the SCP_{inst} decrease is smoother. With respect to Figure 3.8a, as already commented in 3.3.6.1, at low SVF the performance of the reactor appears to be geometry-independent. However, it is also observed that at the most transient part, the SCP_{inst} may differ by more than 100 W/kg_s.

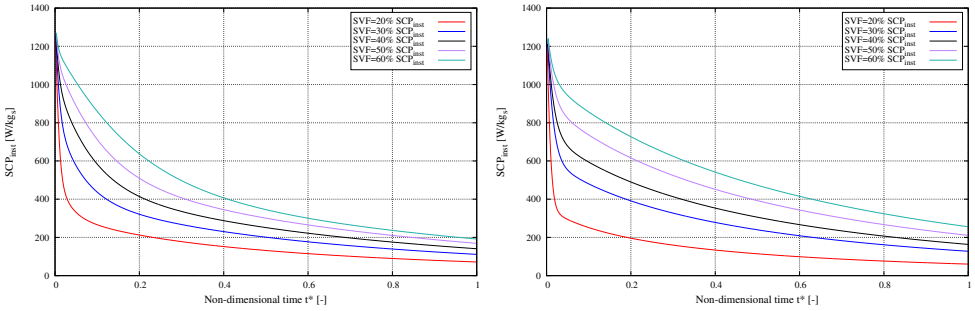

(a) GEOM-A (b) GEOM-D

Figure 3.7: SCP_{inst} evolution for all SVF for (a) GEOM-A and (b) GEOM-D

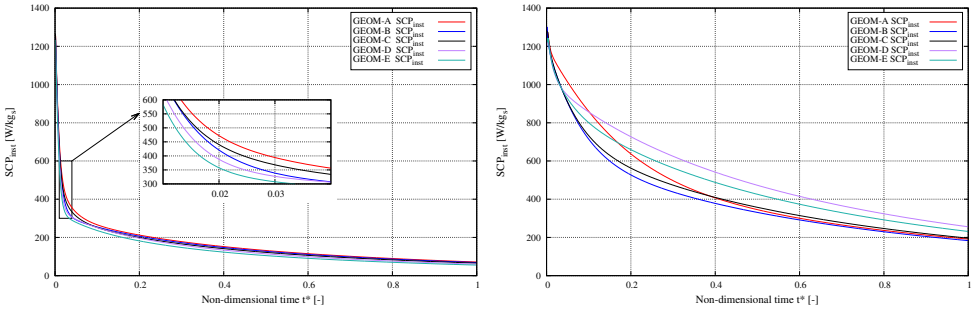

(a) SVF=20 % (b) SVF=60 %

Figure 3.8: SCP_{inst} evolution for all geometries for (a) SVF=20 % and (b) SVF=60 %

In Figure 3.9, the temporal evolution of SCP_{inst} is shown for GEOM-C and GEOM-E, for fin length of 5, 10, 20, 30 and 40 mm. Figure 3.10 shows the SCP_{inst} temporal evolution for all geometries, for $\gamma = 5$ mm and $\gamma = 40$ mm. The effect of less effective cooling of the reactor – and thus, drastic decrease of SCP_{inst} – is observed at higher fin length. At low γ, the temporal evolution of SCP_{inst} is nearly geometry-independent. At high γ, the performance of the geometries that are based in rectangular channel is superior. It is observed that, although the initial SCP_{inst} is lower for rectangular channel geometries, it does not decrease as drastically as the rest geometries. At t*=1, the SCP_{inst} for the rectangular channel geometries is significantly higher than for the circular channel geometries (almost triple for GEOM-E and quadruple for GEOM-D).

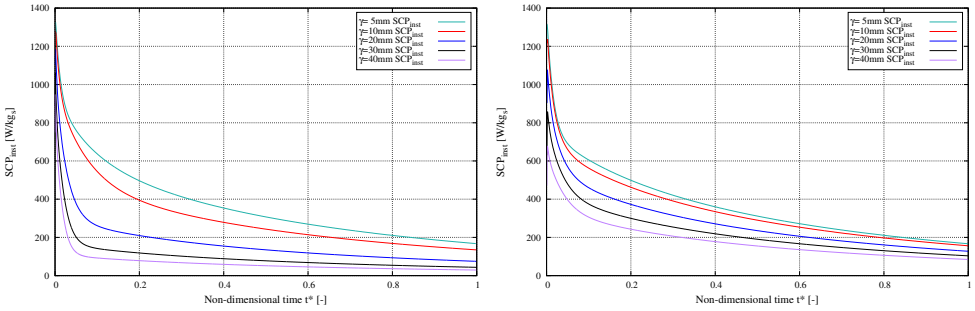

(a) GEOM-C (b) GEOM-E

Figure 3.9: SCP_{inst} evolution for all γ for (a) GEOM-C and (b) GEOM-E

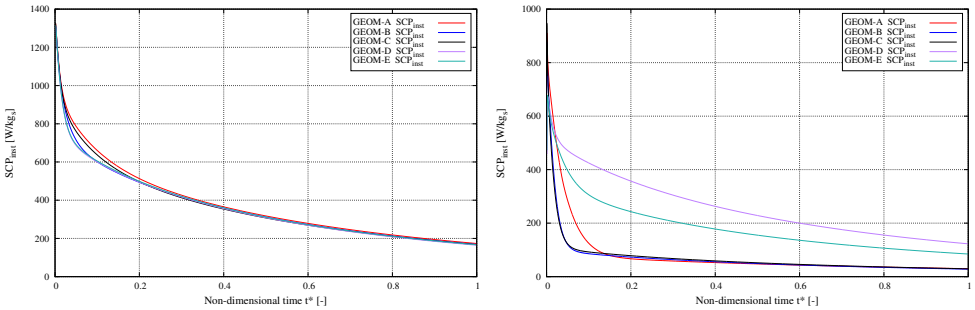

(a) $\gamma = 5\,\text{mm}$ (b) $\gamma = 40\,\text{mm}$

Figure 3.10: SCP_{inst} evolution for all geometries for (a) $\gamma = 5\,\text{mm}$ and (b) $\gamma = 40\,\text{mm}$

In Figure 3.11, the temporal evolution of SCP_{inst} is shown for GEOM-B and GEOM-D, for fin thickness of 0.5, 1, 2, 3 and 4 mm. Figure 3.12 shows the SCP_{inst} temporal evolution for all geometries, for $\delta = 0.5\,\text{mm}$ and $\delta = 40\,\text{mm}$. As in the previous cases, the ineffective cooling of the reactor – which corresponds at higher fin thickness – results in a drastic decrease of the SCP_{inst}, whereas the lowest δ exhibits the most smooth decrease of SCP_{inst}. At the highest δ, the performance of the reactor becomes nearly geometry-independent. It is also observed, that the geometries based on rectangular channel perform relatively better in comparison to those based on circular channel, at lower fin thickness.

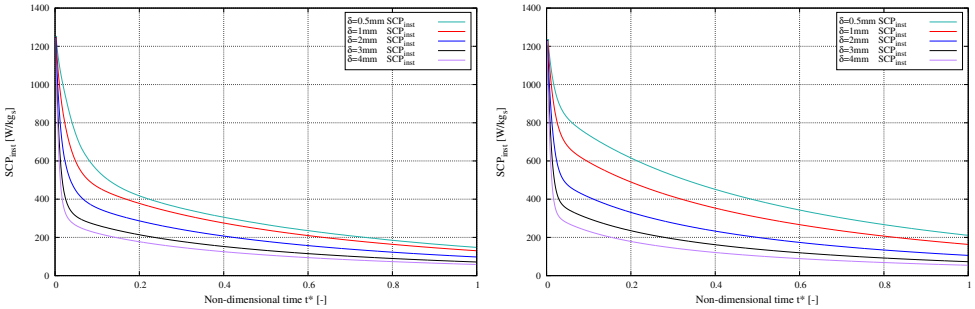

(a) GEOM-B (b) GEOM-D

Figure 3.11: SCP_{inst} evolution for all δ for (a) GEOM-B and (b) GEOM-D

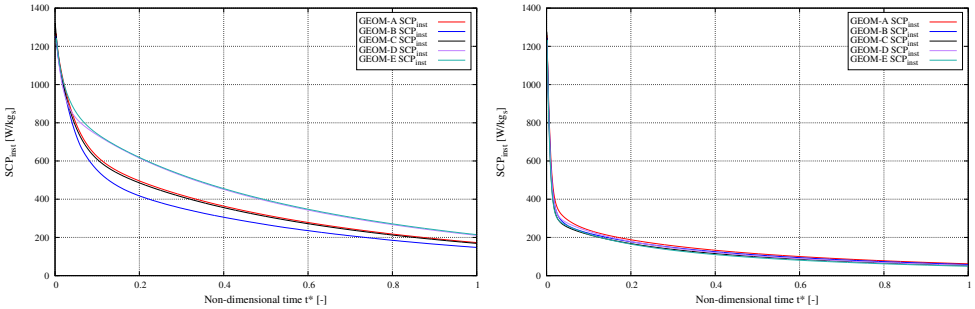

(a) $\delta = 0.5\,\text{mm}$ (b) $\delta = 4\,\text{mm}$

Figure 3.12: SCP_{inst} evolution for all geometries for (a) $\delta = 0.5\,\text{mm}$ and (b) $\delta = 4\,\text{mm}$

3.3.6.3 Heat exchanger material

The results presented in the previous sections consider copper as the heat exchanger material. The simulations were repeated for aluminium, in order to observe its influence on the performance of the system. The relevant properties of the two materials differ significantly ($\rho_{Al} = 0.3 \times \rho_{Cu}$, $c_{p_{Al}} = 2.3 \times c_{p_{Cu}}$ and $\lambda_{Al} = 0.6 \times \lambda_{Cu}$). The density, the specific heat capacity and the thermal conductivity of the materials are presented in Table 3.2. It appears that using aluminium heat exchangers results to slightly lower SCP_{ads} and higher $t_{70\,\%}$, since due to its lower thermal conductivity the packed bed is cooled down less effectively. However this difference is not significant.

The decrease observed in SCP_{ads} when using aluminium instead of copper does not exceed 1 %, for the studied range of SVF and fin thickness. The decrease is higher than 1 % only at higher values of fin length, $\gamma > 30$ mm, with a maximum of 3.03 % reduction for fin length $\gamma = 40$ mm of GEOM-A.

3.3.6.4 Coefficient of Performance

As explained earlier, this study focused on the Specific Cooling Power of the adsorption phase. The evaluation of the Coefficient of Performance is scheduled as the next stage of this study, since this task requires considerably longer computations. Nevertheless, this task has been completed for all geometries with SVF = 40 % and SVF = 50 % ($\gamma = 10$ mm and $\delta = 1$ mm).

Therefore, it is considered interesting to cite here the COP results and comment them briefly. The methodology for this study is detailed in Section 3.4. The results show that the choice of comparing the different geometries based on their Solid Volume Fraction is indeed relevant. The COP of the five geometries – which share the same SVF – is virtually the same. For SVF = 40 %, the COP is within 0.503 ± 0.003, while for SVF = 50 % the COP is within 0.436 ± 0.003.

During desorption, the reactor is heated by the HTF. This thermal energy input is distributed to (i) the increase of the heat exchanger solid temperature (ii) the temperature increase of the adsorbent and adsorbate and (iii) provide the endothermic thermal energy required for desorption. The latter two components do not depend considerably on the geometry – in the sense that, if the changes in the adsorbed mass and the temperature are the same, then the required energy per kg of adsorbent will be the same across the five geometries. In geometries with the same SVF, their solid volume is the same with respect to the entire volume of the reactor. By consequence, the mass of the heat exchanger solid is the same, when normalized per kg of adsorbent. Therefore by keeping constant the SVF across geometries, the component (i) is kept constant. Therefore, the thermal energy input $Q_{heating}$ is nearly constant across different geometries. Moreover, since the numerator of COP, $Q_{cooling}$, is fixed by the $t_{70\%}$, then the COP will be nearly the same across geometries of the same SVF.

Since for the same SVF, a similar COP is expected across geometries, the presented results evaluate how effective is the geometric distribution of the heat exchanger solid and the packed bed – namely, the reactor design – in order to effectively cool down the reactor during adsorption and improve the Specific Cooling Power.

3.4 SCP and COP of the hexagonal honeycomb adsorption reactor

The study presented in this section is dedicated to the numerical investigation of the hexagonal honeycomb adsorption reactor. As already commented in the literature review – to the author's knowledge – this geometry has not been studied thoroughly hitherto.

A parametric study with respect to geometric and operational parameters is presented. In the context of this study, the Specific Cooling Power and the Coefficient of Performance are quantified.

3.4.1 Geometrical considerations for the simulated geometry

The geometry under investigation in this study is the hexagonal honeycomb adsorption reactor. Figure 3.13 illustrates a front view and a three-dimensional view of the reactor, as well as a cross-section of the vertical plane. The heat transfer fluid passes through a vertical rectangular channel. Metallic hexagonal honeycomb structures are embedded on two of the plates which form the aforementioned rectangular channel. The adsorbent is placed inside the hexagonal cells. This module is enclosed within the vapor chamber, where vapor resides. The vapor flowing from or to the evaporator and the condenser passes through the vapor chamber. One or more modules can be incorporated within the vapor chamber.

Detailed distributed-parameter models have considerable computational consumption. Therefore, simulating the entire reactor would result to unpractical computational costs. Thus, it is a common practice to reduce the computational domain, taking into advantage the symmetries and the periodicities exhibited by the geometry under consideration. This is achieved through the assumptions (iv) and (v), presented in Section 2.3. These hypotheses allow to interpret the results of the reduced geometry as representative for the entire reactor. All honeycomb cells are expected to have the same behavior if the HTF temperature is constant across the rectangular channel of the reactor, as well as if the reactor is ideally insulated. Moreover, geometric symmetry of the hexagon allows to simulate only one sixth of the cell.

Figure 3.14 and 3.15 illustrate the computational domain of the reduced geometry and its boundary conditions, respectively. The mathematical formulation of the latter was presented in Section 2.3.3.

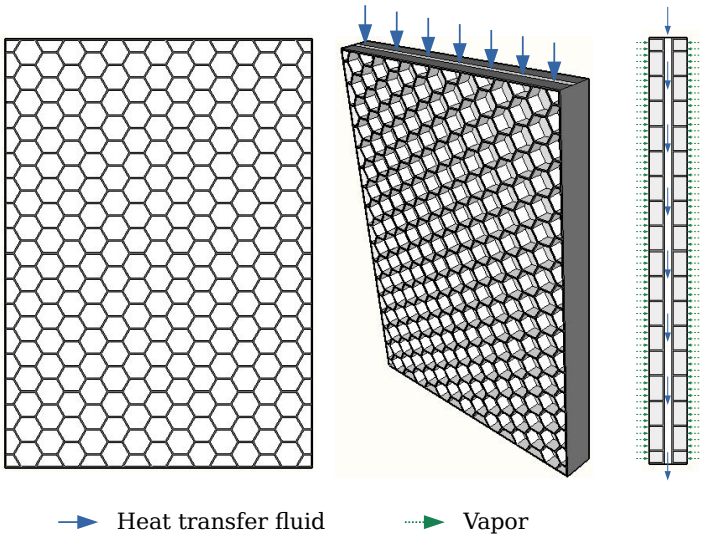

Figure 3.13: Front view, three-dimensional view and vertical cross-section of the hexagonal honeycomb adsorption reactor

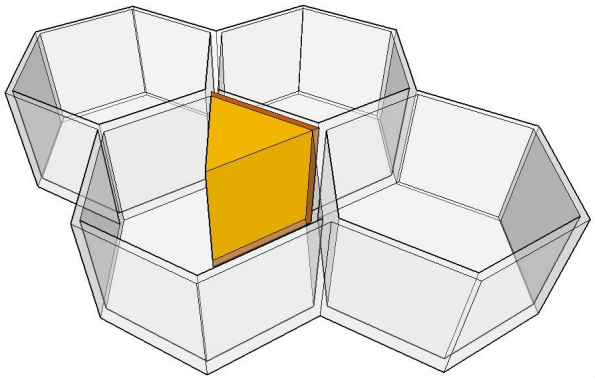

Figure 3.14: Computational domain of the reduced geometry

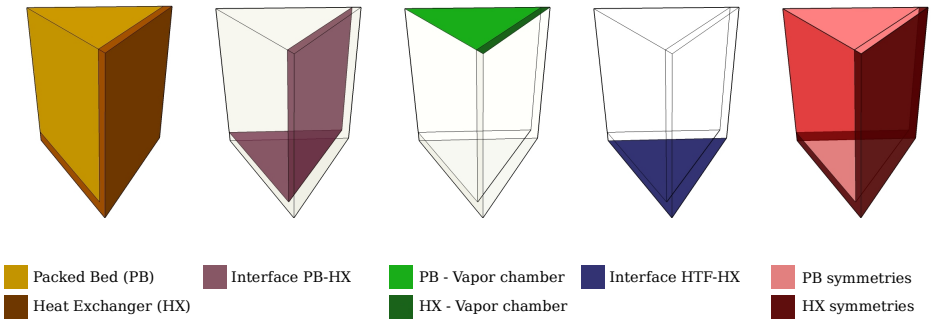

Figure 3.15: Boundary conditions of the computational domain

The required dimensions for the definition of the hexagonal honeycomb geometry are depicted in Figure 3.16. The dimension denoted as α corresponds to the thickness of the metallic plate and it is considered as 1 mm. The three dimensions which define the geometry are the cell inradius β, the cell height γ and the fin thickness δ.

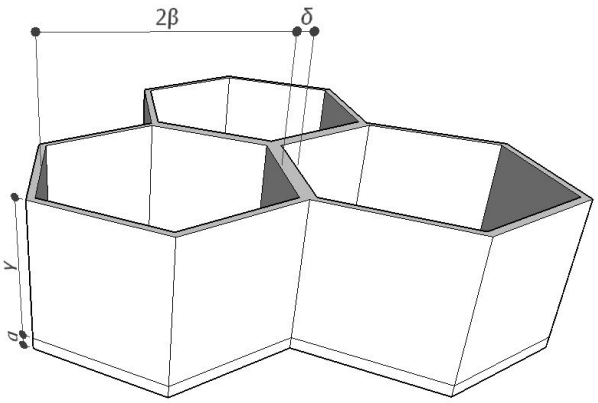

Figure 3.16: Dimensions of the geometry

3.4.2 Simulation details

The entire thermodynamic cycle is simulated, namely the four phases (a) pre-cooling, (b) adsorption, (c) pre-heating and (d) desorption. The cycle simulation is repeated until cyclic behavior is attained. From the simulations, it arose that three cycles are sufficient in order to achieve cyclic steady state and eliminate the influence of the initial conditions. With respect to each phase duration, the scheme presented below was considered. It should be noted that this scheme is appropriate for the design stage, in order to determine the required duration for each phase. In real applications, predetermined phase durations are imposed, according to the values that arise from the design process. This scheme is used in all the presented simulations except Section 3.4.6.5, where predetermined phase durations are considered.

The pre-cooling phase is terminated when the maximum pressure inside the reactor becomes lower than the evaporator pressure. This assures that once the reactor and the evaporator are connected, the vapor flow direction is from the evaporator towards the reactor. The opposite would result in vapor flow from the reactor to the evaporator, where the vapor would condense. The latter is counterproductive for the cooling production since condensation is exothermic. The duration of pre-cooling phase is represented by t_{pc}.

The adsorption phase duration t_{ad} is defined by the adsorbed mass with respect to the theoretical adsorption capacity that would result if equilibrium is achieved. As mentioned earlier, the adsorption rate decreases significantly while approaching equilibrium and therefore, it is of no practical interest to continue the adsorption phase until equilibrium is achieved. The minimum theoretical capacity of the cycle w^*_{min} corresponds to (P_{con}, T_{des}), while the maximum w^*_{max} corresponds to (P_{eva}, T_{ads}). The adsorbed mass across the domain of the packed bed is averaged $\overline{w}$, and its relative value with respect to the difference $(w^*_{\mathrm{max}} - w^*_{\mathrm{min}})$ is calculated based on equation 3.4. The cycle adsorption percentage is the $\overline{w}_{\mathrm{rel}}$ that determines the duration of the adsorption phase. It is set to 70 % for all the simulations, except in Section 3.4.6.3, where a parametric study of this value is presented.

$$\overline{w}_{\mathrm{rel}} = \frac{\overline{w} - w^*_{\mathrm{min}}}{w^*_{\mathrm{max}} - w^*_{\mathrm{min}}} \times 100\% \tag{3.4}$$

Similarly to the pre-cooling phase, the pre-heating phase duration t_{ph} is terminated

when the minimum pressure across the packed bed domain is higher than the condenser pressure. The desorption phase duration t_{de} is calculated as in equation 3.5, in order to balance the half cycle time t_{half}.

$$t_{de} = t_{pc} + t_{ad} - t_{ph} \tag{3.5}$$

Table 3.2 summarizes all the input parameters of the model. Copper is considered as the heat exchanger solid for all the presented results. In Section 3.4.6.4, the base case is simulated with aluminium as heat exchanger solid, and the results are discussed.

3.4.3 Base scenario and studied range for the parametric study

For the parametric study, a base scenario is defined with respect to the geometrical and the operational parameters. Henceforth, each of the parameters under investigation is varied, in order to evaluate its influence on the performance indicators presented in Section 3.4.4. Table 3.3 summarizes the geometrical and operational parameters under investigation. It presents the base scenario values and the studied ranges.

Table 3.3: Base scenario values and studied range for the geometrical and operational parameters under investigation

Geometrical parameters		Base	Range	Unit
Cell inradius	β	3	1-6	mm
Cell height	γ	10	5-30	mm
Fin thickness	δ	1	0.5-3	mm
Operational parameters		**Base**	**Range**	**Unit**
Adsorption temperature	T_{ads}	30	20-40	°C
Desorption temperature	T_{des}	80	60-90	°C
Evaporator temperature	T_{eva}	10	5-15	°C
Condenser temperature	T_{con}	30	20-40	°C
Convection heat transfer coefficient	U_{HTF}	1000	600-2000	$Wm^{-2}K^{-1}$
Cycle adsorption percentage (equation 3.4)	$\overline{w}_{rel}$	70	50-90	%

3.4.4 Performance indicators

The performance indicators used for the evaluation of the reactor performance are the Coefficient of Performance (COP) and the cyclic average Specific Cooling Power (SCP). Furthermore, the cycle duration is reported, since it is adapted on each case.

The COP is a non-dimensional parameter comparing the cooling production to the energy consumption for the operation of the adsorption cooling system.

$$\mathrm{COP} = \frac{Q_{\mathrm{cooling}}}{Q_{\mathrm{heating}}} \tag{3.6}$$

where Q_{cooling} and Q_{heating} are measured in Joules. The useful cooling produced Q_{cooling} is calculated as the product of the adsorbed mass and the latent heat of evaporation of the refrigerant, while Q_{heating} is the thermal energy input at T_{high} during pre-heating and desorption phases.

The SCP is the average cooling power normalized per unit of mass of adsorbent and it is measured in Wkg^{-1}. The average cooling power is the overall useful cooling energy produced throughout the adsorption phase, divided by t_{cycle}. The SCP is calculated as:

$$\mathrm{SCP} = \frac{Q_{\mathrm{cooling}}}{M_s \times t_{\mathrm{cycle}}} = \frac{\Delta m \times \Delta H'_{\mathrm{evap}}}{M_s \times t_{\mathrm{cycle}}} = \frac{\Delta w \times \Delta H'_{\mathrm{evap}}}{t_{\mathrm{cycle}}} \tag{3.7}$$

where Δm is the total mass adsorbed during the adsorption phase and desorbed during the desorption phase, M_s is the dry solid adsorbent mass and Δw is the quotient of the two aforementioned values. The cooling produced associated with Δw is denoted as $\Delta H'_{\mathrm{evap}}$ and it is calculated as:

$$\Delta H'_{\mathrm{evap}} = h_{\mathrm{v,sat}}\big|_{T_{\mathrm{eva}}} - h_{\mathrm{l,sat}}\big|_{T_{\mathrm{con}}} \tag{3.8}$$

where $h_{\mathrm{v,sat}}\big|_{T_{\mathrm{eva}}}$ is the enthalpy of the saturated vapor refrigerant at T_{eva} and $h_{\mathrm{l,sat}}\big|_{T_{\mathrm{con}}}$ is the enthalpy of the saturated liquid refrigerant leaving the condenser, and thus, the enthalpy of the vapor-liquid mixture entering the evaporator (assuming isenthalpic expansion).

3.4.5 Results interpretation

For each parameter under investigation, the reported performance indicators for the reactor performance are the COP and SCP, as presented in Section 3.4.4. Furthermore, since the cycle duration is adapted according to each case, it is also reported. For sake of conciseness, the COP, the SCP and the cycle duration t_{cycle} are reported in one graph. To achieve this, three vertical axes are incorporated in each graph. Each vertical axis is colored as its corresponding curve. The curve and vertical axis are red for the SCP, blue for COP and green for t_{cycle}. For colorless interpretation, the label of each axis indicates the point symbol used in the corresponding curve. The point symbols are circle for SCP, square for COP and triangle for t_{cycle}.

For the three geometric parameters under investigation, spatial distribution of the adsorbed mass w_{rel} and the temperature are reported at 100 s after the beginning of the adsorption phase. The two-dimensional distributions pertain to the cross-section of the cell. Regarding the heat exchanger solid, w_{rel} does not apply, while temperature variations are visually imperceptible by the used scale, due to higher thermal conductivity.

3.4.6 Results

This section presents the results that arose from the simulations, focusing the discussion on the physical phenomena involved and the quantification of the reactor performance.

3.4.6.1 Geometrical parameters

Figure 3.17 presents the reactor performance results for cell inradius in the range of 1-6mm. Within the studied range, considerable variations are observed for both SCP and COP. On the one hand, the SCP decreases as the cell inradius increases, ranging between 80.4 W/kg and 218.9 W/kg for cell inradius of 6 and 1 mm, respectively. Lower inradius results in a more effective cooling of the packed bed. As observed in Figure 3.18, the temperature is maintained lower during the adsorption phase and therefore the adsorbed mass is higher, leading to a higher rate of cooling production. On the other hand, the COP increases as the cell inradius increases, ranging between

0.356 and 0.606 for cell inradius of 1 and 6 mm, respectively. Lower cell inradius results in more densely packed cells, and consequently, to a higher Solid Volume Fraction (SVF), the percentage of the heat exchanger solid volume with respect to the entire reactor volume. The SVF for $\beta = 1$ mm is 59.6% while for $\beta = 6$ mm is 22.5%. As commented earlier, the additional heat exchanger solid mass is associated to higher thermal input and thus, lower COP.

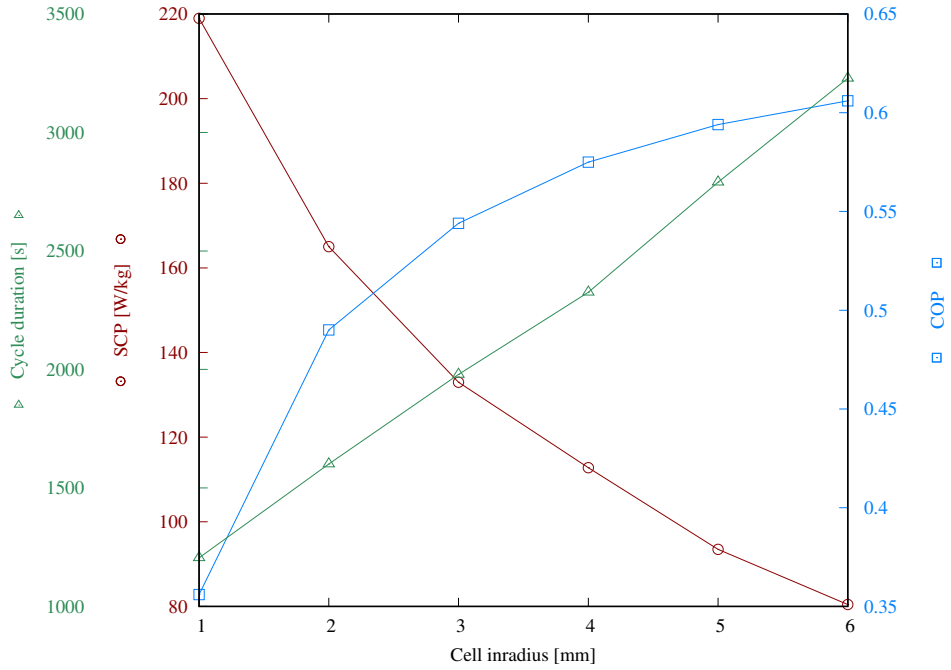

Figure 3.17: Reactor performance based on the cell inradius

Figure 3.19 illustrates the reactor performance for cell height in the range of 5-30 mm. Within the studied range, the SCP halves approximately, though the COP does not experience such a drastic variation. The SCP decreases as the cell height increases, from 159.5 W/kg for $\gamma = 5$ mm to 86.1 W/kg for $\gamma = 30$ mm. As observed from Figure 3.20, the packed bed is cooled more effectively for lower cell height. For increasing cell heights, the released energy due to the exothermic nature of adsorption is removed less effectively, leading to higher temperatures and thus, lower adsorption capacity and cooling production. The COP increases from 0.51 for $\gamma = 5$ mm to 0.57

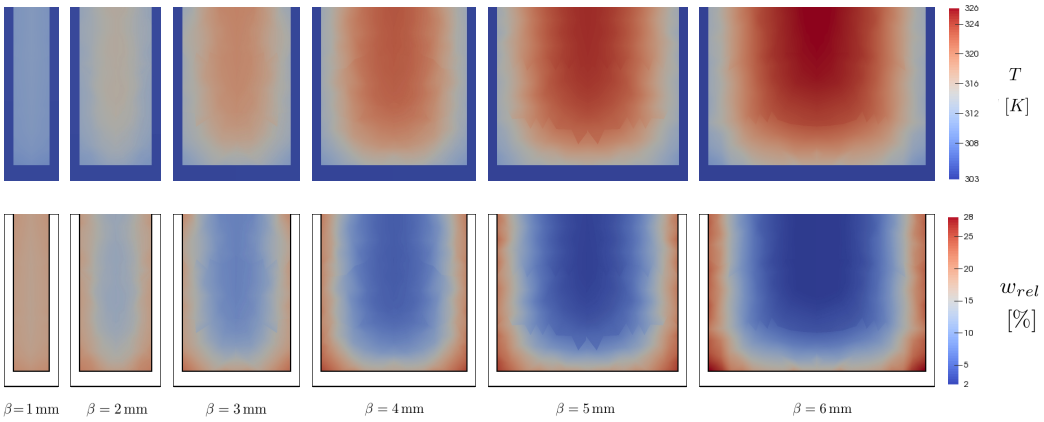

Figure 3.18: Spatial distribution of temperature (top) and relative adsorbed mass (bottom) at t=100s of adsorption phase for various cell inradii

for $\gamma = 30\,\text{mm}$. The COP variation is not so significant since the SVF does not vary considerably, being 38.3% for $\gamma = 5\,\text{mm}$ and 28.9% for $\gamma = 30\,\text{mm}$.

Figure 3.21 shows the reactor performance for fin thickness in the range of 0.5-3 mm. The inverse effect is observed in comparison to the cell height case, namely, COP exhibits considerable variations, whereas SCP does not. In particular, SCP varies between 127.6 W/kg and 140.5 W/kg, corresponding to fin thickness of 0.5 and 3 mm, respectively. As observed in Figure 3.22, the temperature distribution of the packed bed is similar across the studied fin thicknesses. Consequently, the adsorption rate and the cooling production follow the same trend. However, at higher fin thicknesses the reactor is burdened with more heat exchanger solid, with the SVF being 22.5% and 59.6% for $\delta = 0.5\,\text{mm}$ and $\delta = 3\,\text{mm}$, respectively. This considerable increase of the SVF results in a significant decrease of COP, from 0.599 for $\delta = 0.5\,\text{mm}$ to 0.364 for $\delta = 3\,\text{mm}$.

3.4.6.2 Operating temperatures

This section elaborates the influence of the operating temperatures on the reactor performance. These temperatures are T_{des}, T_{ads}, T_{eva} and T_{con}. The latter two determine the evaporator pressure P_{eva} and the condenser pressure P_{con}, respectively.

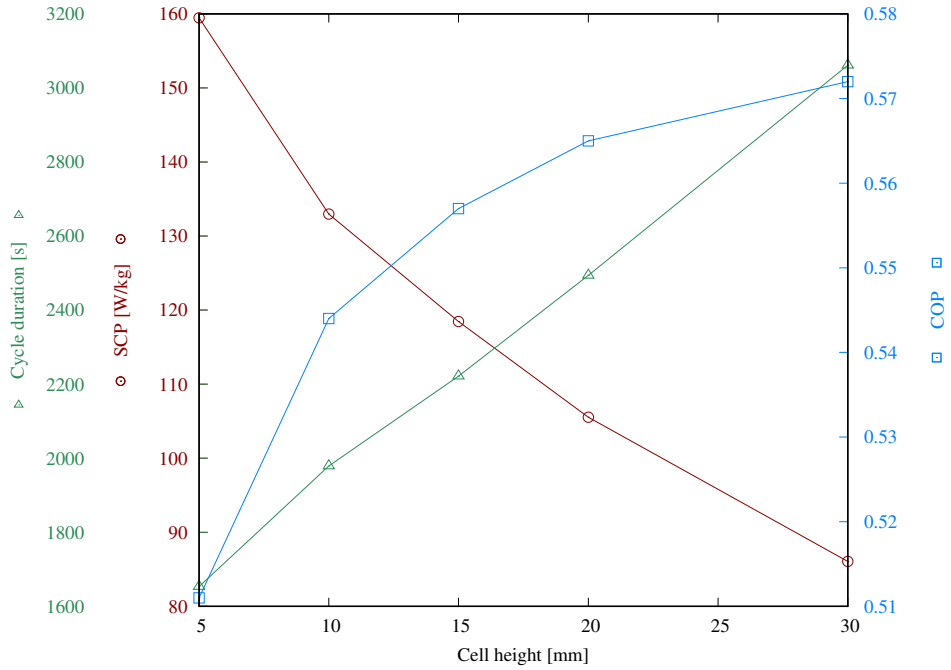

Figure 3.19: Reactor performance based on the cell height

Firstly, the quantitative results are presented graphically and the observed tendencies are commented briefly. Subsequently, a discussion is presented with the objective to facilitate the interpretation of the quantitative results. Through this discussion, it is attempted to provide an insight to the underlying physical phenomena involved.

Figure 3.23 illustrates the reactor performance based on the adsorption temperature T_{ads}, the HTF temperature during the pre-cooling and adsorption phases. As it can be observed, both performance indicators decrease as the T_{ads} increases. The SCP decreases from 166.3 W/kg for $T_{\text{ads}} = 20\,^{\circ}\text{C}$ to 86.4 W/kg for $T_{\text{ads}} = 40\,^{\circ}\text{C}$. The COP decreases from 0.645 for $T_{\text{ads}} = 20\,^{\circ}\text{C}$ to 0.395 for $T_{\text{ads}} = 40\,^{\circ}\text{C}$.

Figure 3.24 shows the reactor performance based on the desorption temperature T_{des}, the HTF temperature during the pre-heating and desorption phases. The temperature range under consideration is 60 - 90 °C. The SCP is significantly influenced by the T_{des}, which almost triples within the range under consideration, from 53.6 W/kg for

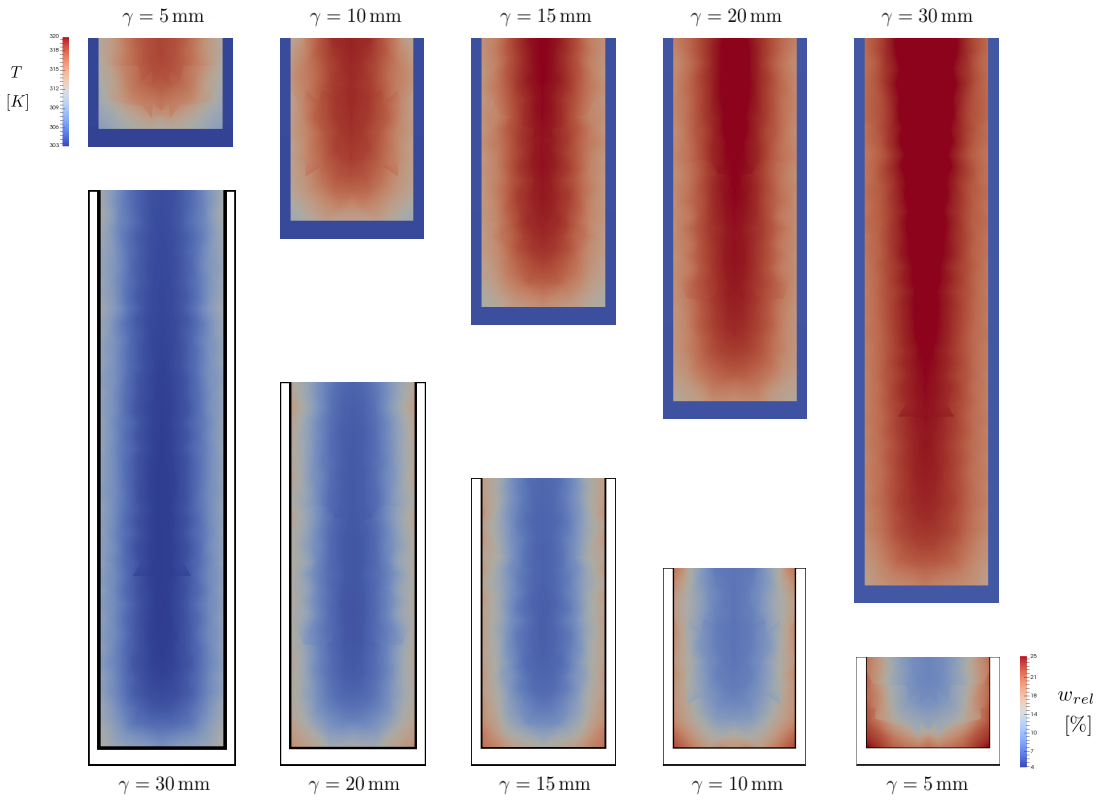

Figure 3.20: Spatial distribution of temperature (top) and relative adsorbed mass (bottom) at t=100s of adsorption phase for various cell heights

$T_{\text{des}} = 60\,°\text{C}$ to 153.8 W/kg for $T_{\text{des}} = 90\,°\text{C}$. With respect to the COP, it is observed that in the range 70-90 °C it is only slightly affected by T_{des} – taking values between 0.531 and 0.544 – whereas at lower T_{des} it presents a sudden decrease until 0.47 for $T_{\text{des}} = 60\,°\text{C}$. Although not plotted in Figure 3.24, the simulation was also performed for T_{des} of 52 °C and 55 °C. The corresponding SCP and COP are 25.3 W/kg and 0.356 for $T_{\text{des}} = 55\,°\text{C}$, while for $T_{\text{des}} = 52\,°\text{C}$, the SCP and the COP are 6.6 W/kg y 0.154. The ability of the system to perform with so low driving temperature is an advantageous feature of adsorption cooling technology (discussed in Section 3.5).

Figure 3.25 illustrates the reactor performance as a function of the evaporator tem-

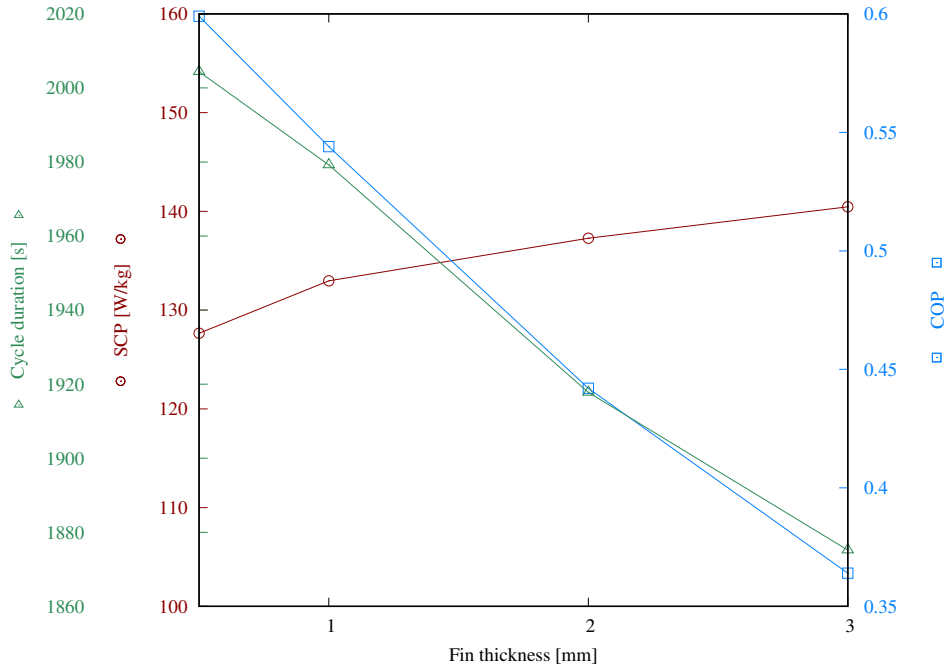

Figure 3.21: Reactor performance based on the fin thickness

perature T_{eva}. As it arises from the results, the reactor performance improves as the T_{eva} increases. In particular, the SCP increases from 95.4 W/kg for $T_{eva} = 5\,°C$ to 168.8 W/kg for $T_{eva} = 15\,°C$. The COP increases from 0.442 for $T_{eva} = 5\,°C$ to 0.624 for $T_{eva} = 15\,°C$. Lastly, Figure 3.26 presents the results for the reactor performance based on the condenser temperature T_{con}. As it can be observed, both the SCP and the COP decrease as the T_{con} increases. The SCP decrease from 162.6 W/kg for $T_{con} = 20\,°C$ to 93.1 W/kg for $T_{con} = 40\,°C$, while the COP decreases from 0.588 for $T_{con} = 20\,°C$ to 0.47 for $T_{con} = 40\,°C$.

In order to gain insight to the underlying physical mechanisms of the system, it is important to elaborate the impact of each of these parameters on the adsorption equilibrium, adsorption kinetics, heat transfer and thermodynamics involved in the system.

Recalling equation 3.4, altering T_{des} or P_{con} alters the theoretical minimum adsorption

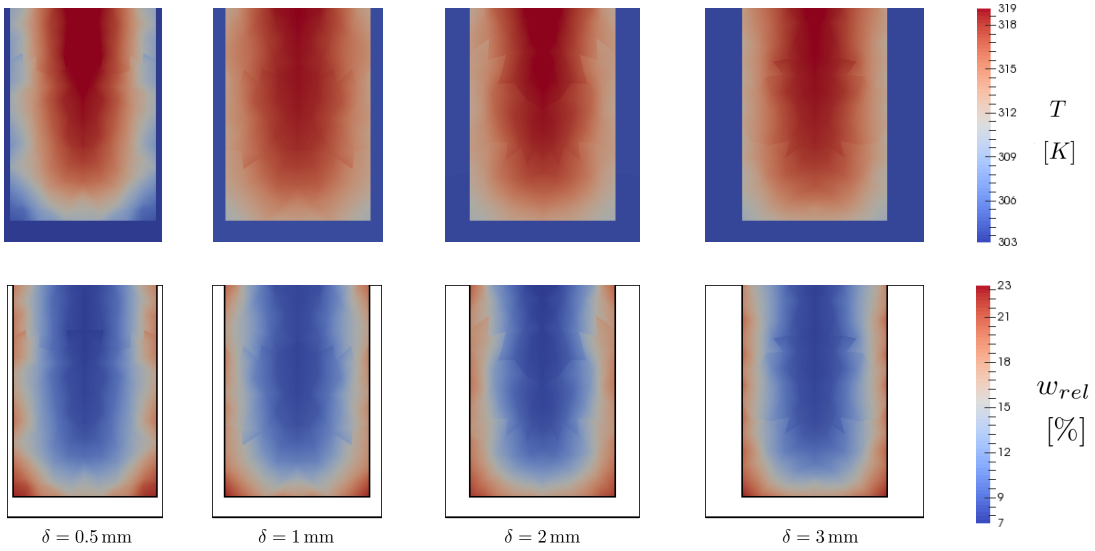

Figure 3.22: Spatial distribution of temperature (top) and relative adsorbed mass (bottom) at t=100s of adsorption phase for various fin thicknesses

equilibrium capacity of the cycle w^*_{min}. Similarly, altering T_{ads} or P_{eva} alters the theoretical maximum adsorption equilibrium capacity of the cycle w^*_{max}. Henceforth, the difference of the theoretical equilibrium capacities ($w^*_{\mathrm{max}} - w^*_{\mathrm{min}}$) will be referred to as $\Delta w^*_{\mathrm{cycle}}$. The $\Delta w^*_{\mathrm{cycle}}$ influences both the adsorption equilibria and the adsorption kinetics. Regarding the equilibria, higher $\Delta w^*_{\mathrm{cycle}}$ allows more vapor to be adsorbed per unit of mass of adsorbent in each cycle. Consequently, the vapor evaporated and the associated cooling produced Q_{cooling} are higher. This quantity is present in the numerator of both the SCP and the COP. Therefore, a higher $\Delta w^*_{\mathrm{cycle}}$ benefits both performance indicators of the reactor. Higher $\Delta w^*_{\mathrm{cycle}}$ is achieved at (i) lower T_{ads}, since the w^*_{max} increases, (ii) higher T_{des}, since the w^*_{min} decreases, (iii) higher T_{eva}, since the w^*_{max} increases for higher P_{eva}, and (iv) lower T_{con}, since the w^*_{min} decreases for lower P_{con}.

The influence of $\Delta w^*_{\mathrm{cycle}}$ on the adsorption kinetics is evident in equation 2.2. As expressed by the LDF model, the adsorption rate is proportional to the difference $(w^* - w)$. Therefore, when $\Delta w^*_{\mathrm{cycle}}$ is higher – apart from the higher potential Q_{cooling} – the rate of cooling production is higher as well, thus the SCP is benefited.

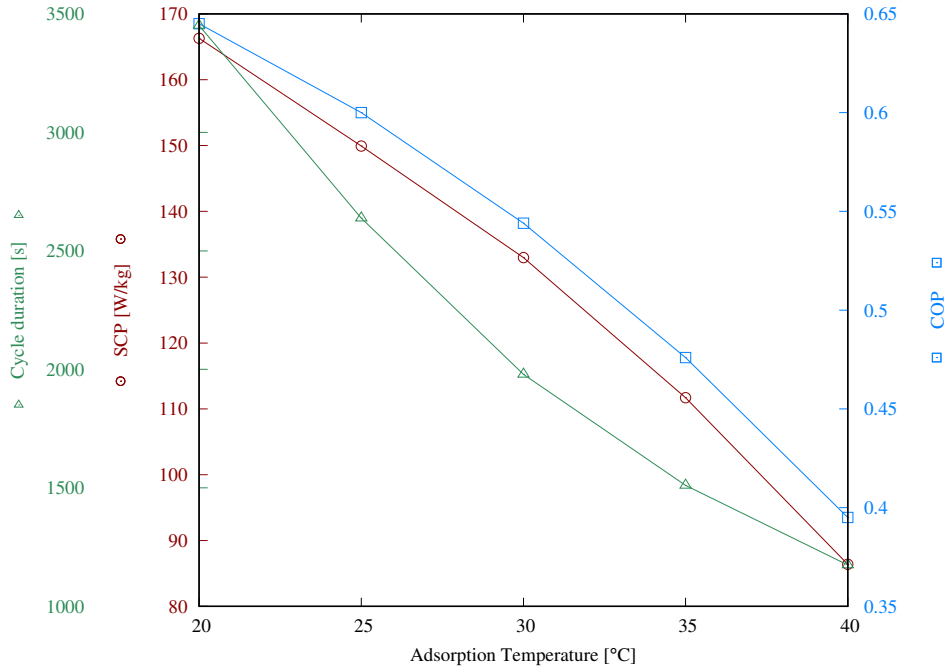

Figure 3.23: Reactor performance based on the adsorption temperature

Furthermore, the adsorption kinetics are also influenced by the temperature dependence of the effective diffusivity, as expressed by the Arrhenius relation (equation 2.3). At higher temperature, the effective diffusivity increases, and thus, the sorption rate increases. With respect to T_{ads}, the effective diffusivity for $T_{ads} = 40\,°C$ is approximately three times higher than for $T_{ads} = 20\,°C$. However, although the effective diffusivity increases at higher T_{ads}, the SCP still decreases, because the importance of decreasing Δw^*_{cycle} at higher T_{ads} is more prevalent. For the case of T_{des}, the effective diffusivity for $T_{des} = 90\,°C$ is approximately 3.5 higher than for $T_{des} = 60\,°C$. Higher desorption rate allows to desorb more effectively the water vapor and thus, to exploit at larger extent the Δw^*_{cycle}.

Although a subtle influence, it is worth mentioning that T_{eva} and T_{con} influence the thermodynamics of the system, in the sense that they alter the $\Delta H'_{evap}$ (calculated in equation 3.8). The T_{eva} determines the enthalpy of the saturated vapor leaving the

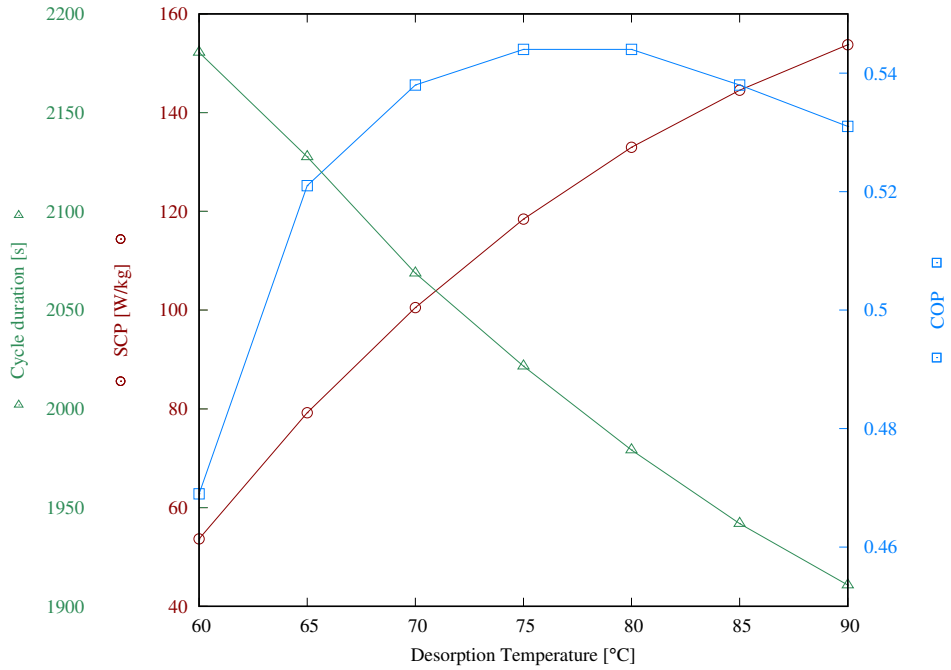

Figure 3.24: Reactor performance based on the desorption temperature

evaporator $h_{\mathrm{v,sat}}\big|_{T_{\mathrm{eva}}}$, while the T_{con} determines the enthalpy of the saturated liquid leaving the condenser $h_{\mathrm{l,sat}}\big|_{T_{\mathrm{con}}}$, which is the enthalpy of the vapor-liquid mixture entering the evaporator, assuming isenthalpic expansion. In other words, at higher T_{eva} and lower T_{con}, the vapor adsorbed by the reactor is associated to higher cooling production. This effect is more notable for T_{con}, where the $\Delta H'_{\mathrm{evap}}$ for $T_{\mathrm{con}} = 20\,^{\circ}\mathrm{C}$ is 3.6% higher than for $T_{\mathrm{con}} = 40\,^{\circ}\mathrm{C}$ (for $T_{\mathrm{eva}} = 10\,^{\circ}\mathrm{C}$), whereas the $\Delta H'_{\mathrm{evap}}$ for $T_{\mathrm{eva}} = 15\,^{\circ}\mathrm{C}$ is only 0.8% higher than for $T_{\mathrm{eva}} = 5\,^{\circ}\mathrm{C}$ (for $T_{\mathrm{con}} = 30\,^{\circ}\mathrm{C}$).

So far, the influence of $\Delta w^*_{\mathrm{cycle}}$ value has been elaborated. However, another aspect that influences the COP is related with the values of w^*_{min} and w^*_{max}. To illustrate this, a simple example is employed, considering two cases A and B with the same $\Delta w^*_{\mathrm{cycle}}$. The two cases are differentiated by the limits of $\overline{w}$, which are lower for case A; namely, $w^*_{\mathrm{min,A}} < w^*_{\mathrm{min,B}}$ and $w^*_{\mathrm{max,A}} < w^*_{\mathrm{max,B}}$. Even though the two cases have the same $\Delta w^*_{\mathrm{cycle}}$, case B would have lower COP. The denominator of the COP – the

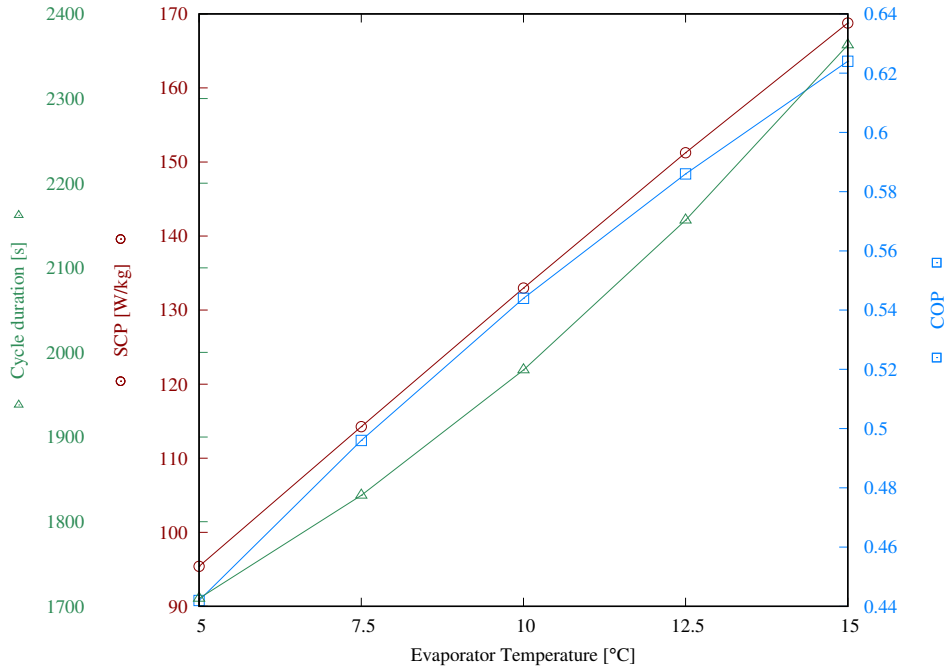

Figure 3.25: Reactor performance based on the evaporator temperature

Q_{heating} provided during the pre-heating and desorption phases – is the amount of thermal energy required to increase the temperature of the reactor from T_{ads} to T_{des}, as well as the thermal energy required for the endothermic desorption. The former part – the sensible heat required for the temperature change – is higher for case B since the thermal mass of the adsorbent is higher, due to its higher adsorbate content. To capture this difference, a comparison between $T_{\text{des}} = 60\,^{\circ}\text{C}$ and $T_{\text{des}} = 90\,^{\circ}\text{C}$ is considered. To compare the two cases, the adsorbed mass is averaged spatially throughout the packed bed domain, as well as it is averaged temporally throughout the desorption phase. This $\left[\frac{1}{t_{\text{de}}}\int_{t_{\text{de}}}\left(\frac{1}{V_{\text{PB}}}\int_{V_{\text{PB}}} w\,dV\right)dt\right]$ will provide an orientative value of the adsorbed mass and its associated thermal mass. For $T_{\text{des}} = 60\,^{\circ}\text{C}$, this value is $0.149\,\text{kg}_\text{w}/\text{kg}_\text{s}$, whereas for $T_{\text{des}} = 90\,^{\circ}\text{C}$ is $0.054\,\text{kg}_\text{w}/\text{kg}_\text{s}$. The corresponding specific heat capacity of the wet adsorbent at these adsorbate contents is $1547\,\text{J}/(\text{kg K})$ and $1149\,\text{J}/(\text{kg K})$, respectively. In other words, at higher level of adsorbed mass, the

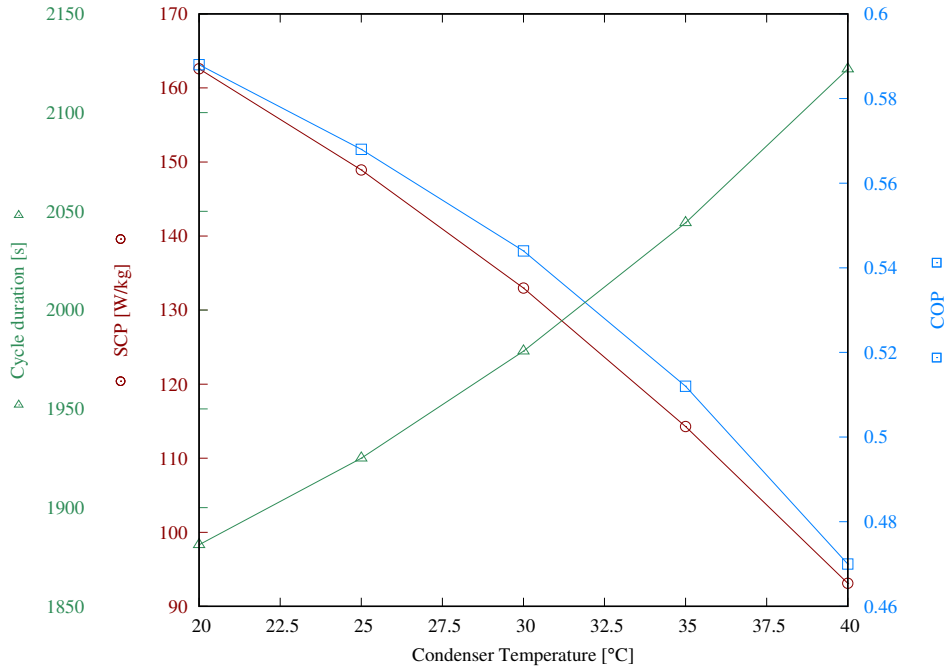

Figure 3.26: Reactor performance based on the condenser temperature

energy required for desorption increases. Since the latter is the denominator of COP, this partially explains the sudden drop of COP for lower T_{des}.

In order to further understand the sudden drop of COP in the lower T_{des}, a discussion is necessary with respect to the adopted cycle scheme (Section 3.4.2). As explained, the simulations begin with a uniform adsorbed mass equivalent to w^*_{min}, corresponding to the equilibrium capacity for P_{con} and T_{des}. The adsorption phase is terminated when the average relative adsorbed mass, $\overline{w}_{\text{rel}}$, becomes 70%. At the end of the desorption phase, the adsorbed mass is expected to decrease anew and approximate w^*_{min}. It is emphasized that – within the finite desorption time – $\overline{w}_{\text{rel}}$ will approximate asymptotically w^*_{min} but it will not reach equilibrium. Hence, the average relative adsorbed mass at the end of desorption phase – henceforth referred to as $\overline{w}_{\text{rel,low}}$ – is expected to be higher than 0 % (which corresponds to the theoretical equilibrium w^*_{min}). Indicatively for the base scenario $\overline{w}_{\text{rel,low}}$ is 0.67 %, while it is lower than 1% for

all the cases presented so far, except the cases of $T_{des} \leq 75\,^{\circ}C$. As the T_{des} decreases, the desorption rate decreases as a result of the combination of two phenomena described above; the decrease of the effective diffusivity and the decrease of Δw^*_{cycle}. Consequently, since the desorption rate decreases significantly, the remaining $\overline{w}_{rel,low}$ at the end of the desorption phase increases, from 1.5% for $T_{des} = 75\,^{\circ}C$ to 8.6% for $T_{des} = 60\,^{\circ}C$. This reduces the $Q_{cooling}$ and thus, it contributes to the overall decrease of COP at low T_{des}. These suggest that for low T_{des}, a different time scheme might be more appropriate. For example, at $T_{des} = 60\,^{\circ}C$ and cycle adsorption percentage $\overline{w}_{rel}$ of 70% (equation 3.4), the COP and the SCP are 0.469 and 53.65 W/kg, respectively. Increasing the cycle adsorption percentage to 75% and 80% increases the COP to 0.496 and 0.512, respectively – whereas the SCP decreases to 50.99 W/kg and 47.33 W/kg. For an application that will mainly operate on such low T_{des} a study focusing in this regime is suggested.

At this point, it could be argued that instead of expecting the adsorbed mass to cycle between $\overline{w}_{rel} = 0\,\%$ and $\overline{w}_{rel} = 70\,\%$, the adsorbed mass could cycle between, for example, $\overline{w}_{rel} = 15\,\%$ and $\overline{w}_{rel} = 85\,\%$ in order to avoid approaching asymptotic behaviors near the equilibrium states. Even though the $Q_{cooling}$ would be the same for the two cases, there are two reasons for preferring the adopted approach. Firstly, it is desired to approach as much as possible the w^*_{min} at the end of the desorption phase, in order to maximize $(w^* - w)$ during the adsorption phase, and hence, maximize the adsorption rate and the SCP. Secondly, the COP is benefited when operating at a lower adsorbed mass range, since – as explained earlier – the adsorbate content and the associated thermal mass are lower.

3.4.6.3 Other operating parameters

The convection heat transfer coefficient U_{HTF} determines the heat transfer rate between the heat transfer fluid and the heat exchanger solid. The U_{HTF} depends on the HTF properties, the channel geometry, the flow regime and the fluid velocity. Figure 3.27 shows the reactor performance as a function of the U_{HTF}. As observed, increasing the U_{HTF} results in a higher SCP. However, the benefit of increasing the U_{HTF} decreases at higher values. Within the range under consideration, the gradient of the SCP curve drops from 0.046 $(Wkg^{-1})/(Wm^{-2}K)$ to 0.008 $(Wkg^{-1})/(Wm^{-2}K)$, suggesting that further increasing the U_{HTF} would not benefit significantly the SCP. At higher U_{HTF}, the thermal resistance between the heat exchanger solid and the HTF

becomes less relevant and the cooling of the reactor is hindered mainly by the low heat transfer within the packed bed and the thermal resistance at the interface of the packed bed and the heat exchanger solid. With respect to the COP, both the overall cycle cooling energy produced and the thermal energy input do not vary significantly, leading to a fairly steady COP across the range under consideration.

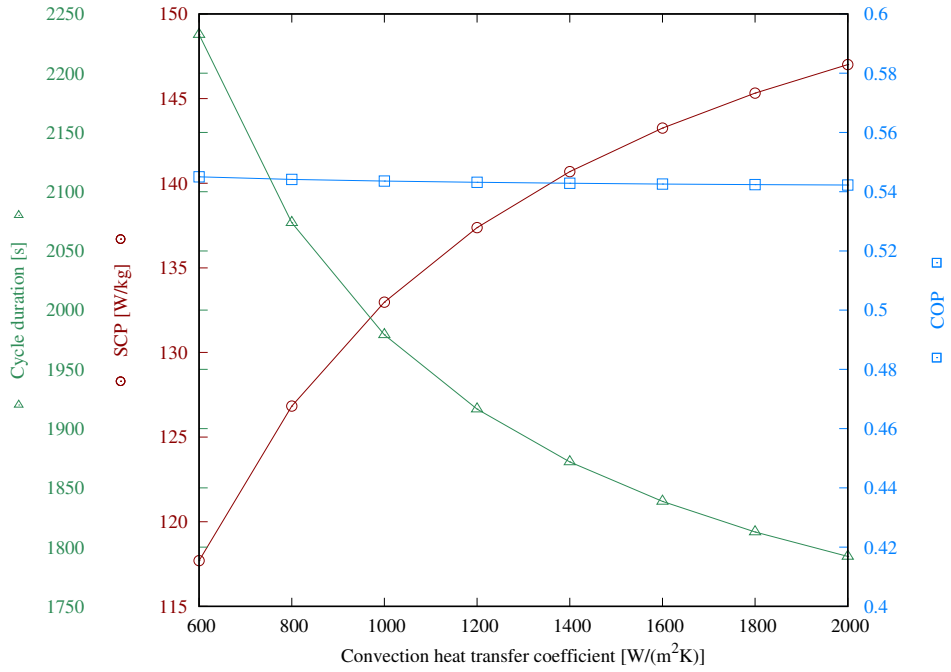

Figure 3.27: Reactor performance based on the convection heat transfer coefficient

All the results presented so far followed the cycling duration scheme described in Section 3.4.2, using 70% as the cycle adsorption percentage $\overline{w}_{\text{rel}}$. In this section, the influence of different $\overline{w}_{\text{rel}}$ is investigated and presented in Figure 3.28. Recalling the LDF model (equation 2.2), the adsorption rate is proportional to the difference between the equilibrium capacity and the instantaneous adsorbed mass. Therefore, the adsorption rate is at its maximum at the beginning of the adsorption phase and it decreases as equilibrium is approached. Consequently, the SCP is higher when the adsorption phase is terminated earlier, namely, at lower cycle adsorption percentage. On the other hand, the required thermal input rate decreases at higher cycle time, since

the temperature difference between the HTF and the reactor decreases. Prolonging the cycle time results in a higher COP, since the overall cooling energy produced during the adsorption phase - the COP numerator - increases at a higher rate in comparison to the overall thermal energy spent during the pre-heating and desorption phases - the COP denominator. Within the range under consideration, the combination (COP, SCP) can be adjusted between (0.46, 165.1 $\mathrm{W/kg_s}$) for $t_{\mathrm{cycle}} = 1023\,\mathrm{s}$ and (0.59, 82.9 $\mathrm{W/kg_s}$) for $t_{\mathrm{cycle}} = 4122\,\mathrm{s}$.

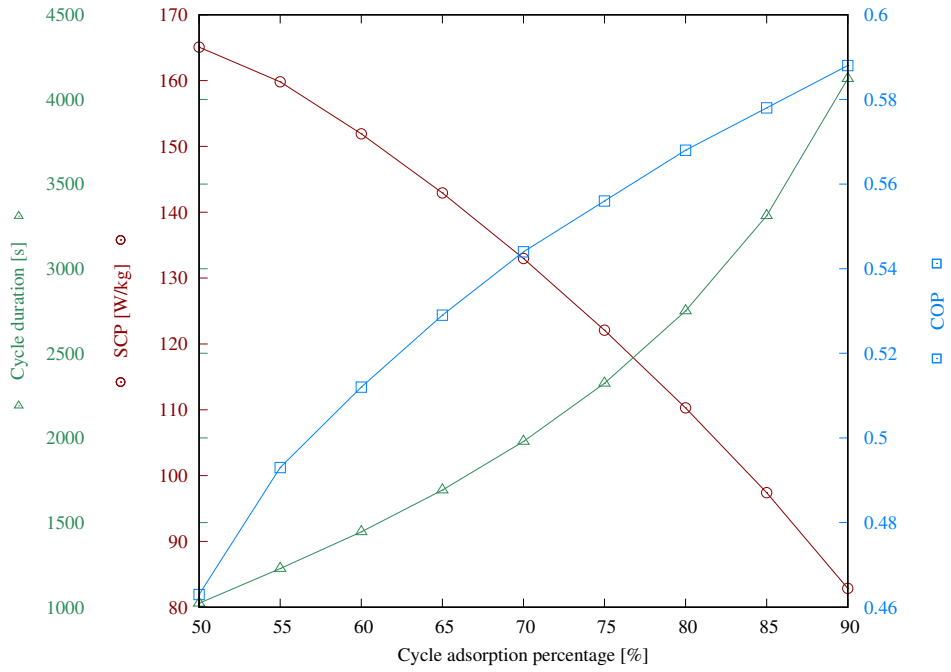

Figure 3.28: Reactor performance based on the cycle adsorption percentage

3.4.6.4 Heat exchanger material

In the previous study and particularly in Section 3.3.6.3, the effect of the heat exchanger solid on the $\mathrm{SCP_{ads}}$ was discussed. It was concluded that aluminium – in comparison to copper – results in slightly lower $\mathrm{SCP_{ads}}$, since it takes slightly longer to achieve $\overline{w}_{\mathrm{rel}} = 70\,\%$ in the adsorption phase. The latter is a consequence of the

lower conductivity of aluminium. In this study, the base case of the hexagonal honeycomb adsorption reactor is simulated with aluminium as heat exchanger solid, in order to observe the influence on the COP and the SCP of the cycle. The same effect is observed as in Section 3.3.6.3, namely, the adsorption phase lasts slightly longer.

However, the difference in the thermal mass of the two metals has two interesting effects. Aluminium has lower thermal mass than copper, in particular, $(\rho\, c_\mathrm{p})_\mathrm{Al} = 0.71 \times (\rho\, c_\mathrm{p})_\mathrm{Cu}$. Therefore, aluminium has lower thermal inertia. On the one hand, lower thermal inertia results in shorter pre-cooling and pre-heating time. It takes shorter period for the temperature switch of the heat exchanger solid, therefore, the reduction and the increase of pressure – during pre-cooling and pre-heating, respectively – are achieved in a shorter period. These reductions of the pre-cooling and pre-heating time compensate the slight increase of the adsorption phase duration, thus, the overall cycle duration decreases. Consequently, the SCP of the aluminium case is slightly higher (0.3%) than the SCP of the copper case.

On the other hand, the COP for the aluminium case is higher than for the copper case, as a result of its lower thermal mass. The corresponding values are 0.586 for aluminium and 0.544 for copper. Recalling the discussion of Section 3.3.6.4, the thermal energy input during pre-heating and desorption is distributed to (i) the increase of the heat exchanger solid temperature (ii) the temperature increase of the adsorbent and adsorbate and (iii) provide the endothermic thermal energy required for desorption. In order to capture the importance of the thermal input that corresponds to the heat exchanger solid, orientative values are provided, normalized per kg of adsorbent for ease of comparison. The energy required for desorbing the adsorbed mass w_rel from 70% to 0% – namely, a Δw of 0.111 $\mathrm{kg_w/kg_s}$ – is 299 $\mathrm{kJ/kg_s}$. The energy required for increasing the temperature of the adsorbent by 50 °C is 72 $\mathrm{kJ/kg_s}$ (evaluating the thermal capacity of the wet adsorbent at the average adsorbed mass). Lastly, for this geometry, the thermal energy required to increase 50 °C the heat exchanger solid is 122 $\mathrm{kJ/kg_s}$ for copper, whereas for aluminium is 87 $\mathrm{kJ/kg_s}$. This difference is reflected as a decrease in Q_heating and by consequence, as an increase of 7.7% in COP, for the case of aluminium.

3.4.6.5 Predetermined phases duration

The results presented above follow the cycle duration scheme presented in Section 3.4.2. This scheme is used only for design purposes, in order to determine the

required phase durations. This section aims to evaluate the reactor performance based on predetermined phases duration. The pre-cooling and pre-heating durations are considered equal $t_{pc} = t_{ph}$, as well as the adsorption and desorption durations $t_{ad} = t_{de}$. A total of 15 simulations were conducted, for the combinations of t_{pc} of 10, 30, 50 s and for t_{ad} of 600, 800, 1000, 1200, 1400 s. Prolonging the adsorption phase has the same effect as the previously presented cycle adsorption percentage, namely increase of COP and decrease of SCP. The effect of t_{pc} on SCP and COP is not significant. For a given t_{ad}, the variations of COP and SCP for the three t_{pc} are less than 1.8% and 2.8% respectively. Therefore, in Figure 3.29, only the case of $t_{pc} = 30$ s is plotted, for sake of clarity.

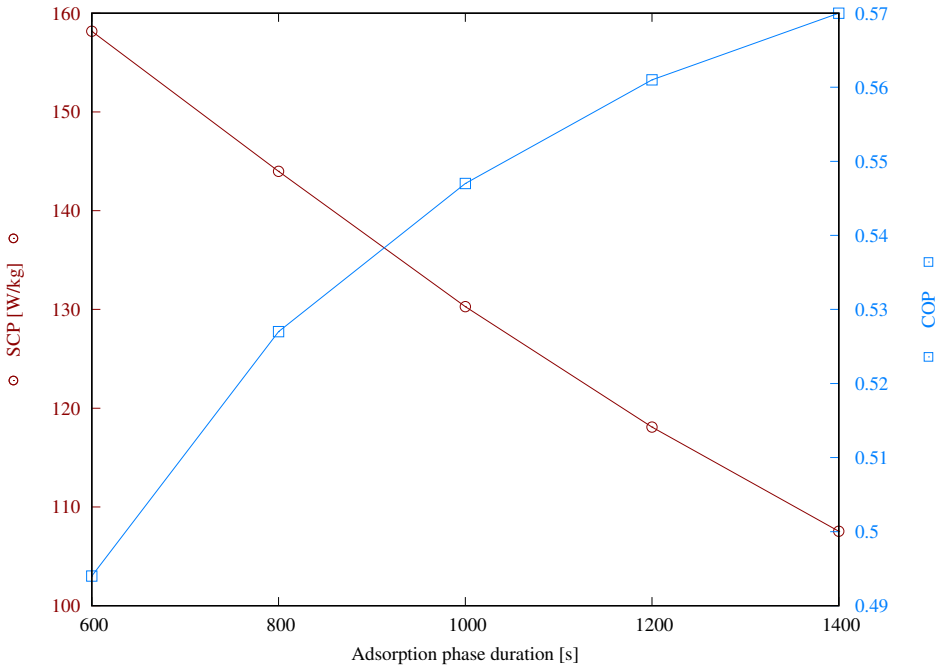

Figure 3.29: Reactor performance based on predetermined adsorption/desorption phase duration

However, the COP and SCP are performance indicators of the entire cycle. Figure 3.30 illustrates the instantaneous SCP for the three cases of t_{pc}, for $t_{ads} = 600$ s. As it can be observed, even though the overall cyclic cooling production does not vary

significantly, the SCP_{inst} exhibits considerable variations. In the case of $t_{pc} = 10\,s$ the pre-cooling phase is terminated prematurely. In other words, the reactor pressure is still higher than the evaporator pressure. Consequently, when the reactor is connected to the evaporator, vapor flows from the reactor towards the evaporator where it condenses. Since condensation is exothermic, this effect is counterproductive. Negative SCP_{inst} corresponds in heating inside the evaporator. The evaporator temperature will increase, depending on its thermal mass. In the case of $t_{pc} = 30\,s$, the pre-cooling phase is slightly longer than the required time to reduce the reactor pressure to the evaporator pressure $t_{pc} = 27.9\,s$, while in the case of $t_{pc} = 50\,s$ the reactor pressure decreases even further, hence, the vapor flow from the evaporator is more intense, leading to higher cooling production at the beginning of the cycle. The latter case would create a sudden cooling production peak in the evaporator and it should be taken into account in the design stage.

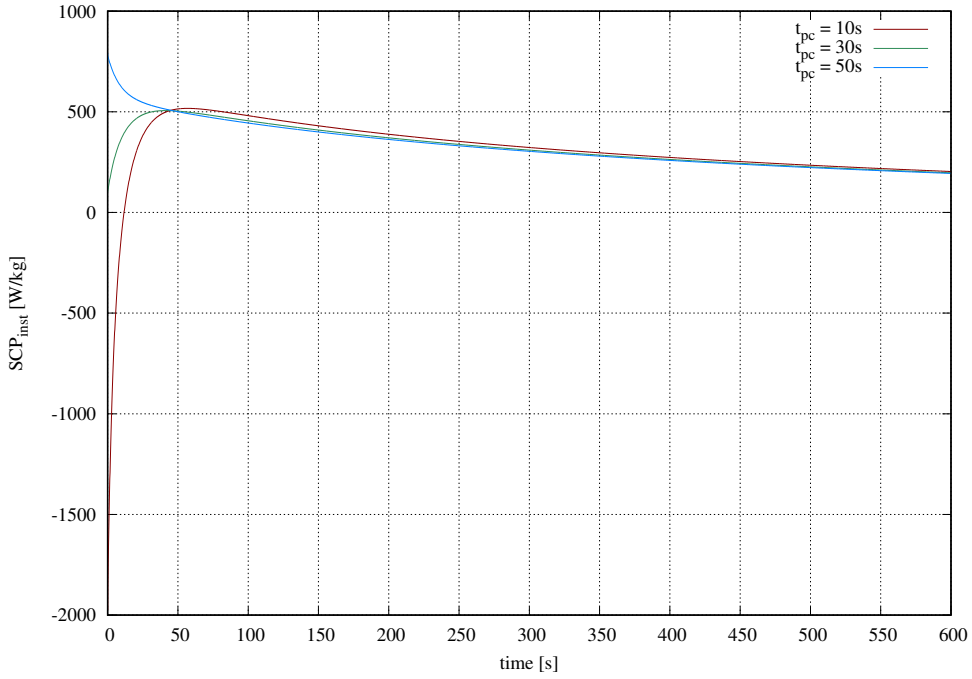

Figure 3.30: Instantaneous Specific Cooling Power during the adsorption phase for various t_{pc} and $t_{ad} = 600\,s$

3.5 Results discussion from engineering perspective

This section aims to provide an engineering perspective to the results presented in the previous sections. The reactor performance was characterized in terms of COP and SCP for the hexagonal honeycomb reactor. For the study concerning the five geometries, the SCP of the adsorption cycle was evaluated. Although the COP was not quantified yet for that study, the qualitative behavior is expected to be similar to the honeycomb reactor. Moreover, in Section 3.3.6.4, it was proven that maintaining the SVF constant results in a virtually equal COP across the geometries.

As it arises from the results, COP and SCP behave in a different manner with respect to the variation of the studied parameters. It should be emphasized that, even though both performance indicators are significant, their importance is determined by the context of the application. Different applications might prioritize the COP or the SCP, although a decent performance for both indicators is required.

The SCP expresses the cooling capacity per unit mass of adsorbent. Higher SCP is equivalent to less adsorbent material for a given cooling capacity and more compact reactors. Therefore, higher SCP is associated with lower initial investment with respect to the adsorbent material purchase and the fabrication of the reactor. Moreover, higher SCP is suitable for applications having space or weight constraints and thus, compactness is desired. Higher COP is equivalent to less thermal energy input for a given cooling capacity. Therefore, while SCP is more related to the initial investment, the COP is associated to the operating costs of the adsorption cooling system. Furthermore, a higher COP would reduce the potential carbon emissions from the operation of the ACS, if carbon-positive energy sources are involved in the thermal energy input.

An example of a COP-oriented application is a solar-driven cooling system located in a geographically isolated region. In this case, the system is equipped with an auxiliary heater in order to cover periods with insufficient solar radiation. The inevitable consumption of this auxiliary heater is inversely proportional to the COP. In such scenario, the fuel consumption of the auxiliary heater can be associated to high cost and low availability. Therefore, a higher COP would benefit the system operation by reducing the auxiliary heater consumption. An example of an SCP-oriented application is a vehicular cooling system driven by waste heat. In this case, the heat provided by the exhaust gases of the vehicle is not associated to any running costs.

Thus a lower COP can be accepted in order to achieve a higher SCP, and hence, a compact and lightweight cooling system. In applications that SCP and COP are equally important, a compromise between them should be reached. This could be any application where a balance is required between initial and operational expenses. According to the overall context of the adsorption cooling system, the geometry of the reactor should be designed carefully.

The operating temperatures also affect significantly the reactor performance. Low adsorption temperature and lower condenser temperature benefit considerably both the COP and the SCP. Therefore, the heat rejection device (e.g. the cooling tower) should be carefully designed, in order to reduce the HTF temperature effectively. Furthermore, depending on the application, the possibility of taking advantage of the outlet HTF from the condenser and adsorber should be considered. Exploiting this by-product of the ACS will reduce the energy consumption of another application, as well as the energy consumed by the heat rejection device. Potential applications include: (i) pre-heating the domestic hot water in a residential building or a tourist facility, (ii) in the latter, swimming pool heating and (iii) fuel pre-heating in vehicles or industry.

Increasing the desorption temperature results in a higher SCP. The COP is slightly affected in the range 70-90 °C, whereas it decreases at lower driving temperatures. Even though the ACS performance declines at lower driving temperatures, the fact that an ACS can operate in such conditions is an advantageous feature in comparison to absorption cooling, which cannot utilize so low driving temperature [27,28]. This renders adsorption cooling as the only candidate for certain thermally-driven applications, such as waste heat at low temperature or solar collectors of lower efficiency and thus, lower manufacturing cost. Furthermore, this feature should be taken into consideration in the design of the control strategy. In a solar-driven application, a cloudy morning might be associated with low driving temperature, but low cooling demand as well. It is then possible to allow the system to operate at a low driving temperature if its cooling capacity is capable to cover the cooling load, without activating the auxiliary heater and thus, reducing its energy consumption.

Attention should also be given in the convection heat transfer coefficient between the heat transfer fluid and the heat exchanger solid. On the one hand, a low value results in an additional thermal resistance and deteriorates the effectiveness of cooling down the reactor during the adsorption phase. On the other hand, increasing excessively the heat transfer coefficient does not benefit further the reactor performance and it

might lead to unnecessarily high HTF pumping energy consumption.

The cycle duration has strong impact on the COP and SCP. Shorter cycle durations provide high SCP and low COP, whereas longer cycle durations provide the inverse. Consequently, cycle duration is identified as a useful manner to regulate the reactor performance according to the instantaneous necessities. For example, during noon of a hot day in a solar-cooled building, SCP can be prioritized over COP. In such scenario, cooling load would peak, while solar radiation abounds and thermal storage tank is fully charged. Contrarily, during early morning COP should be prioritized over SCP. In this case, solar radiation is lower and might not suffice, thus the auxiliary system will be used. As commented earlier, the auxiliary heater consumption must be minimized. Therefore, higher COP is desired at the expense of lower SCP, which would be enough to cover the lower cooling load during early morning.

The material of the heat exchanger solid influences the SCP slightly in the majority of the cases. The inferior thermal conductivity of aluminium – as compared to copper – becomes noticeable in the results only for cases of large fin lengths. With respect to COP, the lower thermal mass aluminium benefits the COP by an increase of 7.7%. A general suggestion is to employ materials with high thermal conductivity and low thermal mass (product of density and specific heat capacity). Nevertheless, the choice of the material will be determined at large degree by technoeconomic criteria such as the material cost, as well as the cost and ease of fabrication.

Three fixed pre-cooling and pre-heating durations were studied. Although macroscopically they do not affect significantly the SCP and the COP, the instantaneous SCP varies significantly. If the pre-cooling is terminated prematurely, vapor will flow from the reactor to the evaporator, condense and provoke heating in the evaporator. Contrarily, if the pre-cooling is prolonged excessively, the reactor pressure would decrease significantly. In this case, once the reactor is connected to the evaporator, the vapor flux will provoke a disproportional peak to the cooling production. These should be taken into consideration in the design stage, in order not to provoke counterproductive heating nor excessive cooling in the evaporator. The latter could lead to freezing in the evaporator or deliver undesirably low temperature to the conditioned space.

3.6 Conclusions

In this chapter, two major studies were presented with respect to adsorption packed bed reactors, by employing the developed computational model, which was presented in Chapter 2.

Motivated by the low comparability between studies of different reactors encountered in the literature, a parametric study of five reactor geometries was conducted. This study pertains to the quantification of the SCP during the adsorption phase, SCP_{ads}. The Solid Volume Fraction (SVF) was introduced in order to render the five geometries comparable. Thirteen cases were studied for each of the five geometries by varying their SVF, fin length and fin thickness. The SVF influences significantly the SCP_{ads}. The SCP_{ads} for SVF=60 % is 2.49-3.45 times higher than for SVF=20 %. At the lowest SVF, the SCP_{ads} is geometry-independent, obtaining values in the range of 144.6-179.7 W/kg_s. On the contrary, at the highest SVF, it ranges from 413.4 W/kg_s (GEOM-B) to 535.8 W/kg_s (GEOM-D). For higher SVF, the geometries based on rectangular HTF channel (GEOM-D,E) exhibit better performance than the geometries based on circular HTF channel (GEOM-A,B,C). Regarding the fin length, the SCP_{ads} is geometry-independent at its lowest value $\gamma = 5\,mm$, since cooling the reactor is effective in all cases, resulting in a SCP_{ads} in the range of 368.9-399.5 W/kg_s. At increasing fin lengths, the SCP_{ads} decreases, though this decrease is more pronounced for the circular channel geometries with an average SCP_{ads} reduction of 80.3 % between $\gamma = 5\,mm$ and $\gamma = 40\,mm$, whereas for GEOM-D and GEOM-E such reduction is 29.4 % and 49.1 %, respectively. The parametric study of the fin thickness quantifies the empirical notion that thinner fins densely packed are preferable to thicker fins sparsely packed. At the highest fin thickness $\delta = 4\,mm$, the SCP_{ads} becomes geometry-independent, since its value is in the range of 131.8-155.3 W/kg_s. At the lowest fin thickness of the studied range, $\delta = 0.5\,mm$, the reactor geometry is relevant while the SCP_{ads} ranges from 344.7 W/kg_s (GEOM-B) to 464.5 W/kg_s (GEOM-E). The next stage of this study is the quantification of the COP for these geometries. This is an ongoing task, however, results regarding the COP for all five geometries for SVF=40 % and SVF=50 % demonstrate that for a given SVF the five geometries have virtually the same COP.

Subsequently, a thorough investigation was conducted with respect to a reactor geometry that remained underexplored hitherto – the hexagonal honeycomb adsorption reactor. This study pertains to the quantification of the cyclic SCP and COP. A para-

metric study was conducted with respect to the three dimensions that define the geometry, as well as for various operating parameters. The cell inradius β influence was investigated in the range of 1-6 mm (SVF=22.5-59.6 %). The dichotomy between SCP and COP is evident. The COP is 0.356 for $\beta = 1$ mm and 0.606 for $\beta = 6$ mm, whereas the SCP is 218.9 W/kg_s for $\beta = 1$ mm and 80.4 W/kg_s for $\beta = 6$ mm. With respect to the fin length γ, the SCP halves approximately in the range under consideration, being 159.5 W/kg_s for $\gamma = 5$ mm and 86.1 W/kg_s for $\gamma = 30$ mm. The COP is not significantly affected since the SVF does not vary considerably, being 38.3% for $\gamma = 5$ mm and 28.9% for $\gamma = 30$ mm. The inverse effect is observed for the influence of the fin thickness δ. The SCP is not significantly affected, being 127.6 W/kg_s for $\delta = 0.5$ mm and 140.5 W/kg_s for $\delta = 3$ mm. The impact of fin thickness on the COP is considerable. It ranges from 0.599 for $\delta = 0.5$ mm to 0.364 for $\delta = 3$ mm, since the respective SVFs are 22.5% for $\delta = 0.5$ mm and 59.6% for $\delta = 3$ mm. With respect to the operating temperatures, both performance indicators are maximized at the lowest adsorption and condenser temperature, as well as for the highest evaporator temperature. For the case of desorption temperature, the SCP exhibits its maximum at the highest value of the range under consideration, while for the COP a maximum is observed around 75-80 °C. The convection heat transfer coefficient does not affect the COP, whereas it influences the SCP at a larger extent at the lower side of the range under consideration. Caution is suggested in order to avoid, on the one hand, entailing an additional heat transfer resistance or, on the other hand, excessive HTF pumping consumption without a substantial improvement of the SCP. The cycle duration was investigated through predetermined values, as well as through the cycle adsorption percentage. The cycle duration choice provokes a dichotomy between SCP and COP. It is also identified as a parameter that allows to adjust the ACS performance in order to adapt it to the instantaneous operating conditions, cooling demand and source availability. For the case of the base scenario, a given reactor geometry, the combination (COP, SCP) can be adjusted through the cycle duration between (0.46, 165.1 W/kg_s) for $t_{cycle} = 1023$ s and (0.59, 82.9 W/kg_s) for $t_{cycle} = 4122$ s. Although the pre-cooling/pre-heating time was found to not affect the cyclic performance indicators, it has an important effect on the instantaneous SCP. As discussed in Section 3.5, short duration would lead to condensation and heat production in the evaporator, whereas excessively prolonged duration might lead to freezing in the evaporator or delivering undesirably low temperature to the conditioned space. Caution is suggested in the choice of these phases duration, since both effects are counterproductive. Copper and aluminium were compared as heat exchanger materials. The effect on

the SCP are not considerable. The COP for the aluminium case is 7.7% higher than the copper case, due to its lower thermal mass, being 0.586 and 0.544, respectively.

Finally, this chapter closes with a discussion of the results from an engineering perspective. Among other practical aspects of the results, the section emphasizes on the application-specific necessities in terms of SCP and COP, thus suggesting that the reactor design should be application-specific.

References

[1] Q. Zhang, X. Yang, P. Li, G. Huang, S. Feng, C. Shen, B. Han, X. Zhang, F. Jin, F. Xu, and T.J. Lu. Bioinspired engineering of honeycomb structure – using nature to inspire human innovation. *Progress in Materials Science*, 74:332 – 400, 2015.

[2] T. Hales. The honeycomb conjecture. *Discrete and Computational Geometry*, 25:1 – 22, 2001.

[3] İ. Solmuş, C. Yamali, C. Yildirim, and K. Bilen. Transient behavior of a cylindrical adsorbent bed during the adsorption process. *Applied Energy*, 142:115 – 124, 2015.

[4] Y. Liu and K.C. Leong. The effect of operating conditions on the performance of zeolite/water adsorption cooling systems. *Applied Thermal Engineering*, 25(10):1403 – 1418, 2005.

[5] H. Niazmand and I. Dabzadeh. Numerical simulation of heat and mass transfer in adsorbent beds with annular fins. *International Journal of Refrigeration*, 35(3):581 – 593, 2012.

[6] B.B. Saha, A. Chakraborty, S. Koyama, and Y.I. Aristov. A new generation cooling device employing $CaCl_2$-in-silica gel–water system. *International Journal of Heat and Mass Transfer*, 52(1):516 – 524, 2009.

[7] S.W. Hong, S.H. Ahn, O.K. Kwon, and J.D. Chung. Optimization of a fin-tube type adsorption chiller by design of experiment. *International Journal of Refrigeration*, 49:49 – 56, 2015.

[8] M. Khanam, S. Jribi, T. Miyazaki, B.B. Saha, and S. Koyama. Numerical investigation of small-scale adsorption cooling system performance employing activated carbon-ethanol pair. *Energies*, 11(6), 2018.

[9] M.B. Elsheniti, M.A. Hassab, and A.E. Attia. Examination of effects of operating and geometric parameters on the performance of a two-bed adsorption chiller. *Applied Thermal Engineering*, 146:674 – 687, 2019.

[10] S. Mitra, M. Muttakin, K. Thu, and B.B. Saha. Study on the influence of adsorbent particle size and heat exchanger aspect ratio on dynamic adsorption characteristics. *Applied Thermal Engineering*, 133:764 – 773, 2018.

[11] B. Golparvar, H. Niazmand, A. Sharafian, and A.A. Hosseini. Optimum fin spacing of finned tube adsorber bed heat exchangers in an exhaust gas-driven adsorption cooling system. *Applied Energy*, 232:504 – 516, 2018.

[12] M. Mahdavikhah and H. Niazmand. Effects of plate finned heat exchanger parameters on the adsorption chiller performance. *Applied Thermal Engineering*, 50(1):939 – 949, 2013.

[13] H.R. Ramji, S.L. Leo, and M.O. Abdullah. Parametric study and simulation of a heat-driven adsorber for air conditioning system employing activated carbon–methanol working pair. *Applied Energy*, 113:324 – 333, 2014.

[14] R.H. Mohammed, O. Mesalhy, M.L. Elsayed, and L.C. Chow. Novel compact bed design for adsorption cooling systems: Parametric numerical study. *International Journal of Refrigeration*, 80:238 – 251, 2017.

[15] R.H. Mohammed, O. Mesalhy, M.L. Elsayed, and L.C. Chow. Performance evaluation of a new modular packed bed for adsorption cooling systems. *Applied Thermal Engineering*, 136:293 – 300, 2018.

[16] M.M. Kowsari, H. Niazmand, and M.M. Tokarev. Bed configuration effects on the finned flat-tube adsorption heat exchanger performance: Numerical modeling and experimental validation. *Applied Energy*, 213:540 – 554, 2018.

[17] H. Zhang, X. Liu, H. Hong, and H. Jin. Characteristics of a 10 kW honeycomb reactor for natural gas fueled chemical-looping combustion. *Applied Energy*, 213:285–292, 2018.

[18] C. Corgnale, B. Hardy, R. Chahine, and D. Cossement. Hydrogen desorption using honeycomb finned heat exchangers integrated in adsorbent storage systems. *Applied Energy*, 213:426 – 434, 2018.

[19] M. Bilardo, G. Fraisse, M. Pailha, and E. Fabrizio. Design and experimental analysis of an integral collector storage (ICS) prototype for DHW production. *Applied Energy*, 259:114104, 2020.

[20] B. Shi, A. Elsayed, R. Al-Dadah, and S. Mahmoud. CFD simulation of honeycomb adsorption bed for automotive cooling system. In Proceedings of the International Conference on Heat Transfer and Fluid Flow, Prague, Czech Republic, 2014.

[21] M. Sosnowski, J. Krzywanski, K. Grabowska, M. Makowska-Janusik, W. Nowak, K. Sztekker, and A. Yousef. Implementation of honeycomb bed in an adsorption cooling technology. In Proceedings of ECOS 2019, The 32th International Conference on efficiency, cost, optimization, simulation and environmental impact of energy systems, June 23-28, Wroclaw, Poland.

[22] T.L. Bergman, A.S. Lavine, F.P. Incropera, and D.P. DeWitt. *Fundamentals of Heat and Mass Transfer*. John Wiley and Sons, 7th edition, 2011.

[23] X. Wang, W. Zimmermann, K.C. Ng, A. Chakraboty, and J.U. Keller. Investigation on the isotherm of silica gel+water systems. *Journal of Thermal Analysis and Calorimetry*, 76(2):659 – 669, 2004.

[24] Fuji Silysia Chemical LTD. (Nagoya, Japan). www.fuji-silysia.co.jp. Accessed: 2020-12-15.

[25] H.T. Chua, K.C. Ng, W. Wang, C. Yap, and X.L. Wang. Transient modeling of a two-bed silica gel–water adsorption chiller. *International Journal of Heat and Mass Transfer*, 47(4):659 – 669, 2004.

[26] I.S. Glaznev and Y.I. Aristov. The effect of cycle boundary conditions and adsorbent grain size on the water sorption dynamics in adsorption chillers. *International Journal of Heat and Mass Transfer*, 53(9):1893 – 1898, 2010.

[27] R. Wang, L. Wang, and J. Wu. *Adsorption Refrigeration Technology*. John Wiley and Sons, 2014.

[28] S. Ajib and A. Alahmer. Solar Cooling Technologies. In Ibrahim H. Al-Bahadly, editor, *Energy Conversion - Current Technologies and Future Trends*, Chapters. IntechOpen, October 2019.

4

Development of a computational model for adsorption cooling systems

Contents of this chapter have been included in :
- G. Papakokkinos, J. Castro, R. Capdevila and R. Damle, A comprehensive simulation tool for adsorption-based solar-cooled buildings – Control strategy based on variable cycle duration, *Energy and Buildings*, 231, 110591, 2021

4.1 Introduction

While Chapter 2 and 3 were dedicated to the simulation of the adsorption reactor, Chapter 4 and 5 are dedicated to the simulation of the entire adsorption cooling system (ACS), using a component-level approach. Chapter 4 presents the construction of the computational model, while Chapter 5 presents a numerical study of an adsorption-based solar-cooled building, utilizing the developed model.

This chapter focuses on the presentation of the ACS model development and validation. The last section presents briefly the components that are coupled to the ACS model in order to form a comprehensive tool for adsorption-based solar-cooled buildings. These are the solar collectors, the thermal storage and the NEST-buildings library. The latter was previously developed in CTTC and it is not a product of this doctoral thesis.

Component-level models are widely used in the investigation of adsorption cooling systems, mostly for the simulation of different configurations of the adsorption cooling cycle. Among other, component-level models were used for the simulation of the conventional two-bed configuration cycle [1], the two-bed cycle with heat recovery [2], the two-bed cycle with mass recovery [3], multi-bed cycles [4,5], multi-bed cycles with dual evaporator [6,7], and two-stage multi-bed cycles [8]. A detailed literature review is beyond the scope of this document. In the context of this thesis,

the intended use of the ACS model is its integration with the solar collectors, thermal storage and the building. An extensive literature review on this topic is presented in Chapter 5.

4.2 Mathematical Formulation

4.2.1 Introduction

A description of the simulated ACS can be found in Section 1.2.2.2. The four components of the adsorption cooling system – the evaporator, the condenser and the two adsorption reactors – are modeled individually. The adopted approach differs from the majority of the component-level modeling studies, as it considers one-dimensional models for the adsorption reactors, instead of the commonly adopted lumped capacitance approach. Studies based on lumped capacitance models use the Number of Transfer Units (NTU) method for the calculation of the heat exchange between the heat transfer fluid (HTF) and the reactor. However, the NTU method is applicable only in steady state, where the fluid flow is thermally developed. Such approach is not appropriate for adsorption reactors, since it fails to capture the effects of HTF residence time and thermal inertia during the switching from heating to cooling the reactor and the inverse. When the switching takes place, the HTF inlet temperature is very different to the temperature profile across the tube, and therefore, the NTU method is not valid. Consequently, one-dimensional models are considered more appropriate for modeling the adsorption reactors. The condenser and the evaporator are not significantly affected from the cyclic operation of the reactors, and therefore, their modeling is based on the lumped capacitance approach.

A priority of this work was to experimentally validate the ACS model. The experimental validation was based on the adsorption chiller SorTech ACS 05, whose experimental data are presented in the doctoral thesis of M. Schicktanz [9]. Consequently, the modeling approach is adapted to certain particularities of the adsorption chiller used for the experimental validation.

4.2.2 Adsorption reactors

The heat exchanger of the adsorption reactor under consideration is a finned tubular reactor. The main HTF mass flow is distributed to various finned tubes. The space between the fins is filled with the adsorbent with the use of an adhesive material. The tubes are expected to have similar thermal behavior and adsorption rate. Therefore the simulation of one tube is sufficient to extract conclusions for the entire reactor. Furthermore, this configuration allows to extrapolate results to different capacities of ACS by assuming that more tubes are incorporated to the heat exchanger.

The finned tube is discretized one-dimensionally, and the following equations for adsorption equilibrium, adsorption kinetics and energy conservation are solved for each control volume. For the pre-heating and pre-cooling phases – when the reactor is disconnected from the evaporator and the condenser – a mass conservation equation and the ideal gas law are also solved.

Adsorption equilibrium
The adsorption equilibrium capacity is calculated through the adsorption isotherm, a relation that provides the adsorption equilibrium capacity w^* as a function of the temperature and pressure. In this study, the adsorbate is water and the adsorbent is the silica gel type RD [10]. For this adsorption pair, Wang et al. [11] derived experimentally the Tóth isotherm.

$$w^{*n} = \frac{K_0 \exp(\Delta H_{\text{ads}}/(R_{\text{g}} T^n)) P_{\text{reac}}}{\left[1 + \left(\frac{K_0}{q_m} \exp(\Delta H_{\text{ads}}/(R_{\text{g}} T^n)) P_{\text{reac}}\right)^{\tau}\right]^{1/\tau}} \tag{4.1}$$

The relevant input parameters may be found in Table 3.2. It should be noted, that for the experimental validation, the isotherm of silica gel 127B reported in [9] is used. The reason for considering silica gel type RD in the numerical studies – instead of the 127B – is that the silica gel type RD is more widely used and studied, and its properties are more well-documented.

Adsorption kinetics
The adsorption kinetics describe the velocity of the adsorption rate from the current state of the adsorbed mass w towards the equilibrium capacity w^*. For the calculation

of the adsorption rate, the Linear Driving Force model is used [12].

$$\frac{dw}{dt}^n = \frac{60 D_e}{d_{\mathrm{p}}^2}(w^{*n} - w^n) \tag{4.2}$$

The D_e is the temperature-dependent effective diffusivity, calculated by the Arrhenius equation (equation 4.3), using the reference diffusivity D_0, the activation energy E_a, the universal gas constant R and the temperature in the control volume under consideration T^n. The relevant input parameters may be found in Table 3.2.

$$D_e = D_0 \exp(-E_a/(RT^n)) \tag{4.3}$$

Energy conservation equations
For each control volume of the tubular adsorption reactor, three energy equations are solved, for (i) the heat transfer fluid of the secondary circuit, (ii) the heat exchanger and (iii) the packed bed. Heat transfer takes place between the heat transfer fluid and the heat exchanger, as well as between the heat exchanger and the packed bed.

- Heat Transfer Fluid of the secondary circuit:

$$(Mc_{\mathrm{p}})^n_{\mathrm{HTF}} \frac{\partial T^n_{\mathrm{HTF}}}{\partial t} = (\dot{m} c_{\mathrm{p}})_{\mathrm{HTF}} (T^{n-1}_{\mathrm{HTF}} - T^n_{\mathrm{HTF}}) + (UA)^n_{\mathrm{HX\text{-}HTF}} (T^n_{\mathrm{HX}} - T^n_{\mathrm{HTF}}) \tag{4.4}$$

  The Nusselt number for the calculation of the heat transfer coefficient U_{HX-HTF} is based on the Gnielinski equation, using the Petukhov relation for the friction factor [13]. The required temperature-dependent properties of water are evaluated at the average temperature between T^n_{HX} and the T^n_{HTF} on the control volume under consideration.

- Heat Exchanger:

$$(Mc_{\mathrm{p}})^n_{\mathrm{HX}} \frac{\partial T^n_{\mathrm{HX}}}{\partial t} = \lambda_{\mathrm{tube}} \nabla^2 T_{\mathrm{HX}} + (UA)^n_{\mathrm{HX\text{-}HTF}} (T^n_{\mathrm{HTF}} - T^n_{\mathrm{HX}}) + (UA)^n_{\mathrm{HX\text{-}PB}} (T^n_{\mathrm{PB}} - T^n_{\mathrm{HX}}) \tag{4.5}$$

  where $(Mc_{\mathrm{p}})^n_{\mathrm{HX}} = (Mc_{\mathrm{p}})^n_{\mathrm{tube}} + (Mc_{\mathrm{p}})^n_{\mathrm{fins}}$. The heat transfer coefficient between the heat exchanger and the packed bed $U_{\mathrm{HX\text{-}PB}}$ is set to $100\,\mathrm{Wm^{-2}K^{-1}}$ [14].

- Adsorption Packed Bed:

$$(Mc_{\mathrm{p}})^{n}_{\mathrm{PB}}\frac{\partial T^{n}_{\mathrm{PB}}}{\partial t} = fM^{n}_{\mathrm{sg}}\left(\frac{\partial w}{\partial t}\right)^{n}\left[\Delta H_{\mathrm{ads}} + \phi c_{\mathrm{p,vap}}(T_{\mathrm{eva}} - T^{n}_{\mathrm{PB}}) + \xi c_{\mathrm{p,vap}}(T_{\mathrm{con}} - T^{n}_{\mathrm{PB}})\right] + (UA)^{n}_{\mathrm{HX\text{-}PB}}(T^{n}_{\mathrm{PB}} - T^{n}_{\mathrm{HX}}) \tag{4.6}$$

where $(Mc_{\mathrm{p}})^{n}_{\mathrm{PB}} = (Mc_{\mathrm{p}})^{n}_{\mathrm{sg}} + (Mc_{\mathrm{p}})^{n}_{\mathrm{adh}} + f(M_{\mathrm{sg}}c_{\mathrm{p,liq}}w)^{n} + (1-f)(M_{\mathrm{sg}}c_{\mathrm{p,liq}}w_{\mathrm{m}})^{n}$.

The thermal mass of the packed bed control volume corresponds to the thermal mass of the silica gel, the adhesive and the adsorbed phase. According to the experimental study [9], a fraction of the silica gel is inactive in terms of adsorption (its exterior pores are blocked by the adhesive). However, its thermal mass is taken into account, assuming an average adsorbed mass $w_{\mathrm{m}} = [(w^{*}(P_{\mathrm{eva}}, T_{\mathrm{ads}}) + w^{*}(P_{\mathrm{con}}, T_{\mathrm{des}})]\,/2$. The silica gel active fraction is denoted as f. The flag ϕ is 0 throughout the cycle, except during the adsorption phase, when it is set to 1 in order to take into account the cold vapor entering into the reactor from the evaporator. During desorption phase, the normal direction of the vapor flow is from the reactor towards the condenser. However, if the pre-heating time is insufficient, backflow occurs from the condenser towards the reactor. In those cases, flag ξ is set to 1 in order to take into account the sensible heat associated to this backflow.

Pressure equation

The pressure of the adsorption reactor is imposed by the evaporator or the condenser, when the reactor is connected to each of them. During the pre-heating and pre-cooling phases, the pressure is calculated based on the ideal gas law. When the reactor is disconnected from the evaporator or the condenser, the vapor mass inside the reactor is calculated and a mass conservation equation (equation 4.8) is solved throughout the pre-heating and pre-cooling phases. The calculated density is then used for the calculation of the pressure based on the ideal gas law.

$$P_{\mathrm{reac}} = \begin{cases} P_{\mathrm{eva}} & \text{adsorption} \\ P_{\mathrm{con}} & \text{desorption} \\ \rho_{\mathrm{g}} R_{\mathrm{g}} T & \text{pre-heating/cooling} \end{cases} \tag{4.7}$$

Mass conservation equation
The mass conservation equation takes into account the density variations in the void space volume V_g of the reactor, as a result of adsorption or desorption.

$$V_g \frac{\partial \rho_g}{\partial t} = f M_{sg} \overline{\frac{\partial w}{\partial t}} \tag{4.8}$$

where $\overline{\partial w/\partial t}$ is the average adsorption rate throughout the reactor.

4.2.3 Condenser and Evaporator

With respect to the mass conservation of the condenser, the typical assumption of constant water mass is adopted. The outlet condensed water mass flow rate is considered equal to the inlet vapor mass flow rate. For the evaporator, the mass conservation equation for water is expressed by equation (4.9).

$$\frac{\partial M_l}{\partial t} = \psi f M_{sg} \left[- \left(\overline{\frac{\partial w}{\partial t}} \right)_{ads} + \left(\overline{\frac{\partial w}{\partial t}} \right)_{des} \right] \tag{4.9}$$

The flag ψ is zero during pre-heating and pre-cooling phases, whereas during adsorption and desorption is set to 1. Equations 4.10 and 4.11 represent the energy conservation equation for the condenser and the evaporator, respectively.

$$(M c_p)_{con} \frac{\partial T_{con}}{\partial t} = \psi f M_{sg} \left[\left(\overline{\frac{\partial w}{\partial t}} \right)_{des} \Delta H_{con} + c_{p,vap}(T_{des} - T_{con}) \right] + \dot{Q}_{sec} \tag{4.10}$$

$$\frac{\partial (Mh)_{eva}}{\partial t} = \psi f M_{sg} \left[- \left(\overline{\frac{\partial w}{\partial t}} \right)_{ads} \left(h_{vap,sat,T_{eva}} + \zeta c_{p,vap}(T_{PB} - T_{eva}) \right) + \left(\overline{\frac{\partial w}{\partial t}} \right)_{des} h_{liq,sat,T_{con}} \right] + \dot{Q}_{sec} \tag{4.11}$$

Similarly to flag ξ in equation (4.6), the flag ζ in equation (4.11) is set to 1 only when vapor backflow occurs from the reactor to the evaporator, in order to take into account its sensible heat.

The heat exchanged with the secondary circuit $\dot{Q}_{sec}$ is calculated based on the NTU approach, described by the equations 4.12 and 4.13.

$$\dot{Q}_{\mathrm{sec}} = \dot{m}_{\mathrm{sec}} c_{\mathrm{p,sec}} \epsilon (T_{\mathrm{sec,in}} - T_{\mathrm{eva/con}}) \tag{4.12}$$

$$\epsilon = 1 - \exp\left(\frac{-(UA)_{\mathrm{eva/con}}}{\dot{m}_{\mathrm{sec}} c_{\mathrm{p,sec}}}\right) \tag{4.13}$$

4.3 Numerical solution

The component models are implemented within NEST, an in-house, C++ based, object-oriented platform, which allows the interaction between various models of different complexity. An implicit temporal discretization scheme and the Gauss-Seidel method are used. For each timestep, all the components models are solved. After the solution of each component, the updated values are sent to the components which interact with it. If a control strategy is applied, the relevant input is assessed based on the control criteria and the associated action is taken (e.g. deactivate a pump, valve switching etc.). Once all the components are solved, the procedure is repeated until convergence is achieved. NEST possesses parallel computing capabilities, which allow to distribute the simulation in various CPUs in order to reduce the computational time.

4.4 Model validation

4.4.1 Validation case

The numerical model of the adsorption cooling system was compared to experimental results, adopting reasonable assumptions where the required information was unavailable.

The criteria sought in the chosen experiment were to provide both transient experimental results such as the outlet temperature of the secondary circuits and the pressure of the condenser and evaporator, as well as experimentally measured cycle performance indicators, namely the COP and the cooling capacity. Furthermore, the

sought experiment should provide the required information to scale the capacity of the validated model, in order to study ACSs of different cooling capacities.

As mentioned earlier, the chosen experiment for this task is the one presented by Schicktanz in his doctoral thesis [9], concerning the commercial adsorption chiller SorTech ACS 05. He also constructed a numerical model for the simulation of this adsorption chiller. Although the modeling approach adopted in the present study is different, the experimental data provided are used for the validation of the presented model. The most important characteristics of the ACS are presented in Table 4.1, while Table 4.2 presents the operating conditions of the experiment. For further information, the reader is referred to [9].

Table 4.1: Adsorption cooling system characteristics [9]

	Value	Unit
Adsorption reactors		
Adsorption reactors quantity	2	-
Heat exchangers per adsorption reactor	2	-
Tubes per HX	6	-
Tube length	12 x 0.685	m
Tubes mass per HX	5.3	kg
Fins mass per HX	4	kg
Fins area per HX A_{fins}	12.6	m^2
Tube heat capacity $c_{\text{p,tube}}$	897	$\text{J}\,\text{kg}^{-1}\,\text{K}^{-1}$
Fins heat capacity $c_{\text{p,fins}}$	385	$\text{J}\,\text{kg}^{-1}\,\text{K}^{-1}$
Tube diameter d_{tube}	8.92	mm
M_{sg} per HX	8.4	kg
M_{adh} per HX	1.5	kg
Evaporator and Condenser		
Tube and fins mass	22	kg
Tube and fins heat capacity $c_{\text{p,eva/con}}$	385	$\text{J}\,\text{kg}^{-1}\,\text{K}^{-1}$
$(UA)_{\text{eva}}$	890	$\text{W}\,\text{K}^{-1}$
$(UA)_{\text{con}}$	3200	$\text{W}\,\text{K}^{-1}$

Table 4.2: Operating conditions for the experimental validation [9]

Input parameter	Value	Unit
$\dot{V}_{\text{HTF,des}}$	1.013	$m^3\,h^{-1}$
$\dot{V}_{\text{HTF,ads}}$	1.562	$m^3\,h^{-1}$
$\dot{V}_{\text{HTF,con}}$	1.138	$m^3\,h^{-1}$
$\dot{V}_{\text{HTF,eva}}$	1.736	$m^3\,h^{-1}$
$T_{\text{HTF,high}}$	75	°C
$T_{\text{HTF,medium}}$	28	°C
$T_{\text{HTF,low}}$	17	°C

4.4.2 Assumptions

Intraparticle mass transfer rate

With respect to the intraparticle mass transfer rate, in Schicktanz' thesis a constant coefficient is assumed, without any dependence on the particle diameter and the temperature [9]. In the present work, such approach is avoided, since the diffusivity, and thus the adsorption rate, depend significantly on the temperature and the particle diameter. Therefore, the Linear Driving Force model is employed (equation 4.2), a typical approach across related literature.

However, the LDF model requires the knowledge of three parameters for the silica gel 127B which are not reported in [9] or elsewhere. The parameters are: (i) the reference diffusivity, (ii) the activation energy for the Arrhenius equation, and (iii) the adsorbent particle size. For the former two parameters, the silica gel RD values are used, assuming that these properties will not differ significantly between the two silica gels, since they both are regular density silica gels [15]. For the particle diameter, the value reported by Fraunhofer researchers in another work is used [16].

Silica gel mass

Schicktanz provides a series of arguments explaining that only a fraction of the silica gel mass reported by the manufacturer is active in the adsorption process. Some of these arguments are: (i) the adhesive blocked the pores of some adsorbent particles and does not allow the mass transfer inside the particle, (ii) the adsorbent was not

completely dry when measuring its mass, thus it appeared to have higher mass while in reality, it was partially loaded, and (iii) during the installation or the operation of the chiller, some particles fell off and they are not in contact with the heat exchanger.

It is impossible to quantify a priori the fraction of the reported silica gel mass that is active. Consequently, a parameter identification study was conducted for the silica gel active fraction f, by fitting the numerical results to the experimental results presented in Table 4.3. Schicktanz also performed parameter identification for this quantity and proposed the value of 0.667 [9]. In the present study, this fraction has been determined as 0.685.

Additional thermal mass

The sum of the masses reported by Schicktanz and presented in Table 4.1 is 120.8 kg. However the mass of the entire chiller is reported as approximately 200 kg [17]. Consequently, it is safe to assume that the masses reported by Schicktanz do not account for the entire thermal mass of the chiller, while elements such as tubes, valves and the components' shells might not be included. In this study, an additional mass of 15kg per reactor heat exchanger is considered. Such value is reasonable when comparing the mass reported by Schicktanz and the entire chiller mass reported in [17], as well as by estimations regarding the mass of the reactor shell.

Thermal losses

Implementing the aforementioned assumptions to the model results in a slightly higher COP value, since the thermal losses are not taken into account. Without thermal losses, the numerically derived COP is 0.612 whereas the experimental value is 0.587. An energy balance of the cycle based on the experimental results of Schicktanz shows that the sum of the heat fluxes of the secondary circuits is not zero, as it would result in the case of a thermodynamic cycle without thermal losses. The imbalance was calculated to 813.5 kJ, which may be interpreted as 320.2 W throughout the cycle. This amount of thermal losses is incorporated in the model, by distributing it along the high temperature secondary circuit. It is assumed that the thermal losses take place exclusively there, since it has the highest temperature difference with the ambient temperature.

4.4.3 Results comparison

Table 4.3 presents the comparison of the numerical results and the experimentally measured results by Schicktanz with respect to the COP, the cooling capacity and the thermal power input, provided by the high temperature secondary circuit to the ACS.

Table 4.3: Comparison of the experimental and numerical results

	COP		Cooling Production		Input Heat	
	Value [-]	ϵ [%]	Value [kW]	ϵ [%]	Value [kW]	ϵ [%]
Experimental [9]	0.587	-	3.62	-	6.17	-
Numerical	0.5867	-0.05	3.617	-0.08	6.165	-0.08

Figures 4.1 and 4.2 compare the temporal profiles as measured experimentally by Schicktanz, and as computed numerically by the model presented in this study. Figure 4.1 illustrates the outlet temperature profile of the desorber, adsorber and evaporator, while Figure 4.2 shows the pressure in the condenser and evaporator.

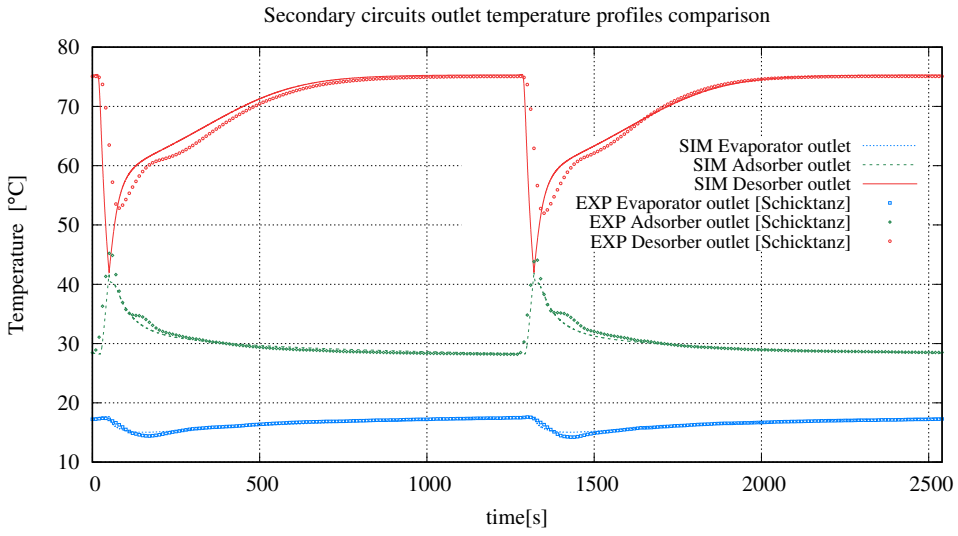

Figure 4.1: Secondary circuits outlet temperature – Experimental and numerical results comparison

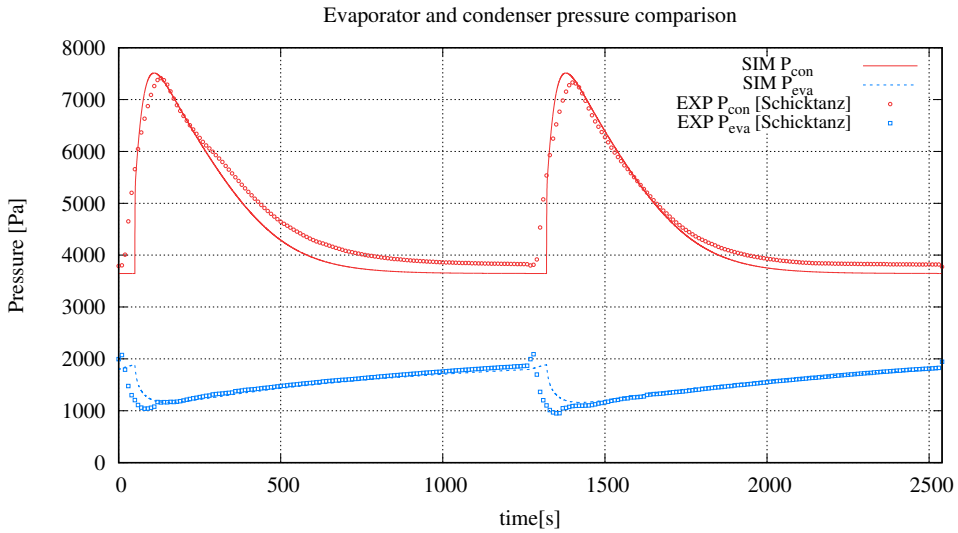

Figure 4.2: Pressure in condenser and evaporator – Experimental and numerical results comparison

4.4.3.1 Discrepancy between the experimental and the numerical results

With respect to the cycle performance indicators presented in Table 4.3, the model predicts the experimental results quite accurately, with a maximum relative error of 0.08%. The temporal profiles presented in Figures 4.1 and 4.2 are predicted less accurately, however, the general behavior is captured qualitatively and quantitatively well. As it can be observed, the discrepancies are mostly manifested when valves switching takes place (t=0, 50, 1270, 1320 s).

The discrepancies between the results may be attributed to various factors. Apart from common factors (limitations of the model, errors related to the conduction or the documentation of the experiment, and uncertainties introduced by the aforementioned assumptions), there is a series of important factors that are responsible for the discrepancies around valve switching:

- An important distinction between the numerical model and the experiment is related to the valves switching, when the high and medium temperature

secondary circuits are redirected from one reactor to the other. While this switching takes place instantaneously in the model, in reality it has a duration that lasts about 15s. This effect results in an uncontrolled mixing of the two flows [9].

- The thermal inertia of the temperature sensors reduces their capacity to capture sudden peaks of temperature [9].
- The temperature sensors data acquisition interval is 10 seconds [9], thus, it is possible that peaks within this interval are missed by the data acquisition system.

Having acknowledged the weaknesses of this experimental validation – arising from the adopted assumptions where the required information is unavailable – it is considered that the numerical model can simulate the adsorption chiller with sufficient accuracy for its intended purpose, which is to study the adsorption chiller behavior while integrated within a larger thermal system.

4.5 Other models in the adsorption-based solar-cooled building simulations

4.5.1 Solar collectors

The solar collectors considered in this study are flat-plate collectors. Their efficiency function is described by equation 4.14 [18]:

$$\eta = 0.792 - 3.940\frac{T_{sc,a} - T_{amb}}{I_{sc,inc}} - 0.012\frac{(T_{sc,a} - T_{amb})^2}{I_{sc,inc}} \tag{4.14}$$

where $T_{sc,a}$ is the average temperature between the collector inlet and outlet, T_{amb} the ambient temperature and $I_{sc,inc}$ the incident radiation per square meter of solar collector. Using the calculated efficiency and the area of the collector, the solar outlet temperature is determined by equation 4.15, considering the mass flow rate and the thermal capacity of an antifreeze water-glycol mixture.

$$T_{sc,out} = T_{sc,in} + \frac{\eta_{sc} A_{sc} I_{sc,inc}}{\dot{m}_{aff} c_{p,aff}} \tag{4.15}$$

The collectors connected in series consider as inlet temperature the outlet temperature of the previous collector, in order to capture the efficiency reduction due to heat losses when operating at higher temperature. For the simulations, the total collector field is divided into sub-fields of 5 collectors of 2 m^2, connected in series.

4.5.2 Thermal storage

The thermal storage tank is connected directly to the solar system and provides thermal energy to the desorbing reactor of the ACS through a heat exchanger. It is equipped with an auxiliary heater and the thermal losses to the environment are taken into account through a thermal resistance R_{amb}, applied to its external surface A_{ext}.

The temporal evolution of its temperature is described by equation (4.16).

$$(Mc_p)_{aff}\frac{\partial T_{tank}}{\partial t} = \dot{m}_{aff}c_{p,aff}(T_{sc,out} - T_{tank}) + \epsilon(\dot{m}c_p)_{HTF}(T_{ACS,out} - T_{tank}) + \frac{T_{tank} - T_{amb}}{R_{amb}/A_{ext}} + \beta\dot{Q}_{aux} \tag{4.16}$$

where ϵ is the effectiveness of the heat exchanger, and flag β marks whether the auxiliary heater is activated or deactivated, taking the value of 1 or 0, respectively.

4.5.3 Building model

For the building simulation, the NEST-buildings library was utilized. This library was previously developed in the CTTC laboratory. The building model is presented briefly. For a detailed presentation of the mathematical formulation of the building model, the reader is referred to [19].

The building model takes into account the following physical phenomena:

- Walls, Floor and Roof:
  - Heat conduction through multi-layer walls and thermal inertia effects (thermal energy accumulation) based on one-dimensional discretization.

  - On the interior side, heat convection with interior air and thermal radiation heat transfer with the other walls of the room, the roof and the floor, depending on their view factors.
  - On the exterior side, heat convection with ambient air, solar radiation and thermal radiation heat transfer with sky for the walls and the roof; whereas for the floor, heat conduction with the ground.
  - Solar radiation transmitted through the windows.
- Multi-glazed windows:
  - For each glass layer the same physical mechanisms as in the wall case are applied, with respect to heat conduction, heat convection and thermal inertia effects.
  - Reflection, absorption and transmission of solar radiation for each glass layer.
  - Natural convection heat transfer in the air chamber between the glass layers.
  - Thermal radiation heat transfer between the glass layers.
- Interior air:
  - Convection heat transfer with the walls, roof, floor and the interior glass layer of the windows.
  - Internal heat and moisture gains provoked by human presence and operation of electrical appliances.
  - Heat and mass transfer related to ambient air fluxes as a consequence of ventilation and infiltrations.

The interaction between the ACS and the building takes place in the air-conditioning unit. The latter pertains to a fan-coil; a cross-flow, air-to-water heat exchanger. The HTF exiting the evaporator is circulated through the fan-coil, while interior air is also forced through it. The HTF exchanges energy with the interior air in order to cool it down. While on the water side of the heat exchanger only sensible heat transfer occurs, on the air side, humidity condensation occurs if the temperature is lower than the interior air dew point, which is calculated based on its temperature and humidity. The challenging part of the solution of the fan coil is to determine the ratio of sensible and latent heat exchanged on the air side, when condensation occurs. For the fan-coil solution, the method proposed by Braun [20] was implemented in the model. For the

convective heat transfer coefficient on the air side of the coil, the relations proposed by Abu Madi et al. [21] and Wang et al. [22] are adopted for dry and wet coil, respectively.

The reliability of the NEST-buildings model was tested based on the BESTEST procedure, published by Judkoff and Neymark [23]. The validation pertains to the cases of free-floating mode, and heating and cooling mode – both for a lightweight and a heavyweight building. For the results of this validation the reader is referred to [19, 24].

References

[1] I.I. El-Sharkawy, H. AbdelMeguid, and B.B. Saha. Towards an optimal performance of adsorption chillers: Reallocation of adsorption/desorption cycle times. *International Journal of Heat and Mass Transfer*, 63:171 – 182, 2013.

[2] X. Wang and H.T. Chua. Two bed silica gel–water adsorption chillers: An effectual lumped parameter model. *International Journal of Refrigeration*, 30(8):1417 – 1426, 2007.

[3] A. Akahira, K.C.A. Alam, Y. Hamamoto, A. Akisawa, and T. Kashiwagi. Mass recovery adsorption refrigeration cycle—improving cooling capacity. *International Journal of Refrigeration*, 27(3):225 – 234, 2004.

[4] X. Wang, Z. He, and H.T. Chua. Performance simulation of multi-bed silica gel-water adsorption chillers. *International Journal of Refrigeration*, 52:32 – 41, 2015.

[5] B. Zajaczkowski. Optimizing performance of a three-bed adsorption chiller using new cycle time allocation and mass recovery. *Applied Thermal Engineering*, 100:744 – 752, 2016.

[6] K. Thu, B.B. Saha, K.J. Chua, and K.C. Ng. Performance investigation of a waste heat-driven 3-bed 2-evaporator adsorption cycle for cooling and desalination. *International Journal of Heat and Mass Transfer*, 101:1111 – 1122, 2016.

[7] S.M. Ali, P. Haider, D.S. Sidhu, and A. Chakraborty. Thermally driven adsorption cooling and desalination employing multi-bed dual-evaporator system. *Applied Thermal Engineering*, 106:1136 – 1147, 2016.

[8] S. Mitra, P. Kumar, K. Srinivasan, and P. Dutta. Development and performance studies of an air cooled two-stage multi-bed silica-gel adsorption system. *International Journal of Refrigeration*, 67:174 – 189, 2016.

[9] Matthias Schicktanz. *Dynamische Modellierung einer Adsorptionskälteanlage unter besonderer Berücksichtigung des Einflusses von Temperaturfluktuationen*. PhD thesis, Technischen Universität Berlin, 2013.

[10] Fuji Silysia Chemical LTD. (Nagoya, Japan). www.fuji-silysia.co.jp. Accessed: 2020-12-15.

[11] X. Wang, W. Zimmermann, K.C. Ng, A. Chakraboty, and J.U. Keller. Investigation on the isotherm of silica gel+water systems. *Journal of Thermal Analysis and Calorimetry*, 76(2):659 – 669, 2004.

[12] M. Suzuki. *Adsorption Engineering*. Copublished by: Kodansha, Tokyo and Elsevier Science Publishers, Amsterdam, 1990.

[13] T.L. Bergman, A.S. Lavine, F.P. Incropera, and D.P. DeWitt. *Fundamentals of Heat and Mass Transfer*. John Wiley and Sons, 7th edition, 2011.

[14] I.S. Glaznev and Y.I. Aristov. The effect of cycle boundary conditions and adsorbent grain size on the water sorption dynamics in adsorption chillers. *International Journal of Heat and Mass Transfer*, 53(9):1893 – 1898, 2010.

[15] Y.I. Aristov. Challenging offers of material science for adsorption heat transformation: A review. *Applied Thermal Engineering*, 50(2):1610 – 1618, 2013. Combined Special Issues: ECP 2011 and IMPRES 2010.

[16] C. Bongs, A. Morgenstern, and H-M. Henning. Evaluation of sorption materials for the application in an evaporatively cooled sorptive heat exchanger. In *Proceeding of the 5th Heat Powered Cycles Conference*, pages 317–322, 2009.

[17] W. Mittelbach and T. Büttner. Compact adsorption chillers with coated adsorber heat exchangers. In *9th International IEA Heat Pump Conference, Zurich, Switzerland*, 2008.

[18] I. Sarbu and C. Sebarchievici. *Solar heating and cooling systems : fundamentals, experiments and applications*. Academic Press, 2017.

[19] Oussama Souaihi. *Multiphysics simulation in buildings*. PhD thesis, Universitat Politècnica de Catalunya, 2017.

[20] James Eduard Braun. *Methodologies for the Design and Control of Central Cooling Plants*. PhD thesis, University of Wisconsin - Madison, 1988.

[21] M. Abu Madi, R.A. Johns, and M.R. Heikal. Performance characteristics correlation for round tube and plate finned heat exchangers. *International Journal of Refrigeration*, 21(7):507 – 517, 1998.

[22] C. Wang, Y. Hsieh, and Y. Lin. Performance of plate finned tube heat exchangers under dehumidifying conditions. *Journal of Heat Transfer*, 119(1):109–117, 02 1997.

[23] R. Judkoff and J. Neymark. International energy agency building energy simulation test (BESTEST) and diagnostic method. *NREL/TP-472-6231, National Renewable Energy Laboratory, Golden, CO*, 1995.

[24] G. Papakokkinos, J. Castro, R. Capdevila, and R. Damle. A comprehensive simulation tool for adsorption-based solar-cooled buildings – control strategy based on variable cycle duration. *Energy and Buildings*, 231:110591, 2021.

5

Numerical study of an adsorption-based solar-cooled building

Contents of this chapter have been included in :
- G. Papakokkinos, J. Castro, R. Capdevila and R. Damle, A comprehensive simulation tool for adsorption-based solar-cooled buildings – Control strategy based on variable cycle duration, *Energy and Buildings*, 231, 110591, 2021

5.1 Introduction

This chapter presents the numerical study of an adsorption-based solar-cooled building, using the model presented in Chapter 4. Section 5.2 pertains to a literature review focusing on the works that have studied solar-driven ACSs. Section 5.3 details the case study under consideration. Section 5.4 presents the optimization process of the cycle duration of the ACS and the determination of the required ACS capacity for the case study. Section 5.5 presents the proposed control strategy of the system and Section 5.6 is dedicated to the results of the numerical study.

5.2 Literature review

Computational models concerning ACSs are widely used and reported in the peer-reviewed literature [1]. The reported models which elaborate solar-driven ACSs may be classified in two categories. The first category pertains to dynamic simulations of the ACS coupled with the solar system, although without simulating the building. In these studies, the components of the ACS are modeled individually using lumped-capacitance or one-dimensional approach. The second category of the reported

models pertains to studies which do include the simulation of the building, but they do not solve explicitly the individual components of the ACS. The overall performance of the ACS is evaluated instead as a function of the operating temperatures.

With respect to studies aligned with the first category, El-Sharkawy et al. [2] investigated numerically the application of an ACS coupled with compound parabolic concentrator solar collectors in three locations in the Middle East region. They studied the option of including a hot water storage tank between the solar collectors and the adsorption chiller. They concluded that its incorporation provides more stability to the system and higher cooling capacity at the beginning and at the end of the cycle. The maximum cyclic cooling capacity achieved for the climatic conditions of Jeddah and Cairo was reported as 14.8 kW, while for the case of Aswan, 15.8 kW was achieved. Habib et al. [3] used the experimental data of a solar system installed in Durgapur, India, to investigate numerically the feasibility of a dual mode adsorption chiller in this location. Simulations of the dual mode adsorption chiller proposed by Saha et al. [4] were performed, concluding that it can be driven throughout the year using solar energy; 10 months at the single-stage four-bed mode and 2 months at the double-stage mode, when the regeneration temperature is below 60 °C. Alam et al. [5] numerically studied a two-bed conventional adsorption chiller driven by compound parabolic concentrator collectors for the climatic conditions of Tokyo, Japan. The system did not contain thermal storage and the chiller is directly driven by the solar field. Two cases were studied with respect to the cycle duration and the number of collectors; cycle duration 900 s with 18 collectors and cycle duration 1500 s with 15 collectors. The reported COP is approximately 0.45 and 0.55 for the former and the latter case, respectively. The maximum cyclic cooling capacity achieved is 10 kW for both cases. The authors also reported that an optimization of the cycle duration could reduce the required solar collectors area. The same conclusion was reported in [6], where a similar study was performed for the location of Dhaka, Bangladesh. Koronaki et al. [7] analyzed numerically a solar driven adsorption chiller in three different cities in Eastern Mediterranean (Athens, Nicosia and Alexandria), using a lumped-capacitance model. They reported a maximum cooling capacity of 14.7 kW in Nicosia. They then proceeded to study the influence of various types of solar collectors, including hybrid photovoltaic-thermal collectors. Finally, they studied the influence of the cooling temperature, and reported that a reduction of 2 °C can improve the cooling capacity by 8.57 %, as well as the energy and exergy efficiency by 12.78 % and 21.8 %, respectively. Tso et al. [8] presented a numerical investigation of a

solar-driven double-bed adsorption chiller without thermal storage, located in Hong Kong. A novel adsorbent is employed, a mixture of activated carbon, silica gel and calcium chloride. They considered an adsorption chiller of fixed capacity and studied its performance in terms of COP and SCP, with respect to three different solar collector types and various collectors area. Based on their findings, they recommended 30 m^2 of double glazed collectors as the most appropriate solution for the studied case. The average cyclic COP throughout the day is reported as 0.48. Jaiswal et al. [9] studied numerically a solar field of evacuated tube collectors directly feeding an adsorption chiller at Bangalore, India. They performed a parametric study for the solar field area and cycle duration of the chiller. Several cycle durations of the chiller were simulated, though for each case the cycle duration was kept constant throughout the day. They concluded that these two parameters influence significantly the performance of the system. Pan and Wang [10] studied the effect of the hot water temperature to the optimal cycle duration. They constructed a linear relation that describes the optimal cycle duration as a function of the hot water temperature. They reported that the implementation of this strategy results in a significantly better performance of the adsorption chiller, in comparison to constant cycle duration throughout the day.

Regarding studies related to the second category, Alahmer et al. [11] numerically investigated a solar driven adsorption chiller located in Perth (Australia) and Amman (Jordan), using the TRNSYS software. Parametric studies were performed with respect to the collector inclination, driving temperature, tank storage volume and hot water flow rate. During the summer period, the average COP and cooling capacity for Perth were reported as 0.491 and 10.3 kW respectively, while for Amman, these performance indicators were determined as 0.467 and 8.46 kW. Angrisani et al. [12] used TRNSYS software for the simulation of a 200 m^2 office building in Naples, Italy. The study was concerned with both heating and cooling. For the latter, a solar adsorption chiller was employed, and its performance was investigated based on different solar collector types, inclination angle, solar field area, as well as hot and cold storage size. The results were evaluated from thermal, economical and environmental perspective. They reported solar fractions of 0.71 and 0.78 for the flat-plate and the evacuated collectors, respectively. They estimated that the carbon dioxide emissions avoidance is in the range of 23-49%, with respect to two conventional cooling technologies. Palomba et al. [13] developed a similar model in TRNSYS and compared the numerical results with the performance of a solar cooled building in Shanghai, China [14]. The reported discrepancies are lower than

10 %. Then, they substituted the numerical model of the building by a load profile and proceeded to investigate the system behavior in 5 other locations, conducting parametric studies of design parameters, such as the area and the inclination angle of the solar collectors, as well as the thermal storage size. They concluded that it is possible to achieve annual primary energy savings of 0.97 MWh and carbon dioxide emissions avoidance of 22 kg, per installed square meter of solar collectors. Buonomano et al. [15] considered a three-floor building with integrated photovoltaic-thermal collectors, which are capable to produce electricity and provide useful low temperature thermal energy. The latter is utilized in order to provide space heating, space cooling and domestic hot water. They conducted parametric analyses for four Italian cities. They reported primary energy savings in the range of 59-69%, simple payback period of 10.6-11.3 years and avoided carbon dioxide emissions of 76-84%. Using the same commercial software, similar studies were performed for the climate conditions of Egypt [16], Qatar [17] and Lithuania [18].

The approach followed by the first category of models allows to study the operational characteristics of the ACS (such as cycle duration), and adapt them to the solar energy availability in order to achieve an optimal performance under these conditions. However, since the building is not simulated, the interaction between the ACS and the building cannot be studied. The operation of the ACS is subjected to the temperature of the conditioned space. Therefore, this approach cannot be used for the operational control of the system, for example, to deactivate the ACS when the temperature of the building reaches a minimum level with respect to the thermal comfort of the occupants, or to employ antifreezing strategies for the evaporator. Furthermore, this approach assumes constant evaporator inlet temperature, while in reality it depends strongly on the building interior temperature.

The approach used by the second category allows to extract important conclusions for the overall performance of the entire thermal system. However, there are various limitations as a result of the macroscopic, non-dynamic modeling of the ACS. Firstly, it cannot capture the thermal inertia effects resulting from the activation or deactivation of the ACS, as well as from the variations of the operational conditions. Furthermore, the influence of the inherent cyclic operation of an ACS is not captured, and the secondary circuits appear to have smooth outlet temperature profiles, as commented in [13], whereas in reality the temperature fluctuations are considerable. Additionally, it does not allow to intervene in the cycle duration, which can be a useful manner to adapt the ACS performance to the source or the load conditions.

Moreover, these studies are performed with commercial software, and they often do not report thorough information for the mathematical formulation of the model and its experimental validation.

Consequently, the current state-of-the-art for the simulation of solar-driven ACSs pertains on either omitting completely the building or simplifying significantly the ACS performance. To the author's knowledge, the only work to present an integrative analysis is [19], where a solar cooling and heating application is investigated for the climate of Orly, France. The adsorption chiller components are simulated with lumped capacitance models, and they are coupled with the solar system and a relatively simple building model. The latter does not consider the thermal mass of the walls and the solar gains through the windows. The study focused on the observation and phenomenological understanding of the system, without proposing improvement measures. Furthermore, the authors emphasized in their conclusions that more complex building models are necessary.

As it arises from the literature review, the current state-of-the-art has important limitations with respect to the simulation of the entire thermal system. As elaborated above, these limitations hinder considerably the applicability of such models. Hence, it becomes evident that a comprehensive simulation tool would be highly beneficial, since it allows to simulate more realistically the interaction between the solar system, the ACS and the building.

5.3 Case study: A solar-cooled office in Barcelona

5.3.1 System description

The thermal system considered in this study consists of (i) the solar thermal collectors, (ii) a thermal storage water tank with an incorporated auxiliary heater, (iii) an adsorption cooling system (ACS) and (iv) a building, whose occupants' thermal comfort during hot months must be satisfied. The objective of this study is to investigate the potential of satisfying this cooling demand using solar thermal energy, and thus, take advantage of the associated environmental benefits.

Figure 5.1 illustrates the thermal system under consideration, and a brief description of its operation follows. The solar collectors capture part of the incident solar

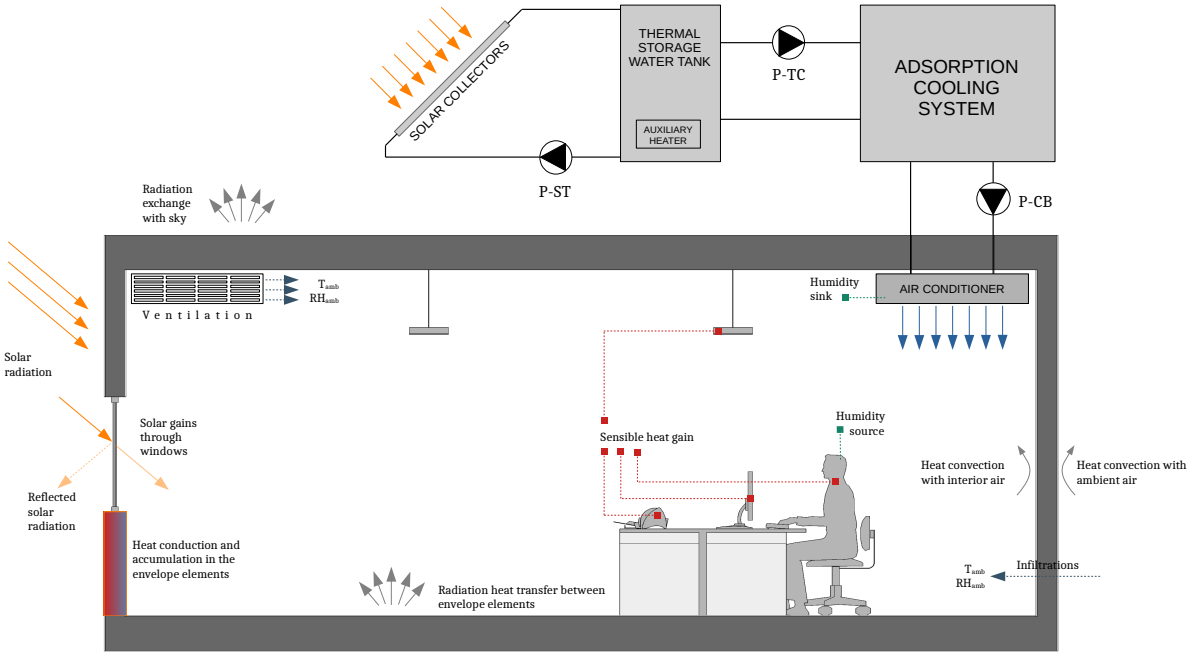

Figure 5.1: Schematic diagram of the thermal system under consideration.

radiation. The tank water is circulated through the solar collectors by pump P-ST, and consequently returns to the tank at a higher temperature. An auxiliary heater is incorporated, in order to heat the tank water when the solar radiation does not suffice. Pump P-TC delivers the accumulated hot water to the thermally-driven ACS. The operation of the latter results in the desired cold production, as temperature drop inside its evaporator. Pump P-CB circulates the heat transfer fluid (HTF) through the evaporator of the ACS, where its temperature is reduced. Subsequently, the chilled HTF is circulated through the air-conditioning unit inside the building. Inside the latter, an air-to-water heat exchanger, the HTF removes thermal energy from the building interior air in order to decrease its temperature and maintain it within thermal comfort levels. The building temperature varies as a result of the internal heat gains (human presence and electrical equipment) and the interaction of the building with its ambient climatic conditions.

5.3.2 Location and type of building

The building under consideration is an office located in Barcelona, Spain (coordinates: 41.38° N, 2.17° E). The climatic data of the location are extracted using the Meteonorm software. The working hours are set between 9am and 6pm.

5.3.3 Envelope and construction elements

A 160 m^2-floor building is considered with dimensions 20 m x 8 m x 3 m. The 20 m facade is oriented towards the south, and it has three double-glazed windows of 7.5 m^2 each. Table 5.1 lists the properties of the materials which constitute the construction elements. The composition of the elements is listed starting from the exterior. Materials that do not contribute significantly to the thermal resistance or thermal mass of the construction elements (such as impermeable membranes) are not simulated, since it would increase the computational cost without affecting the results. The material properties are derived from [20].

Table 5.1: Properties of the construction elements [20].

	Thickness cm	Conductivity W m^{-1} K^{-1}	Thermal capacity J kg^{-1} K^{-1}	Density kg m^{-3}
Roof				
Expanded polystyrene	4	0.035	1675	50
Concrete slab	16	1.13	1000	2000
Lightweight plaster	2	0.16	1000	600
Wall				
Brick	22	0.84	800	1700
Lightweight plaster	2	0.16	1000	600
Floor				
Concrete slab	16	1.13	1000	2000
Tiles	2	0.840	800	1900

5.3.4 Internal gains

This subsection summarizes the heat gains or losses associated to the internal sources and ambient air inflows.

Human heat emission
A total of 16 employees are considered conducting sedentary, moderate work. The relevant heat emissions are reported in [21]. The values adopted in this study pertain to a group, equally comprised by women and men. The total emitted heat is 130W/person. Its distribution to sensible and latent heat depends on the temperature. In [21], the sensible and latent heat are reported for 15, 20, 22, 24 and 26 °C. In this study, a linear interpolation is performed between these reported values, based on the building interior temperature. The sensible heat is considered in the energy conservation equation of the building, while the latent heat is converted to absolute humidity gain, and it is considered in the vapor mass conservation equation.

Electrical appliances heat emission
The workstation of each employee is considered to be equipped with a desktop computer (3.0 GHz processor, 2GB RAM), and a 560mm flat panel monitor, with an average consumption 77 W and 36 W, respectively [22]. Additionally, two laser printers and a scanner are considered, with an average consumption of 130 W and 16 W, respectively [22].

Lighting heat emission
A required illuminance of 500 lux is considered, which is achieved using LED luminaires with a luminous efficacy of 80 lum/W. The associated heat gain of a LED luminaire is considered as 78.1 % of the electric capacity installed, according to [23].

Ventilation and infiltration losses
The ventilation rate, responsible for providing outdoor air during the working hours, is set to 12.5 l/s per person, according to the local legislation [24]. An additional $2.5\,\mathrm{l/(s\,m^2)}$ is applied to the $10\,\mathrm{m^2}$ printing zone in order to remove the contaminants. Furthermore, one air change per hour is assumed throughout the day as the effect of the infiltration through the building envelope. The calculated airflow is considered in

the energy conservation equation, as well as in the vapor mass conservation equation, in conjunction with hourly data of the ambient air temperature and humidity.

5.4 Optimization of ACS cycle duration and determination of ACS capacity

This section summarizes the preliminary calculations performed, in order to determine the cycle durations of the ACS, as well as the capacity of the ACS, which is capable of satisfying the cooling demand and maintaining the building within thermal comfort levels.

5.4.1 Optimization study of the ACS cycle durations

The ACS operation is dictated by two cycle durations, the pre-heating/pre-cooling time t_{pre} and the adsorption/desorption time t_{sor}, whose sum is the half-cycle duration t_{half}. The performance of the ACS – in terms of cooling capacity and COP – depends strongly on the cycle duration. However, an optimum set of (t_{pre}, t_{half}) would be a function of several parameters such as the operating temperatures (temperatures of the secondary circuits HTF) and mass flow rates, geometrical parameters of the components, adsorption pair properties, as well as the desire to prioritize COP over cooling capacity or the inverse. Upon change of any of these parameters, the optimum (t_{pre}, t_{half}) would change as well. Therefore, it is considered essential to present the process of this study, firstly as a parametric study, which is demonstrative of the behavior of the ACS in various (t_{pre}, t_{half}), and secondly, as an optimization study that allows to determine rapidly the desired (t_{pre}, t_{half}).

For the presented case, it is considered $T_{\text{des}} = 80\,^{\circ}\text{C}$, $T_{\text{con}} = T_{\text{ads}} = 30\,^{\circ}\text{C}$ and $T_{\text{eva}} = 15\,^{\circ}\text{C}$ (abbreviated as 80/30/30/15°C). In the parametric study, the cycle duration is varied as follows: (i) the pre-heating/pre-cooling time t_{pre} is varied between 10 s and 100 s with a step of 5 s, and (ii) the half-cycle duration t_{half} is varied between 300 s and 2000 s, with a step of 10 s. Figures 5.2 and 5.3 present in the form of two-dimensional contours the influence of the aforementioned cycle durations on the cooling capacity and the COP, respectively.

As it can be observed, the highest COP and cooling capacity occur in different regions

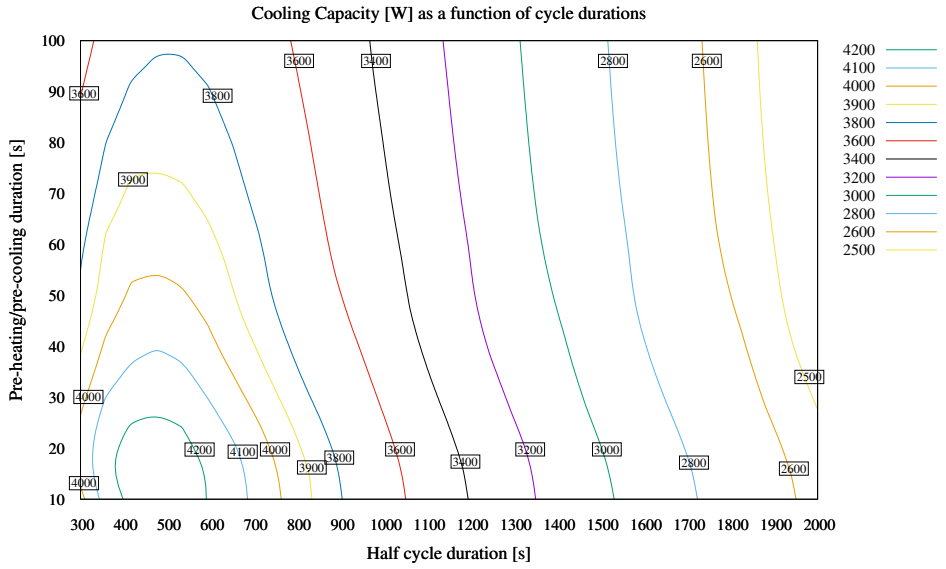

Figure 5.2: Cooling capacity as a function of cycle durations

of the two-dimensional contours. On the one hand, the highest cooling capacity occurs for $t_{\text{pre}} = 15\,\text{s}$ and $t_{\text{half}} = 470\,\text{s}$, where the cooling capacity is 4259.9 W and the COP is 0.366. On the other hand, the highest COP occurs for $t_{\text{pre}} = 50\,\text{s}$ and $t_{\text{half}} = 2000\,\text{s}$, where the COP is 0.567 and the cooling capacity is 2434.5 W. Operating the ACS at the cycle durations that correspond to the maximum COP would result in a significantly lower cooling capacity. In other words, the amount of adsorbent and in general, the size of the ACS would be underexploited. Operating the ACS at the cycle durations which correspond to its maximum cooling capacity would result in a significantly lower COP. Namely, the ACS would consume much more energy. Consequently, a compromise should be achieved through the selection of (t_{pre}, t_{half}) in order to ensure relatively good performance both in terms of COP and cooling capacity.

In order to couple both cooling capacity and COP into one performance indicator of the ACS, the following η-function is constructed:

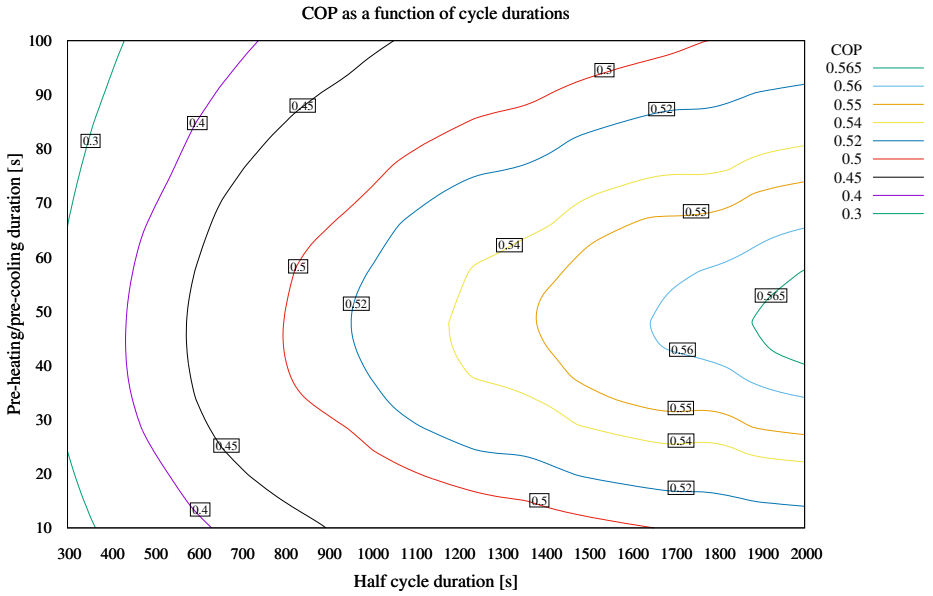

Figure 5.3: COP as a function of cycle durations

$$\eta = \alpha_\eta \left(\frac{\text{COP}}{\text{COP}^*} \right) + (1 - \alpha_\eta) \left(\frac{\dot{Q}_{\text{cool}}}{\dot{Q}^*_{\text{cool}}} \right) \tag{5.1}$$

Where α_η is a weighing factor in order to prioritize the COP or the cooling capacity. It is set to 0.5 when there is no prioritization. Since COP and $\dot{Q}_{\text{cool}}$ have values of different order, it is necessary to normalize them and make them comparable. In order to achieve this, they are divided by COP^* and $\dot{Q}^*_{cool}$, respectively, which correspond to theoretical maximum values.

Figure 5.4 illustrates the result of η-function for the same sets of (t_{pre}, t_{half}), as in Figures 5.2 and 5.3.

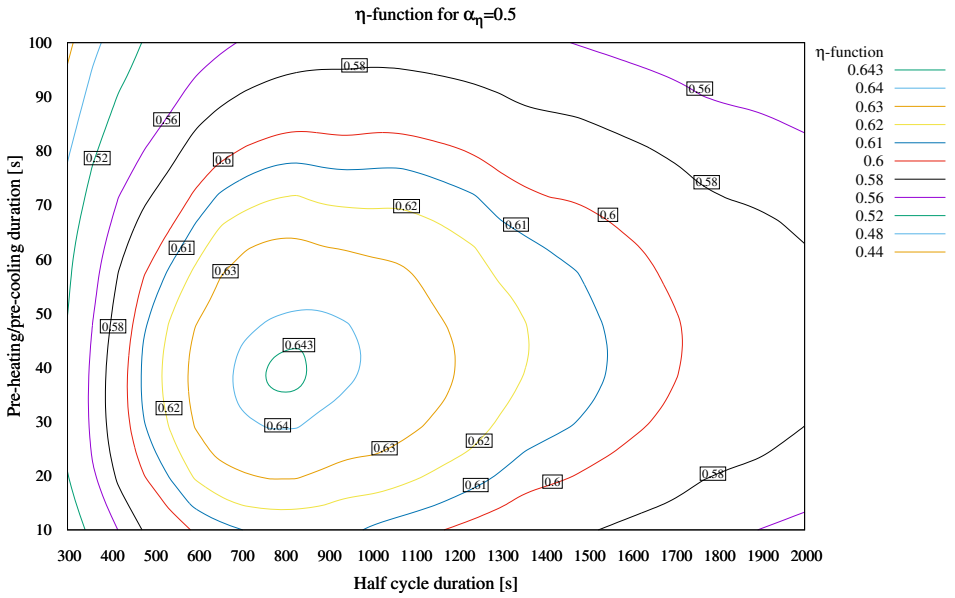

Figure 5.4: η-function for $\alpha_\eta = 0.5$ as a function of cycle durations

The η-function for $\alpha_\eta = 0.5$ is maximized for $t_{\text{pre}} = 40\,\text{s}$ and $t_{\text{half}} = 810\,\text{s}$, where the cooling capacity and COP are 3772.7 W and 0.499, respectively. Within this range of (t_{pre}, t_{half}), 3249 simulations were required to approach the maximum η-function using the parametric study. In order to reduce the required simulations, and thus accelerate the process of determining the desired (t_{pre}, t_{half}), an optimization process is employed. In this case, the NEST platform is coupled to the generic optimization program GenOpt [25]. GenOpt launches the NEST simulations, reads the results and evaluates the optimization function η-function. Then, based on the optimization algorithm (in this case Hooke-Jeeves), GenOpt launches new simulations with the objective to determine the optimum solution of (t_{pre}, t_{half}), within the specified range. Figure 5.5 illustrates the trajectory of the optimization process, from the starting point to the optimum point. Five starting points are considered, one from each of the four corners of the specified range and one from the center. All five cases achieve the optimum point, with the required simulations being between 65 and 93, a significantly lower value than the 3249 simulations of the parametric study. This methodology

is employed extensively in Section 5.6.3, in order to detect the optimum cycles for several operating temperatures and α_η.

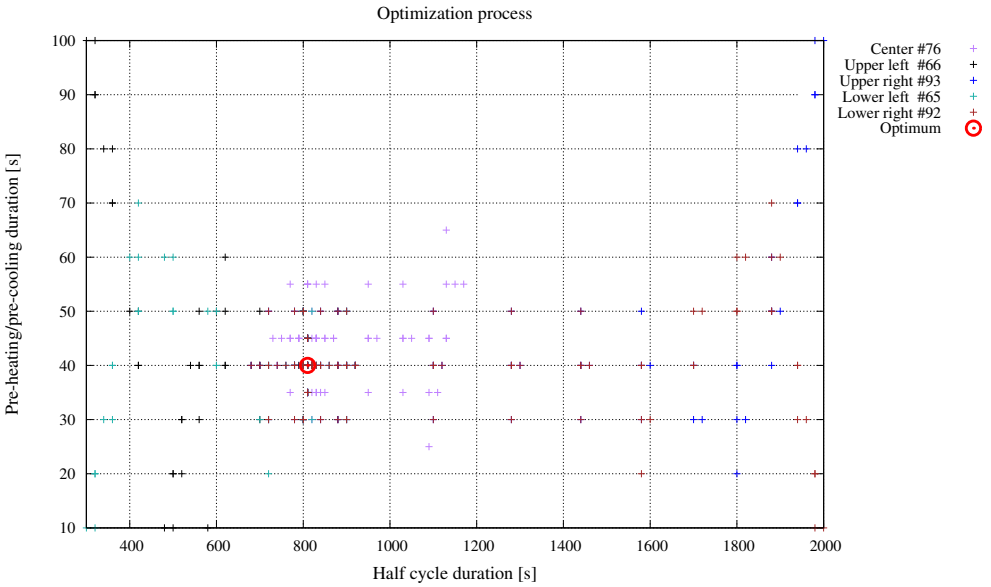

Figure 5.5: Optimization process

5.4.2 Scaling the ACS capacity

The ACS used for the case study is the validated model described in Section 4.4, whose characteristics are presented in Tables 4.1 and 4.2. As mentioned earlier, a priority for the validated model was to allow to extrapolate it to ACSs of other capacities. A scaling factor is applied to the geometrical parameters of the components, the adsorbent mass and the mass flow rates of the secondary circuits. For example, a scaling factor of three would exhibit almost equivalent performance as three ACSs with the capacity of the validated model.

Once the scaled ACSs models were constructed, the same cycle duration optimization process was applied to each of them. Subsequently, simulations coupling the ACS with the building were conducted for the month of July. In these simulations, the solar

collectors and the tank are omitted, instead, the secondary circuit driving temperature is fixed to $T_{des} = 80\,°C$. This approach allows to separate the effect of the solar thermal system, in order to evaluate whether the ACS is capable to satisfy the cooling demand when it operates in its nominal point (cycle durations were optimized for $T_{des} = 80\,°C$).

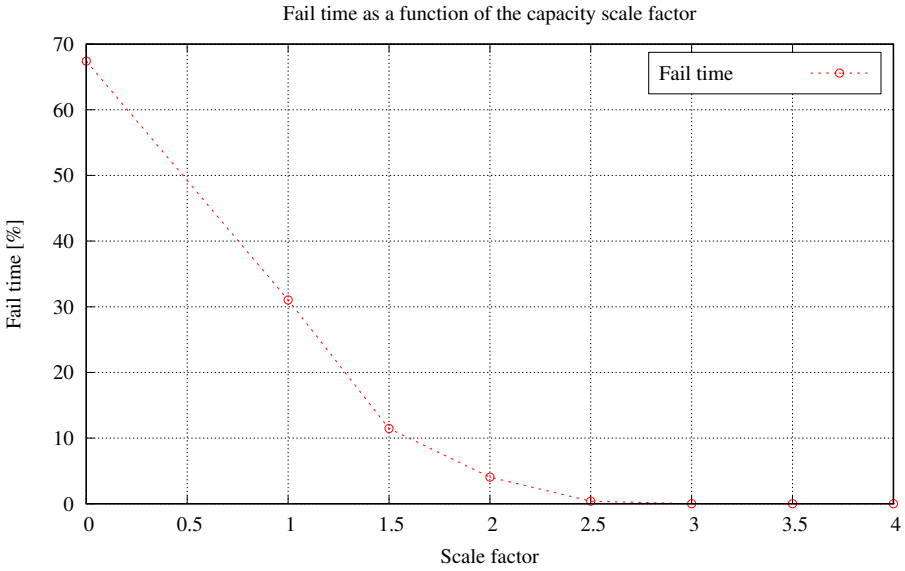

Figure 5.6: Fail time as a function of the capacity scale factor

A performance indicator named fail time is used for the evaluation of ACSs of different capacities. The fail time is the percentage of the time during which the interior temperature is 0.5 °C higher than the designated T_{max}, with respect to the total working hours of the solar-cooled office.

Figure 5.6 shows the fail time for ACSs with scale factors from 1 to 4. At scale factor 0, the fail time corresponds to the case where no cooling is provided to the building. The fail time without cooling is 67.4 %. At scale factor 2.5 the fail time is almost eliminated, and at scale factor 3 the fail time is 0. Consequently, the ACS that can satisfy the cooling demand has a scale factor of 3, and this is the ACS used for further simulations. The performance of this ACS is $\dot{Q}_{cool} = 11\,318.2\,W$ and $COP = 0.499$,

for operating temperatures of 80/30/30/15°C and cycle durations $t_{\text{pre}} = 40\,\text{s}$ and $t_{\text{half}} = 810\,\text{s}$. Figure 5.7 illustrates the interior temperature for scale factors 1, 2, 3 – as well as the case without cooling – on the 22nd of July. As observed, in the case without cooling the interior temperature reaches almost 31 °C. In the cases of scale factors 1 and 2 the interior temperature is above comfort limits, whereas for scale factor 3, it is maintained within comfort limits.

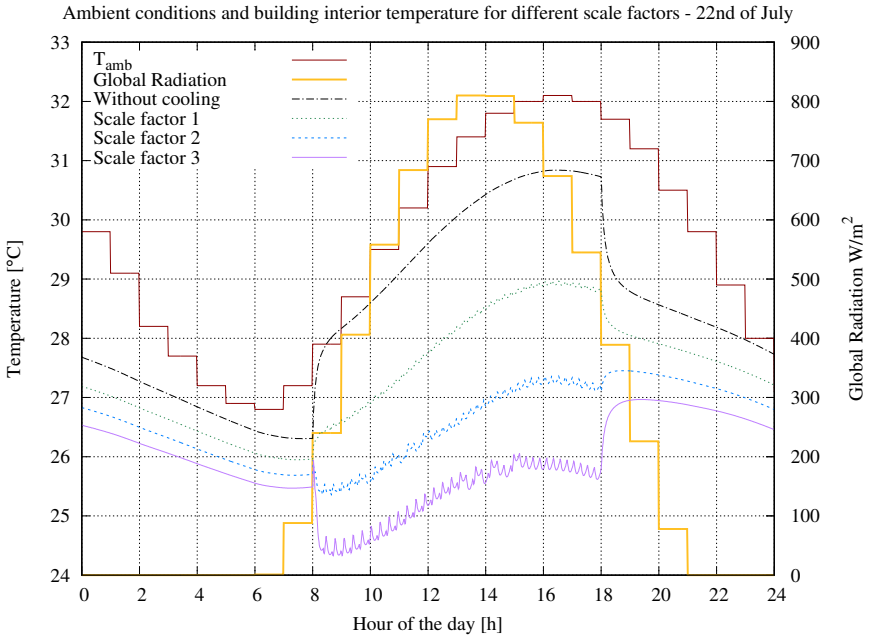

Figure 5.7: Ambient conditions and building interior temperature for different scale factors – 22nd of July

5.5 Control strategy

The thermal system under consideration requires a control strategy in order to achieve its objective and ensure its faultless operation. In this context, there are four elements that require regulation, apart from the inner regulation of the ACS (valve openings that regulate the cycle durations and redirection of secondary circuits). The positions

of these four elements are illustrated in Figure 5.1, while the control strategy is explained below and it is illustrated in Figure 5.8.

- *Pump circulating HTF between the solar collectors and the tank* (P-ST). This pump is controlled by a differential temperature controller, which activates it when the HTF passing through the solar collectors increases its temperature above a certain temperature difference $\Delta T_{\text{solar,on}}$. Below this $\Delta T_{\text{solar,on}}$, pumping the HTF through the solar collectors is considered not beneficial (very low solar radiation) or even counterproductive (during night). In order to avoid oscillations of activation and deactivation of the P-ST, once the P-ST is activated, it will be deactivated when ΔT_{solar} drops below $\Delta T_{\text{solar,off}}$ (where $\Delta T_{\text{solar,off}} < \Delta T_{\text{solar,on}}$). Furthermore, the P-ST will be deactivated if the tank temperature T_{tank} reaches $T_{\text{tank,max}}$, in order to avoid boiling in the tank and delivering temperatures to the ACS higher than the admissible temperature. Once P-ST is deactivated for reaching $T_{\text{tank,max}}$, it will be reactivated at $T_{\text{tank,react}}$.
- *Auxiliary heater of the thermal storage tank* (AUX). The auxiliary heater is activated when the temperature of the tank T_{tank} is lower than a certain temperature $T_{\text{aux,on}}$. The auxiliary heater ensures that when the solar radiation does not suffice, the driving temperature T_{des}, is not lower than the desired level. To avoid oscillations, once the AUX is activated, it is deactivated when the T_{tank} becomes lower than $T_{\text{aux,off}}$ (where $T_{\text{aux,off}} < T_{\text{aux,on}}$).
- *Pump circulating HTF between tank and the chiller desorber* (P-TC). This pump – along with the secondary circuits of the adsorber and condenser, which follow the same pattern – is responsible for the activation of the ACS and consequently, for the desired cooling production. It is considered that the objective of the ACS is to maintain the evaporator temperature within certain limits. Therefore, the P-TC is activated when the T_{eva} becomes higher than a certain $T_{\text{eva,high}}$, and it is deactivated when T_{eva} is lower than $T_{\text{eva,low}}$. The deactivation $T_{\text{eva,low}}$ is necessary in order to avoid freezing in the evaporator, as well as not to deliver undesirably low temperatures to the building. The ACS activation is decoupled from the evaporator secondary circuit. In this way, when the chiller reaches its freezing limit, it is deactivated, although the secondary circuit of the evaporator continues to operate if the temperature in the building interior is high.
- *Pump circulating HTF between the building air-condition unit and the chiller evaporator* (P-CB). This pump is responsible for delivering the low temperature HTF

to the building, and thus, decrease its temperature. P-CB is activated when the interior air temperature T_{int}, exceeds the thermal comfort limit $T_{\text{int,high}}$ and deactivated when it is lower than $T_{\text{int,low}}$, in order not to decrease excessively the T_{int}.

The maximum interior temperature $T_{\text{int,high}}$ is set to 26 °C, which according to [26] is the maximum temperature that would provide thermal comfort of Predicted Mean Vote of PMV $< \pm 0.5$, assuming a metabolic equivalent of task of MET $= 1.2$, and clothing insulation of 0.5 clo. The $T_{\text{int,low}}$ is set to 23 °C. The evaporator temperatures that dictate the operation of the ACS, $T_{\text{eva,low}}$ and $T_{\text{eva,high}}$, are set to 10 °C and 18 °C. The maximum admissible temperature of the tank $T_{\text{tank,max}}$ is set to 90 °C and the $T_{\text{tank,react}}$ is set to 85 °C. The control parameters $T_{\text{aux,off}}$, $T_{\text{aux,on}}$, as well as $\Delta T_{\text{solar,off}}$ and $\Delta T_{\text{solar,on}}$, are investigated in Section 5.6.

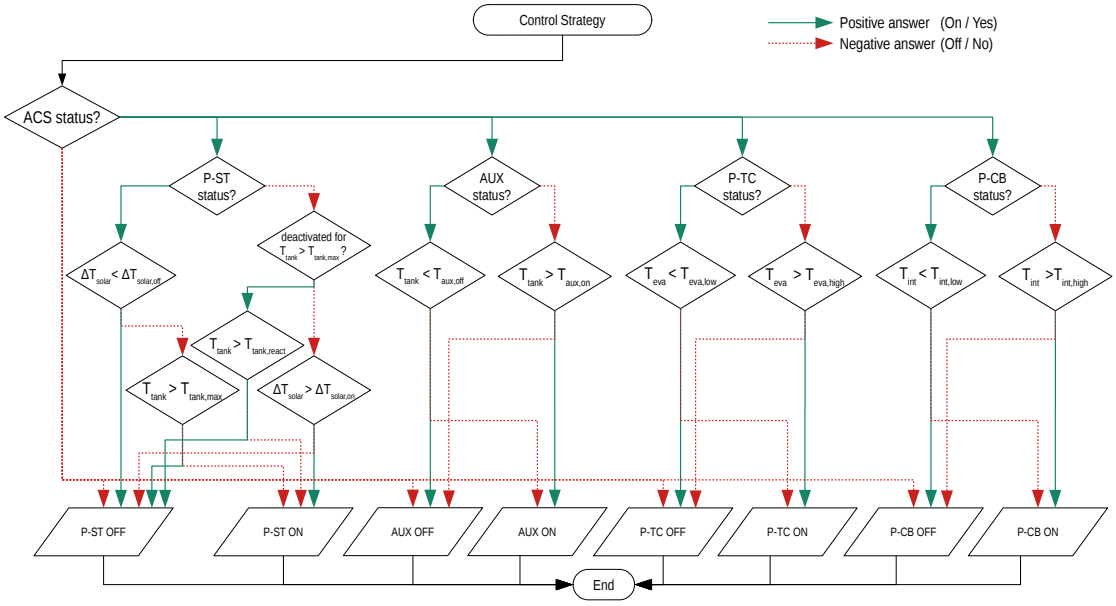

Figure 5.8: Control strategy diagram

5.6 Results and Discussion

This section summarizes the results of the simulations of the entire system. The results pertain to the month of July. The simulations begin earlier in order to eliminate the influence of the initial conditions.

5.6.1 Performance indicators

While many system parameters are monitored, the performance indicator used for the comparison of the results is the solar fraction (SF) of the system, calculated by the equation 5.2. The solar fraction represents the percentage of the thermal energy provided by the solar system Q_{solar}, with respect to the total thermal energy provided, the latter being the sum of the Q_{solar} and the thermal energy provided by the auxiliary heater of the tank Q_{aux}.

$$\text{SF} = \frac{Q_{\text{solar}}}{Q_{\text{solar}} + Q_{\text{aux}}} \times 100\% \tag{5.2}$$

The thermal energy provided by the auxiliary heater Q_{aux} is another performance indicator used in this study. Although this indicator is specific to the system and the period under consideration (month of July), it allows to detect the benefits derived from an improved operation of the ACS, as demonstrated in Section 5.6.3. Furthermore, it is the indicator of the ACS consumption, which is representative of its operating cost, as well as the avoided CO_2 emissions. Therefore, it is of great importance from the user or investor perspective. It also allows the comparison with other cooling systems, as in Section 5.6.4.

It should be mentioned, that many studies used the performance indicator solar Coefficient of Performance $\text{COP}_{\text{solar}}$, calculated as the ratio of the total cooling provided divided by the total solar incident radiation on the collectors. However, in studies considering an auxiliary heater, the $\text{COP}_{\text{solar}}$ does not provide meaningful conclusions, since it does not take into account the contribution of the auxiliary heater. While the numerator of the $\text{COP}_{\text{solar}}$ is nearly constant when the ACS is capable to meet the cooling demand, the denominator – the total incident radiation – is proportional to the collectors area. Consequently, the $\text{COP}_{\text{solar}}$ decreases as a function of the collectors area, ranging from 0.49 for $A_{\text{solar}} = 20\,\text{m}^2$ to 0.12 for $A_{\text{solar}} = 80\,\text{m}^2$.

5.6.2 Results based on constant cycle duration

In this section, results of the simulations are presented for the case of constant cycle durations. The cycle durations used are $t_{pre} = 40\,s$ and $t_{half} = 810\,s$, optimized for operating temperatures of 80/30/30/15°C and $\alpha_\eta = 0.5$. Three phases of simulations are considered, with respect to the control parameters of the auxiliary heater ($T_{aux,on}$, $T_{aux,off}$) and the solar pump ($\Delta T_{solar,on}$, $\Delta T_{solar,off}$). Table 5.2 summarizes the numerical values imposed in each phase for these control parameters. Each phase of the simulations was conducted for solar collectors area A_{solar} between 20-80 m^2 with a step of 10 m^2 and for tank volume V_{tank}, in the range of 200l and 1000l with a step of 100l. However, the results are plotted for a step of 200l for the sake of clarity of the graphs.

Table 5.2: Control parameters for each simulation phase

	P-ST		Auxiliary Heater	
	$\Delta T_{solar,on}$	$\Delta T_{solar,off}$	$T_{aux,on}$	$T_{aux,off}$
Phase A	5 °C	3 °C	80 °C	75 °C
Phase B	5 °C	3 °C	70 °C	65 °C
Phase C	3 °C	1 °C	70 °C	65 °C

Phase A pertains to the case of $T_{aux,on} = 80\,°C$, $T_{aux,off} = 75\,°C$, $\Delta T_{solar,on} = 5\,°C$ and $\Delta T_{solar,off} = 3\,°C$. In this case, the control strategy does not allow the driving temperature to fall more than 5 °C from the nominal point. On the one hand, the ACS is assured that the driving temperature will not become significantly lower than its nominal value. On the other hand, the auxiliary heater is activated more frequently, especially during the morning hours when the tank temperature is low, and solar radiation is not sufficient. Figure 5.9 illustrates the results of the solar fraction and Q_{aux} as functions of the A_{solar}, for various V_{tank}. As arises from the graph, for all tank volumes there is a maximum SF around 50-60m^2. The maximum SF is 55.2 %, and it is observed for $A_{solar} = 50\,m^2$ and $V_{tank} = 800\,l$. The minimum Q_{aux} is 1768 kWh, and it is achieved for the same A_{solar} and $V_{tank} = 600\,l$. At larger solar fields, the maximum temperature of the tank $T_{tank,max}$ is achieved more frequently, and consequently, the pump P-ST is deactivated for larger periods of time. At $A_{solar} = 80\,m^2$, it becomes evident that the case with the lower $V_{tank} = 200\,l$ can accommodate less thermal energy than the case of the highest $V_{tank} = 1000\,l$ and consequently, more solar energy

is rejected, and thus, it has lower SF. It can be also observed that at lower A_{solar}, the SF is approximately 27 % for all V_{tank}, while the Q_{aux} is over 2800 kWh. In these cases, the tank volume does not have a significant effect on the SF, since the solar thermal energy production is relatively low and it can be entirely admitted in the tank.

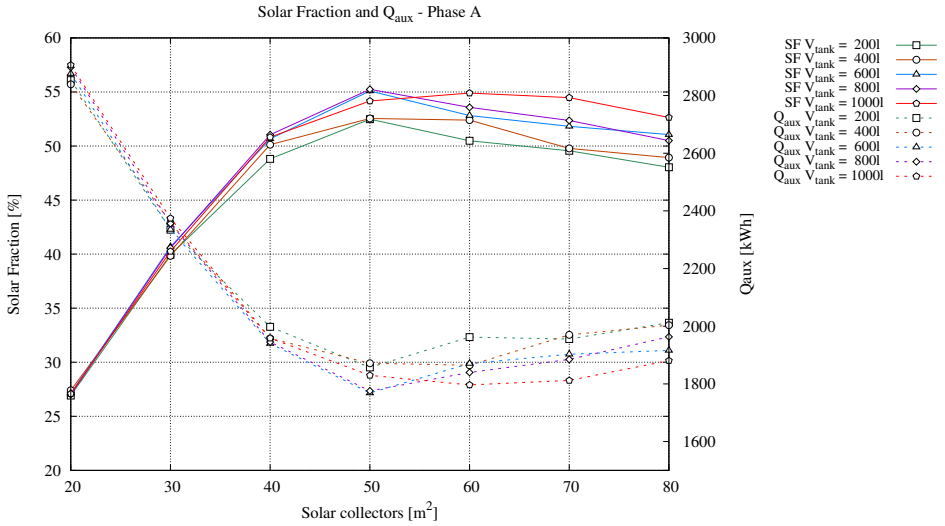

Figure 5.9: Solar fraction and Q_{aux} for Phase A of the simulations

Phase B pertains to the same case as Phase A, with the difference that the driving temperature is allowed to become much lower, having as control parameters $T_{aux,on} = 70\,°C$, $T_{aux,off} = 65\,°C$. In contrast to Phase A, the driving temperature is allowed to decrease more, and thus, the ACS operates with significantly lower driving temperature than its nominal point. However, even though the ACS operation is not efficient, it is based on solar energy, and thus, the SF increases. Figure 5.10 illustrates the results of the solar fraction and Q_{aux} for this phase. In this case, solar fractions over 67 % are observed, a significant increase with respect to the maximum SF of Phase A, 55.2 %. With respect to the Q_{aux}, the lowest value achieved is 1283 kWh, which constitutes a reduction of 27.4 % with respect to the corresponding value of Phase A.

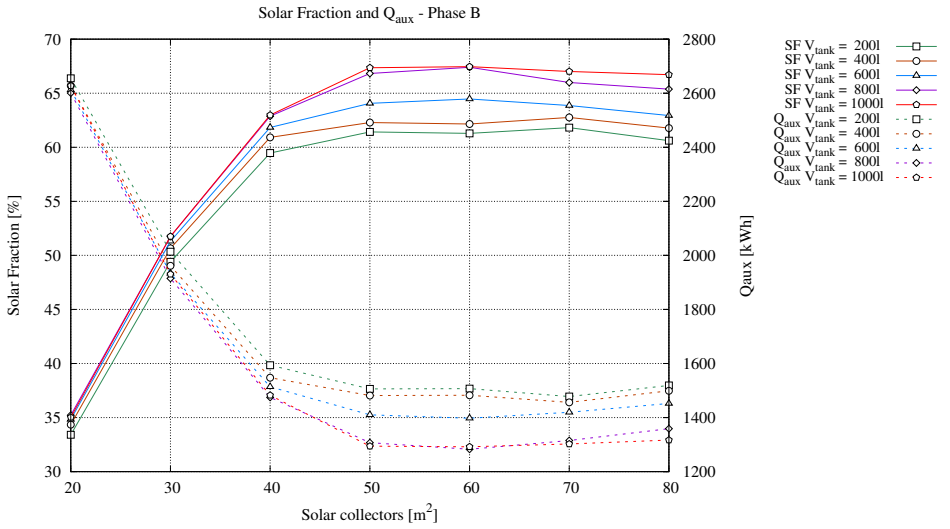

Figure 5.10: Solar fraction and Q_{aux} for Phase B of the simulations

Phase C pertains to the same case as Phase B, although in this case the control parameters related to the operation of the differential temperature controller of the solar field are imposed as $\Delta T_{\text{solar,on}} = 3\,^{\circ}\text{C}$ and $\Delta T_{\text{solar,off}} = 1\,^{\circ}\text{C}$. This results in a higher operation time of the solar field, and consequently, the SF increases. The drawback of this control strategy is that it would require precise temperature sensors in order to detect the $\Delta T_{\text{solar}} = 1\,^{\circ}\text{C}$. Figure 5.10 illustrates the results of the solar fraction and Q_{aux} for Phase C. A significant increase on the SF is observed. The maximum solar fractions are in the range of 84.7-87.7 %, and they are exhibited at $A_{\text{solar}} = 80\,\text{m}^2$ for all V_{tank} except for 1000l, which exhibits its maximum at $A_{\text{solar}} = 70\,\text{m}^2$. However, it should be mentioned that the SF is quite high for $A_{\text{solar}} = 50\,\text{m}^2$, being only 4.4-5.7 % lower than the respective maximum of the V_{tank} under consideration. Therefore, it could be argued that above $A_{\text{solar}} = 50\,\text{m}^2$, a larger solar field – associated to higher installation cost, and the necessity of a larger space – does not contribute significantly to the SF increase. With respect to the Q_{aux}, a significant reduction is achieved, reaching values lower than 500 kWh. With respect to Phase B, the reduction of Q_{aux} is averaged for the various V_{tank}, of each case of solar field A_{solar}. This reduction increases with A_{solar}, ranging from 10.9 % to 62.6 %, which correspond to A_{solar} of $20\,\text{m}^2$ and $80\,\text{m}^2$, respectively.

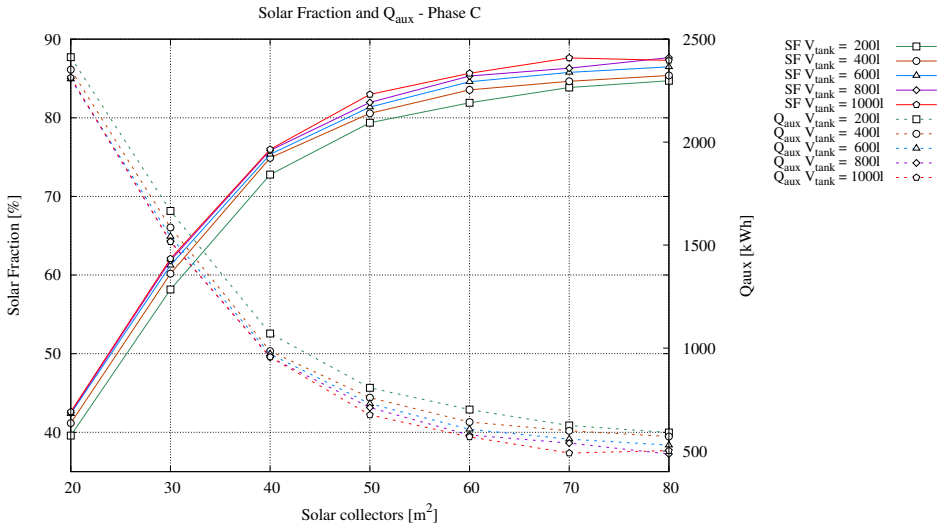

Figure 5.11: Solar fraction and Q_{aux} for Phase C of the simulations

5.6.3 Results based on variable cycle duration

As mentioned earlier, the results presented above pertain to an ACS with constant cycle duration. In this section, it is attempted to improve the efficiency of the ACS by adapting the cycle duration to the instantaneous operating temperatures. Furthermore, the weighing factor α_η is varied in order to explore the ACS performance when COP is prioritized. Therefore, the optimization process presented in Section 5.4.1 is repeated for a total of 495 cases, which are the combinations of the following:

- T_{des} in the range of 70-90°C, with a step of 2 °C
- T_{eva} in the range of 10-18°C, with a step of 1 °C
- α_η (the weighing factor which prioritizes COP over cooling capacity) in the range of 0.5-0.9, with a step of 0.1

When a cycle of the ACS is completed, the control strategy evaluates the operating temperatures and determines the new cycle duration. The latter is the optimum value for the instantaneous operating temperatures, as arose from the optimization

studies. The simulations are based on the same control criteria used in Phase C and they are conducted for $V_{\text{tank}} = 600\,\text{l}$. For each A_{solar}, five simulations with variable cycle duration are performed, using the optimized cycle durations for each of α_η. Figure 5.12 presents the results regarding the solar fraction and the Q_{aux}, as well as the results corresponding to the case of constant cycle of Phase C for $V_{\text{tank}} = 600\,\text{l}$.

Firstly, it should be mentioned that at higher α_η, prioritizing the COP in such extent results to significantly lower cooling capacity, and consequently, to appearance of fail time (as defined in Section 5.4). The fail time for the case of $\alpha_\eta = 0.7$ is exhibited only for A_{solar} in the range of 20-40 m^2, and it is lower than 0.21 %, whereas for α_η of 0.8 and 0.9 the fail time appears in all A_{solar}, and it only exceeds 1 % for $\alpha_\eta = 0.9$ and $A_{\text{solar}} \leq 30\,\text{m}^2$. To put the fail time in context, fail time of 1 % corresponds to 3.1 h without thermal comfort throughout the month of July. Although this fail time can be considered acceptable, new simulations demonstrated that it can be eliminated if another control criterion is applied. The cases exhibiting fail time were repeated by considering that if the interior temperature is higher than 25 °C, the cycle duration should be chosen based on $\alpha_\eta = 0.6$. In this way, when the interior temperature is closer to the thermal comfort limit, the cycle duration prioritizes COP in a lesser degree and thus, the cooling capacity is higher and thermal comfort is satisfied.

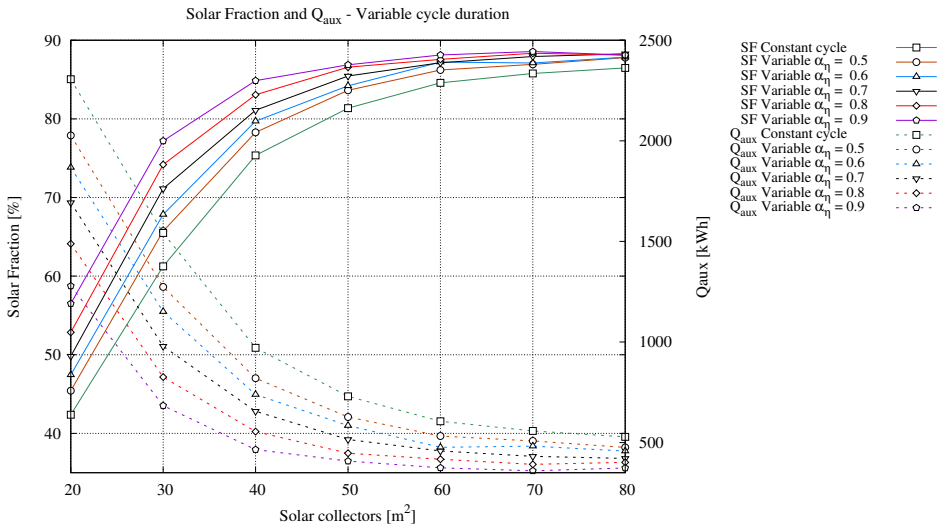

Figure 5.12: Solar fraction and Q_{aux} for variable cycle duration

It should be emphasized that the variable cycle approach is not anticipated to influence significantly the solar fraction. Although an increase in the SF is observed, the variable cycle approach reduces the entire thermal input of the ACS, but its distribution to Q_{solar} and Q_{aux} does not change drastically. In this case, the meaningful indicator is the auxiliary thermal input Q_{aux}, which is related to the economical cost and environmental harm that is associated to the operation of the ACS. There are two ways to interpret the results. The first is to observe that for a given solar field, employing a variable cycle duration approach results in a reduction of the required Q_{aux}. This effect is more significant in the lower A_{solar} of the studied range, and less significant in the larger A_{solar} of the studied range. Comparing the case of constant cycle duration to the case of $\alpha_\eta = 0.9$, the Q_{aux} reduction ranges from 44.5 % for $A_{solar} = 20\,m^2$ to 29.3 % for $A_{solar} = 80\,m^2$. The second way to interpret the results is by observing that if variable cycle duration approach is employed, the same consumption of Q_{aux} can be achieved with a lower A_{solar}, and thus, with lower installation costs and lower space requirements. As an example, it can be observed that the Q_{aux} for $A_{solar} = 40\,m^2$ and $\alpha_\eta = 0.9$ is 12 % lower in comparison to $A_{solar} = 80\,m^2$ and constant cycle duration. With respect to these two specific cases, it is concluded that an optimized variable cycle approach may allow to satisfy the cooling demand using half solar collectors area and lower auxiliary consumption in comparison to constant cycle duration.

5.6.4 Perspective for carbon dioxide emissions avoidance

This section attempts to put in context the CO_2 emissions avoidance that would result from the utilization of a solar-driven adsorption cooling system instead of an electricity-driven conventional cooling system. For the latter, two performances are considered; COP=2 and COP=4, corresponding to relatively low and relatively high performance, respectively. Through the simulations, it arose that in order to meet the cooling demand of the building in July, approximately 2000 kWh of cooling should be provided. Accordingly, the required electrical energy would be 1000 kWh_e and 500 kWh_e, for COP 2 and 4, respectively. The CO_2 emissions related to the consumed electrical energy are subjected to the energy mix of the electrical grid. Two cases are considered, the average and the highest CO_2 emission intensity $g\,CO_2/kWh_e$ of the European Union for 2016. According to the European Environment Agency [27], these values are 295.8 $g\,CO_2/kWh_e$ and 818.9 $g\,CO_2/kWh_e$. The CO_2 emissions for the combinations of the two COP and two carbon intensities are shown in Table 5.3.

Table 5.3: CO_2 emissions of electricity-driven cooling systems (in kg, for the month of July)

	COP = 2	COP = 4
EU_{aver} 295.8 g CO_2/kWh$_e$	295.8	147.9
EU_{max} 818.9 g CO_2/kWh$_e$	818.9	409.5

From the simulations results, the minimum thermal input energy exhibited by the auxiliary heater $Q_{aux_{min}}$ is 359.3 kWh$_{th}$. However, technoeconomic restrictions may not allow to implement a system capable of achieving the aforementioned $Q_{aux_{min}}$. Therefore, apart from $Q_{aux_{min}}$, the $Q_{aux} = 500$ kWh$_{th}$ is taken into consideration as well, representing a more feasible case since it can be achieved by lower A_{solar}. Considering that this thermal input is delivered by a natural gas boiler, these two values are converted to CO_2 emissions by applying a boiler efficiency of 95% (already available in the market), and an emission factor of 202 g CO_2/kWh$_{th}$ for natural gas combustion [28]. Therefore, the associated CO_2 emissions are 106.3 kg CO_2 and 76.4 kg CO_2, for $Q_{aux} = 500$ kWh$_{th}$ and $Q_{aux_{min}}$, respectively. Comparing the case of the ACS with $Q_{aux} = 500$ kWh$_{th}$ to the case of electricity-driven cooling system with COP=4 and the average EU CO_2 emission intensity, a decrease of CO_2 emissions of 28.1% is achieved. Comparing the case of the ACS with $Q_{aux_{min}}$ to the case of electricity-driven cooling system with COP=2 and the maximum EU CO_2 emission intensity, a reduction of CO_2 emissions of 90.7% is achieved. It should be noted that further CO_2 emission reduction can be achieved, if a biomass boiler is employed instead of a natural gas boiler.

5.7 Conclusions

This chapter was dedicated to the numerical study of an adsorption-based solar-cooled building. A case study is defined regarding a solar-cooled office located in Barcelona, Spain. The thermal system under consideration involves the solar collectors, the thermal storage tank with its incorporated auxiliary heater, the ACS and the building. Prior to the investigation of the entire thermal system, two preliminary tasks are carried out.

The first preliminary task involves the coupling of the ACS model to the generic optimization program GenOpt [25]. This coupling provides the ability to perform optimization studies using the model. In this case, the optimization studies focus

on the two characteristic durations of the adsorption thermodynamic cooling cycle – namely, the pre-cooling/pre-heating duration t_{pre} and the half cycle duration t_{half}. In order to illustrate the importance of these parameters, a parametric study is conducted for t_{pre} in the range of 10-100 s and for t_{half} in the range of 300-2000 s. The dichotomy between cooling power and COP related to the cycle durations becomes evident, since their maxima occur at completely different regions. The maximum cooling power occurs for $t_{\text{pre}} = 15$ s and $t_{\text{half}} = 470$ s, where the cooling capacity is 4259.9 W and the COP is 0.366. The maximum COP occurs for $t_{\text{pre}} = 50$ s and $t_{\text{half}} = 2000$ s, where the COP is 0.567 and the cooling capacity is 2434.5 W. A function that evaluates conjointly the cooling capacity and the COP is fabricated and it is optimized. The function allows the prioritization of one of the two performance indicators. In the case without prioritization, the optimum is exhibited for $t_{\text{pre}} = 40$ s and $t_{\text{half}} = 810$ s, where the cooling capacity and COP are 3772.7 W and 0.499, respectively.

The second preliminary task involves the determination of the ACS capacity, which is sufficient for the satisfaction of the cooling demand. The ACS model presented in Chapter 4 is scaled to different capacities. Then, the building is simulated with the ACS of different capacities. The minimum scale factor that allows the satisfaction of the cooling demand of the building is 3.

Subsequently, a control strategy is proposed. In the initial stage, fixed cycle durations are considered, according to the aforementioned optimization study. The control strategy regulates four elements: (i) the pump between the solar collectors and the storage tank, (ii) the pump between the tank and the ACS, (iii) the auxiliary heater of the tank and (iv) the pump between the evaporator and the building. Three simulation phases are conducted using different control criteria for the elements (i) and (iii). Each simulation phase is conducted for solar collectors areas in the range of 20-80 m^2 and thermal storage tank volumes in the range of 200-1000 l. To illustrate the effects of the control criteria in a distilled manner, the solar fraction and the auxiliary energy input are summarized below for the case of $A_{\text{solar}} = 40\,\text{m}^2$ and $V_{\text{tank}} = 600$ l.

Phase A considers as temperature difference for the activation of the solar pump $\Delta T_{\text{solar,on}} = 5\,^{\circ}\text{C}$ and for its deactivation $\Delta T_{\text{solar,off}} = 3\,^{\circ}\text{C}$, as well as activation temperature of the auxiliary heater $T_{\text{aux,on}} = 80\,^{\circ}\text{C}$ and deactivation $T_{\text{aux,off}} = 75\,^{\circ}\text{C}$. The SF achieved is 50.7% and the contribution of the auxiliary heater is $Q_{\text{aux}} = 1940$ kWh. In Phase B, the $T_{\text{aux,on}}$ and $T_{\text{aux,off}}$ are reduced to 70 °C and 65 °C, respectively. For the case under consideration, the SF is 61.8% and the contribution of the auxiliary heater is $Q_{\text{aux}} = 1513$ kWh. Subsequently in Phase C, the $\Delta T_{\text{solar,on}}$ and $\Delta T_{\text{solar,off}}$ are

reduced to 3 °C and 1 °C, respectively. The SF achieved is 75.4% and the contribution of the auxiliary heater is $Q_{\text{aux}} = 971\,\text{kWh}$.

Subsequently, a variable cycle duration approach is adopted. The aforedescribed optimization study is conducted for multiple combinations of operating temperatures and weighing factors α_η for the prioritization of COP. The variable cycle duration employs the optimum cycle duration for the instantaneous operating temperatures. The control criteria are based on Phase C. For weighing factors α_η of 0.5, 0.6, 0.7, 0.8 and 0.9, the contribution of the auxiliary heater that arose from the simulations is 820, 739, 656, 554 and 465 kWh, respectively. The importance of the control strategy is demonstrated, since the contribution of the auxiliary heater – namely, the non-solar energy consumption of the ACS – is reduced by 76%, in comparison to the results of Phase A. Furthermore, another manner to interpret the results is to observe that the adoption of variable cycle duration allows to satisfy the cooling demand with less solar collectors, thus a significant reduction can be achieved in the initial investment and space requirements. For example, the auxiliary heater consumption for variable cycle duration and $A_{\text{solar}} = 40\,\text{m}^2$ is 12% less than the auxiliary heater consumption for Phase C and $A_{\text{solar}} = 80\,\text{m}^2$.

Finally, the CO_2 emissions avoidance that would result from the utilization of the ACS is quantified. The auxiliary heater is assumed to operate with natural gas. The associated emissions are compared to the respective emission of electricity-driven cooling systems. Four scenarios are considered, involving the combinations of two COPs and two carbon intensities. The CO_2 emissions avoidance was calculated between 28.1-90.7%. Further environmental benefits can be obtained if the auxiliary heater operates with biomass instead of natural gas.

References

[1] T. Nagel, S. Beckert, C. Lehmann, R. Gläser, and O. Kolditz. Multi-physical continuum models of thermochemical heat storage and transformation in porous media and powder beds — A review. *Applied Energy*, 178:323 – 345, 2016.

[2] I.I. El-Sharkawy, H. AbdelMeguid, and B.B. Saha. Potential application of solar powered adsorption cooling systems in the Middle East. *Applied Energy*, 126:235 – 245, 2014.

[3] K. Habib, B. Choudhury, P.K. Chatterjee, and B.B. Saha. Study on a solar heat driven dual-mode adsorption chiller. *Energy*, 63:133 – 141, 2013.

[4] B.B. Saha, S. Koyama, K.C. Ng, Y. Hamamoto, A. Akisawa, and T. Kashiwagi. Study on a dual-mode, multi-stage, multi-bed regenerative adsorption chiller. *Renewable Energy*, 31(13):2076 – 2090, 2006.

[5] K.C.A. Alam, B.B. Saha, and A. Akisawa. Adsorption cooling driven by solar collector: A case study for tokyo solar data. *Applied Thermal Engineering*, 50(2):1603 – 1609, 2013. Combined Special Issues: ECP 2011 and IMPRES 2010.

[6] R.A. Rouf, K.C.A. Alam, and M.A.H. Khan. Effect of operating conditions on the performance of adsorption solar cooling run by solar collectors. *Procedia Engineering*, 56:607 – 612, 2013. 5th BSME International Conference on Thermal Engineering.

[7] I.P. Koronaki, E.G. Papoutsis, and V.D. Papaefthimiou. Thermodynamic modeling and exergy analysis of a solar adsorption cooling system with cooling tower in mediterranean conditions. *Applied Thermal Engineering*, 99:1027 – 1038, 2016.

[8] C.Y. Tso, S.C. Fu, and C.Y.H. Chao. Modeling a solar-powered double bed novel composite adsorbent (silica activated carbon/$CaCl_2$)-water adsorption chiller. *Building Simulation*, 7(2):185–196, Apr 2014.

[9] A.K. Jaiswal, S. Mitra, P. Dutta, K. Srinivasan, and S.S. Murthy. Influence of cycle time and collector area on solar driven adsorption chillers. *Solar Energy*, 136:450 – 459, 2016.

[10] Q.W. Pan and R.Z. Wang. Study on operation strategy of a silica gel-water adsorption chiller in solar cooling application. *Solar Energy*, 172:24 – 31, 2018. Special issue for Solar Cooling.

[11] A. Alahmer, X. Wang, R. Al-Rbaihat, K.C. Amanul Alam, and B.B. Saha. Performance evaluation of a solar adsorption chiller under different climatic conditions. *Applied Energy*, 175:293 – 304, 2016.

[12] G. Angrisani, E. Entchev, C. Roselli, M. Sasso, F. Tariello, and W. Yaïci. Dynamic simulation of a solar heating and cooling system for an office building located in southern italy. *Applied Thermal Engineering*, 103:377 – 390, 2016.

[13] V. Palomba, S. Vasta, A. Freni, Q. Pan, R. Wang, and X. Zhai. Increasing the share of renewables through adsorption solar cooling: A validated case study. *Renewable Energy*, 110:126 – 140, 2017.

[14] X.Q. Zhai, R.Z. Wang, Y.J. Dai, J.Y. Wu, Y.X. Xu, and Q. Ma. Solar integrated energy system for a green building. *Energy and Buildings*, 39(8):985 – 993, 2007.

[15] A. Buonomano, F. Calise, A. Palombo, and M. Vicidomini. Adsorption chiller operation by recovering low-temperature heat from building integrated photovoltaic thermal collectors: Modelling and simulation. *Energy Conversion and Management*, 149:1019 – 1036, 2017.

[16] A.M. Reda, A.H.H. Ali, M.G. Morsy, and I.S. Taha. Design optimization of a residential scale solar driven adsorption cooling system in upper Egypt based. *Energy and Buildings*, 130:843 – 856, 2016.

[17] L.F. Sim. Numerical modelling of a solar thermal cooling system under arid weather conditions. *Renewable Energy*, 67:186 – 191, 2014.

[18] K. Januševičius, G. Streckienė, and V. Misevičiūtė. Simulation and analysis of small-scale solar adsorption cooling system for cold climate. *International Journal of Environmental Science and Development*, 6:54 – 60, 2015.

[19] M. Clausse, K.C.A. Alam, and F. Meunier. Residential air conditioning and heating by means of enhanced solar collectors coupled to an adsorption system. *Solar Energy*, 82(10):885 – 892, 2008.

[20] S.V. Szokolay. *Introduction to Architectural Science - The Basis of Sustainable Design*. Architectural Press (Elsevier), 2nd edition, 2008.

[21] Chartered Institution of Building Services Engineers. CIBSE Guide A: Environmental design. www.cibse.org/getattachment/Knowledge/CIBSE-Guide/CIBSE-Guide-A-Environmental-Design-NEW-2015/Guide-A-presentation.pdf, 2015. Accessed: 2020-12-15.

[22] American Society of Heating, Refrigeration and Air-Conditioning Engineers. 2009 ASHRAE Handbook Fundamentals - SI edition, 2009.

[23] B.L. Ahn, J.W. Park, S. Yoo, J. Kim, S.B. Leigh, and C.Y. Jang. Savings in cooling energy with a thermal management system for LED lighting in office buildings. *Energies*, 8:6658–6671, 2015.

[24] Instituto para la Diversificación y Ahorro de la Energía (IDAE), Spanish Ministry of Industry, Energy and Tourism. Guía técnica: Instalaciones de climatización con equipos autónomos, 2012.

[25] Michael Wetter. GenOpt Generic Optimization Program User Manual version 3.1.1. Lawrence Berkeley National Laboratory, simulationresearch.lbl.gov/GO/download/manual-3-1-1.pdf, 2016. Accessed: 2020-12-15.

[26] Fergus Nicol. The limits of thermal comfort: avoiding overheating in European buildings. Chartered Institution of Building Services Engineers (CIBSE), London, United Kingdom, 2013.

[27] European Environment Agency. CO_2 emission intensity. www.eea.europa.eu/data-and-maps/daviz/co2-emission-intensity-6. Accessed: 2020-12-15.

[28] Intergovernmental Panel on Climate Change (IPCC), H. S. Eggleston, L. Buendia, K. Miwa, T. Ngara, and K. Tanabe. 2006 IPCC Guidelines for National Greenhouse Gas Inventories, July 2006.

6

Conclusions and future research

6.1 Conclusions

The objective of this doctoral thesis was to contribute to the investigation of adsorption cooling systems, a sustainable cooling technology. This contribution is attempted through the development of two computational models, which approach ACSs from a different perspective.

Chapter 1 commenced with a brief presentation of the motivation of this thesis. Adsorption cooling is identified as a potential candidate for a sustainable satisfaction of the highly increasing cooling demand. The reader is then gradually introduced to the topic. The discussion initiates with the explanation of the basic phenomena involved – adsorption and cooling production – and subsequently, it elaborates their synthesis into the adsorption cooling concept and the adsorption cooling thermodynamic cycle. Then, the major challenges in the design and operation of ACSs are presented, namely, the dichotomies of the Specific Cooling Power and the Coefficient of Performance induced by the reactor geometry and the cycle duration, as well as the integration of an ACS within a wider thermal system, a solar-cooled building. Chapter 1 concludes with a presentation of the objectives of the thesis – the development of the two computational models and their utilization for the conduction of numerical studies.

Chapter 2 presents the development of the computational model of adsorption packed bed reactors. The reactor is the most important component of an ACS, and in fact, the only distinctive component, since evaporators and condensers form part of other cooling technologies as well. The reactor design is determining for the ACS performance. The developed model is capable to simulate any potential reactor geometry, since it is implemented using three-dimensional unstructured meshes. Both the packed bed and the solid heat exchanger domains are simulated in a conjugate manner, thus allowing to study the influence of the latter on the reactor performance. The modeling approach for intraparticle and interparticle mass transfer is the Linear Driving Force model and the Ergun equation for porous media, respectively. The heat transfer inside the packed bed is modeled with the Local Thermal Non-Equilibrium approach. The computational speed of the model has a decisive impact on its applicability. In order

to improve the computational speed of the model, three modifications were applied on the initial state of the numerical solution algorithm of the packed bed domain. The computational cost was drastically reduced by reducing the required iterations, or by increasing the admissible timestep, or by reducing the computational cost of each iteration. The numerical model was implemented within the in-house C++/MPI CFD platform, TermoFluids. Subsequently, the reliability of the model was questioned through verification and validation assessments. In the verification assessment, the model was evaluated in terms of energy conservation, mass conservation, mesh independence, timestep independence, convergence criteria sufficiency, as well as for correct programming implementation regarding the parallelization in various CPUs, and memory leakage. The verification assessment was categorized in three perspectives, representing different levels of expectations from the model. For the experimental validation, the model performance was compared to experimental results found in the literature. Finally, the necessity of conducting an experiment in CTTC was identified and the experiment was conceptually conceived. The chapter closes with a discussion on the benefits and novelties entailed by this future experiment.

Chapter 3 is dedicated to the numerical studies that were conducted using the computational model presented in Chapter 2. Two major numerical studies were presented. The first study pertains to the investigation and comparison of five different reactor geometries. The motivation of this study is the lack of comparability between different studies across the literature. The five geometries are the (a) tubular reactor with circular radial fins, (b) tubular reactor with square radial fins, (c) tubular reactor with axial fins, (d) rectangular channel with corrugated fins and (e) rectangular channel with hexagonal honeycomb fins. The study involves the quantification of the SCP during the adsorption phase. The quantification of the COP is the next step of this study, since it requires significantly longer simulations. However, in order to allow the comparison among different geometries, the Solid Volume Fraction was introduced. Preliminary COP results prove that – as initially conjectured – geometries with the same SVF have almost equal COP. Therefore although the COP quantification is an ongoing task, during the comparison of the SCP results of different geometries with the same SVF, it can be considered that the COP would be virtually the same. A base scenario was defined with respect to the fin thickness, the fin length and the SVF. Subsequently, a parametric study was conducted with respect to each of these parameters. The second study involves a thorough investigation of a geometry that remained underexplored hitherto – the hexagonal honeycomb adsorption reactor.

A parametric study is conducted with respect to the three dimensions that define the geometry, as well as for various operating conditions. The chapter closes with a discussion of the results from an engineering perspective. Among the discussion of several practical aspects, it is attempted to convey that the reactor design should be application-specific. This arises from the fact that different applications might prioritize to different degree the SCP over the COP, or the inverse, while the design reactor is determinant for these performance indicators.

Chapter 4 is dedicated to the development and validation of the adsorption cooling system model. In this model, a component-level approach is adopted. The reactors are simulated with one-dimensional models, while the evaporator and the condenser are simulated with lumped-capacitance models. The ACS model is validated against experimental results found in the literature, adopting reasonable assumptions where the required information was unavailable. Chapter 4 closes with a brief presentation of the models that are coupled to the ACS model in order to form a comprehensive simulation tool for adsorption-based solar-cooled buildings.

Chapter 5 presents the numerical simulation of a case study, concerning an adsorption-based solar-cooled building. The case study is defined with respect to the building (location, dimensions, orientation, windows, construction elements, infiltrations) as well as with respect to its utilization (time schedules, internal heat and humidity gains, ventilation rate). The validated ACS model presented in Chapter 4 is scaled to various capacities. The building is then simulated with various ACS capacities in order to determine which is the ACS capacity capable to satisfy the cooling demand. Furthermore, the ACS model was coupled to the generic optimization program GenOpt, thus allowing the conduction of optimization studies. In this case, the optimization considered the cycle durations, since they are determinant of the performance of the system. For the operation of the system, a control strategy with fixed cycle duration was proposed and gradually improved. Three simulation phases were conducted with different control parameters. In each of these phases, the simulations were conducted for various combinations of solar collectors and thermal storage volumes. Subsequently, the optimization process was repeated for numerous combinations of operating conditions. The obtained optimum cycle durations were used for the implementation of a control strategy based on variable cycle durations. The latter was proven highly beneficial since it reduces significantly either the auxiliary thermal input or the required solar collectors area. The potential CO_2 emissions avoidance was calculated between 28.1-90.7% with respect to four scenarios of electricity-driven

systems of different performance and CO_2 emission intensity.

6.2 Future research

The outcome of this doctoral thesis lays the foundations for further future research.

With respect to the research direction of the adsorption packed bed reactor:

- Complete the on-going characterization of the COP of different reactor geometries and their comparison.
- The inclusion of other reactor geometries is also under consideration, such as the flat-plate pin fin heat exchanger, in inline and staggered configuration.
- The conduction of the experiment in the CTTC laboratory (elaborated in Section 2.5.2.3). Apart from the laboratory scopes, its adequate documentation and publication will be a meaningful contribution to the community.
- Challenge the experimental validation of the model based on the aforementioned experiment.
- It would be interesting to derive a simplified distributed-parameter model for the reactor. This simplification may result from adopting approaches such as the isobaric assumption for the interparticle mass transfer, the adsorption equilibrium for intraparticle mass transfer or local equilibrium for heat transfer. The idea is to reduce drastically the computational cost – and quantify the error introduced. Then the simplified model – being significantly faster – can be coupled to the generic optimization program GenOpt. The geometric optimization studies would indicate the optimum regions, where the complete model should be employed for a more accurate quantification of the system performance.
- Explore other engineering applications that can be simulated by the model. The most prevalent candidates are the seasonal thermochemical storage and the solar desalination, since they are well-aligned with the research interests of the laboratory.

With respect to the research direction of adsorption cooling systems:

- Focusing on the ACS, more configurations of the thermodynamic cycle can be implemented, studied and optimized.

- The optimization studies presented in the thesis considered the ACS simulation. Subsequently, the obtained optimum results were utilized to shape the control strategy of the ACS when it is coupled to the building, the solar collectors and the thermal storage. In future studies, the optimization procedure will concern the simulation of the entire system. The parameters that can be optimized include: the solar collector area, the thermal storage volume, the inclination angle of the collectors, control criteria values etc.
- The incorporation of a cold storage tank is one of the next steps.
- More complex control strategies should be explored.
- Coupling with more complicated buildings, in terms of geometry and use profile.
- A more holistic investigation for the satisfaction of the cooling demand of the building – by incorporating the use of ACS within a wider control strategy, such as its combination with retractable shadowing elements, nocturnal ventilation and other domotic applications. For example, when the solar thermal input is not sufficient, shadowing elements can be activated in order to decrease the solar gains and consequently the cooling demand. This may allow to the control strategy to prioritize the COP over the SCP and thus, reduce the auxiliary consumption.
- Simulations for a year-round thermal management of the building, in order to evaluate whether the infrastructure for the ACS can be exploited for heating purposes. During the months without cooling demand, the solar collectors can be employed for space heating or domestic hot water supply. The operation of the ACS as a heat pump for heating is also worth investigating.

Nomenclature

Latin symbols

A	area [m^2]
a	exchange surface area per unit volume for spherical particles [m^{-1}]
c_p	specific heat capacity [$J\,kg^{-1}\,K^{-1}$]
d_p	particle diameter [m]
D_e	effective diffusivity [$m^2\,s^{-1}$]
D_0	reference diffusivity [$m^2\,s^{-1}$]
E_a	activation energy [$J\,mol^{-1}$]
f	silica gel active factor [-]
H	enthalpy [J]
h	specific enthalpy [$J\,kg^{-1}$]
K_0	Tóth pre-exponential constant [$kg_w\,kg_s^{-1}\,Pa^{-1}$]
K_D	permeability [m^2]
K_E	inertia-related parameter for Ergun equation [m]
M	mass [kg]
$\dot{m}$	mass flow rate [$kg\,s^{-1}$]
Nu	Nusselt number [-]
$\hat{n}$	surface normal vector
P	pressure [Pa]
Pr	Prandtl number [-]
Q	energy [J]
$\dot{Q}$	heat flux [W]
$\dot{q}$	specific heat flux [$W\,m^{-2}$]
q_m	Tóth monolayer capacity [$kg_w\,kg_s^{-1}$]
R	universal gas constant [$J\,mol^{-1}\,K^{-1}$]
R_g	gas constant [$J\,kg^{-1}\,K^{-1}$]
R_{amb}	thermal resistance of tank for the ambient losses [$m^2\,K\,W^{-1}$]
RH	relative humidity [%]
Re	Reynolds number [-]
T	temperature [K] or [°C]
t	time [s]
U	heat transfer coefficient at the subscripted interface [$W\,m^{-2}\,K^{-1}$]
$\vec{u}$	superficial velocity vector [$m\,s^{-1}$]

V	volume [m^3]
w	adsorbed mass [$kg_w\ kg_s^{-1}$]
w^*	adsorption equilibrium capacity [$kg_w\ kg_s^{-1}$]

Greek symbols

α	metallic plate thickness [m]
α_η	COP weighing factor (equation 5.1)
β	geometry-specific parameter [m or °] (Sec. 3.3)
	cell inradius [m] (Sec. 3.4)
	flag for the operation of the auxiliary heater (Sec. 4.5)
γ	fin length [m] (Sec. 3.3)
	cell height [m] (Sec. 3.4)
δ	fin thickness [m]
ΔH_{ads}	isosteric enthalpy of adsorption [$J\,kg^{-1}$]
ΔH_{evap}	latent heat of evaporation [$J\,kg^{-1}$]
ε	void fraction [-]
ϵ	effectiveness of NTU method, or error
ζ	flag for backflow from reactor to evaporator (Sec. 4.2)
η	efficiency [-]
θ	convergence criterion [-]
λ	thermal conductivity [$W\,m^{-1}\,K^{-1}$]
μ	dynamic viscosity [Pa s]
ξ	flag for backflow from condenser to reactor (Sec. 4.2)
ρ	density [$kg\,m^{-3}$]
σ	standard deviation
τ	Tóth dimensionless constant [-]
ϕ	angle [°] (Sec. 3.3)
	flag for the adsorber operation (Sec. 4.2)
ψ	flag for the evaporator and condenser operation (Sec. 4.2)

Subscripts and superscripts

ad	adsorption
adh	adhesive
ads	adsorber
aff	antifreeze fluid
amb	ambient
aver	average
Al	aluminium
b	bed
calc	calculated
cf	control face
con	condenser
cool	cooling
Cu	copper
cv	control volume
de	desorption
des	desorber
eva	evaporator
expe	expected
g	gas
hx	heat exchanger
if	interface between heat exchanger and packed bed
inc	incident
init	initial
inst	instantaneous
int	interior
iter	iteration
l	liquid
n	node number
p	particle
pc	pre-cooling
ph	pre-heating
pi	particle interface
reac	reactor

react	reactivation
rel	relative
s	solid
sat	saturated
sc	solar collector
sg	silica gel
sec	secondary circuit
sub	sub-timestep
t	total
trans	transient
v	vapor
w	water

Abbreviations

ACS	Adsorption Cooling System
AUX	Auxiliary heater of the thermal storage tank
COP	Coefficient of Performance
GEOM	Geometry
GMRES	Generalized Minimal Residual method
G-S	Gauss-Seidel
HTF	Heat Transfer Fluid
HX	Heat Exchanger
LHS	Left Hand Side
NTU	Number of Transfer Units
P-ST	Pump circulating HTF between the solar collectors and storage tank
P-TC	Pump circulating HTF between the tank and the chiller desorber
P-CB	Pump circulating HTF between the building air-condition unit and the chiller evaporator
PB	Packed bed
RHS	Right hand side
RMSD	Root Mean Square Deviation
SCP	Specific Cooling Power [$W\,kg^{-1}$]
SF	Solar Fraction [%]
SVF	Solid Volume Fraction [%]